

# Development of a Non-Adiabatic Ab Initio Molecular Dynamics Method and its Application to Photodynamical Processes

THÈSE N° 4115 (2008)

PRÉSENTÉE LE 11 JUILLET 2008

À LA FACULTE SCIENCES DE BASE

LABORATOIRE DE CHIMIE ET BIOCHIMIE COMPUTATIONNELLES  
PROGRAMME DOCTORAL EN CHIMIE ET GÉNIE CHIMIQUE

ÉCOLE POLYTECHNIQUE FÉDÉRALE DE LAUSANNE

POUR L'OBTENTION DU GRADE DE DOCTEUR ÈS SCIENCES

PAR

**Enrico Marko TAPAVICZA**

Dipl.-Chemiker Univ., Universität Bayreuth, Allemagne  
et de nationalité allemande

acceptée sur proposition du jury:

Prof. J.-C. Bünzli, président du jury  
Prof. U. Röthlisberger, directrice de thèse  
Prof. M. Casida, rapporteur  
Dr N. Doltsinis, rapporteur  
Prof. J. Vanicek, rapporteur



ÉCOLE POLYTECHNIQUE  
FÉDÉRALE DE LAUSANNE

Suisse  
2008



# Contents

<b>Summary</b>	<b>1</b>
<b>Zusammenfassung</b>	<b>3</b>
<b>1 Introduction</b>	<b>7</b>
<b>2 Basic Principles of Non-Adiabatic Molecular Dynamics</b>	<b>13</b>
2.1 Born-Oppenheimer Expansion and Non-Adiabatic Couplings . . . . .	13
2.2 Born-Oppenheimer Approximation . . . . .	15
2.3 Potential Energy Surfaces . . . . .	16
2.4 Semiclassical Non-Adiabatic Molecular Dynamics . . . . .	16
<b>3 Electronic Structure Methods</b>	<b>21</b>
3.1 The Hartree-Fock Approximation . . . . .	22
3.2 The Time-Dependent Hartree-Fock Method . . . . .	24
3.3 The Configuration Interaction Method . . . . .	25
3.4 Multi-Configurational Self-Consistent Field Method . . . . .	27
3.5 Coupled Cluster Methods . . . . .	28
3.6 Kohn-Sham Density Functional Theory . . . . .	30
3.7 Time-Dependent Density Functional Theory . . . . .	33
3.7.1 The Time-Dependent Kohn-Sham Equations . . . . .	33
3.7.2 Linear Response TDDFT . . . . .	34

<b>4</b>	<b>TDDFT Surface Hopping</b>	<b>39</b>
4.1	Introduction . . . . .	39
4.2	Theory and Implementation . . . . .	41
4.3	Results . . . . .	44
4.4	Conclusion . . . . .	46
<b>5</b>	<b>Non-Adiabatic Coupling Vectors</b>	<b>49</b>
5.1	Introduction . . . . .	50
5.2	Method . . . . .	51
5.3	Computational Details . . . . .	53
5.4	Results . . . . .	54
5.5	Conclusions . . . . .	58
<b>6</b>	<b>Surface Hopping Study of Oxirane Photochemistry</b>	<b>61</b>
6.1	Introduction . . . . .	62
6.2	Theoretical Methods . . . . .	65
6.3	TDDFT/SH Dynamics . . . . .	68
6.3.1	Computational Details . . . . .	69
6.3.2	Results . . . . .	71
6.4	Functionals . . . . .	77
6.4.1	Computational Details . . . . .	78
6.4.2	Vertical Excitation Energies . . . . .	79
6.4.3	Potential Energy Curves . . . . .	81
6.5	Conical Intersections in TDDFT . . . . .	85
6.5.1	Computational Details . . . . .	87
6.5.2	Results . . . . .	88
6.6	Conclusion . . . . .	93
6.7	Noncrossing Rule . . . . .	95
6.8	Supplementary Material . . . . .	99

<b>7</b>	<b>CC2 and TDDFT Studies of a Donor-Bridge-Acceptor Molecule</b>	<b>103</b>
7.1	Introduction . . . . .	104
7.2	Computational Details . . . . .	106
7.3	Results . . . . .	106
7.3.1	Ground State Geometries . . . . .	106
7.3.2	Vertical Absorption Energies . . . . .	108
7.3.3	Geometries of the Excited Charge Transfer State and Fluorescence . . . . .	113
7.3.4	Geometries of the Excited Intradonor State . . . . .	117
7.4	Conclusions . . . . .	118
7.5	Appendix . . . . .	121
<b>8</b>	<b>Conclusions and Outlook</b>	<b>125</b>
	<b>Publications</b>	<b>143</b>
	<b>Presentation and Posters</b>	<b>145</b>
	<b>Acknowledgment</b>	<b>147</b>
	<b>Curriculum Vitae</b>	<b>149</b>



## Summary

Photoprocesses are ubiquitous in nature, science, and engineering. The understanding as well as the optimization of photochemical and photophysical properties of molecular systems requires computational tools that are able to describe the dynamical evolution of the system in electronically excited states.

*Ab Initio* Molecular Dynamics (AIMD) based on Density Functional Theory (DFT) has become an established tool for elucidating mechanisms of chemical reactions that occur in the electronic ground state. However, to describe photoprocesses by AIMD, an underlying electronic-structure method that is able to treat excited states is necessary. This complicates the description of these processes because in the past this implied the use of computationally expensive wavefunction-based methods, which in addition are not straightforward to use.

Time-Dependent Density Functional Theory (TDDFT) provides an in principle exact description of electronically excited states, although in practice, approximations have to be introduced. Compared to wavefunction-based methods, TDDFT is computationally less demanding and is relatively straightforward and easy to use. Recently, TDDFT nuclear gradients have become available and allow to carry out AIMD in excited states.

In this thesis a TDDFT-based AIMD method that is able to account for non-adiabatic effects is developed and implemented. The non-adiabatic couplings are computed by means of a Kohn-Sham orbital based reconstruction of the many-electron wavefunction for ground and excited states. The non-adiabatic scheme is based on the fewest switches trajectory surface hopping (SH) method introduced by Tully.

The method is applied to describe decay processes, such as fragmentation or isomerization, that occur upon photoexcitation of the molecules protonated formalimine and oxirane. In the case of protonated formalimine, the results of the TDDFT-SH method are in good agreement with SH simulations based on the state-averaged complete active space (SA-CASSCF) method, both with respect to the observed reaction mechanisms and the excited state life times. In the case of oxirane, the TDDFT-SH simulations confirm the main experimental results and provide an additional refinement of the postulated reaction mechanism.

The accuracy of TDDFT is investigated with respect to different issues that are especially important for the proper description of photoprocesses. These aspects include the accuracy of non-adiabatic

coupling (NAC) vectors, the description of  $S_1$ - $S_0$  conical intersections, and the description of locally excited states in systems where charge transfer (CT) states are present, that are affected by the well-known CT failure of TDDFT.

Concerning the NAC vectors, a qualitative agreement with SA-CASSCF is found, although magnitudes are underestimated by TDDFT/PBE. Regarding the description of conical intersections to the ground state, we find as expected that TDDFT in the adiabatic approximation (ALDA) is not able to predict an intersection that is strictly conical. However, we find that TDDFT is able to approximate a conical intersection that has a similar shape as the one predicted by SA-CASSCF. For an electron donor-bridge-acceptor molecule it is shown that the CT failure of TDDFT can also considerably affect properties of non-CT states. The use of TDDFT using conventional exchange-correlation functionals is thus not recommended for the description of such systems. Using the second-order approximate coupled cluster (CC2) method in conjunction with a high quality basis set, an accurate and balanced description of both locally excited and CT states can be made. The use of CC2 with large basis sets for AIMD simulations is however still computationally unaffordable for larger systems.

TDDFT is still in its infancy and several attempts to cure some of its deficiencies have already been made. These attempts mainly concern improvements of the approximations of the exchange-correlation functionals and associated TDDFT kernels. The TDDFT-SH method that has been developed in this thesis can in principle be applied in combination with any approximation for the exchange correlation functional, provided that nuclear gradients for this approximation are available and the computational cost remains acceptable. In this way, the method developed here is able to directly profit from the ongoing improvements in the active research field of exchange-correlation functionals and kernels.

**key words:** TDDFT, Tamm-Dancoff approximation, CC2, non-adiabatic molecular dynamics, non-adiabatic couplings, surface hopping, conical intersection, charge transfer failure, oxirane, formalimine, donor-bridge-acceptor, photoisomerization, ring-opening, photoinduced electron transfer.



# Zusammenfassung

Photoprozesse sind allgegenwärtig in Natur, Wissenschaft und Ingenieurwesen. Für das Verständnis sowie die Optimierung von photochemischen und photophysikalischen Eigenschaften molekularer Systeme sind öfters rechengestützte Methoden notwendig, die die dynamische Evolution des Systems beschreiben können.

*Ab Initio* Molekular Dynamik (AIMD), basierend auf Dichtefunktionaltheorie, ist eine etablierte Methode zur Erforschung von Mechanismen von Prozessen, die im elektronischen Grundzustand stattfinden. Zur Beschreibung von Photoprozessen durch AIMD muss jedoch eine Methode verwendet werden die in der Lage ist elektronisch angeregte Zustände zu beschreiben. Dies kompliziert die Beschreibung dieser Prozesse, denn in der Vergangenheit implizierte dies die Verwendung von rechenaufwendigen, auf Wellenfunktionen basierenden Methoden, die nicht einfach anzuwenden sind.

Zeitabhängige Dichtefunktionaltheorie (TDDFT) liefert eine im Prinzip exakte Beschreibung von elektronisch angeregten Zuständen, die in der Praxis jedoch Näherungen erfordert. Im Vergleich zu Methoden basierend auf Wellenfunktionen ist TDDFT weniger rechenaufwendig und relativ einfach zu benutzen. Erst seit kurzem, sind nukleare Gradienten für TDDFT verfügbar und ermöglichen die Anwendung von AIMD in angeregten Zuständen.

In dieser Promotionsarbeit wird eine AIMD Methode entwickelt und implementiert, die auf linear response TDDFT basiert ist und nicht-adiabatische Effekte berücksichtigt. Die nicht-adiabatischen Kopplungen werden anhand einer Vielelektronen Wellenfunktion von Grundzustand und angeregten Zuständen berechnet, die auf der Basis von Kohn-Sham Orbitalen rekonstruiert wurde. Das nicht-adiabatische Schema basiert auf der *Fewest Switches Surface Hopping* (SH) Methode, die von Tully eingeführt wurde. Die Methode ist in der Lage Prozesse wie Fragmentierung und Isomerisierung zu beschreiben, die nach der elektronischen Anregung der Moleküle Oxiran und Formaldiminium Kation erfolgen. Im Falle des

Formaliminium Kations sind die Resultate der TDDFT-SH Methode bezüglich des Reaktionsmechanismus sowie der Lebensdauer des angeregten Zustandes in guter Übereinstimmung mit Simulationen die auf der State-Averaged Complete Active Space (SA-CASSCF) Methode basieren. Im Falle von Oxiran bestätigen die TDDFT-SH Simulationen die Hauptergebnisse der Experimente und geben zusätzlich Informationen zu dem postulierten Reaktionsmechanismus.

Ausserdem wird die Genauigkeit von TDDFT in an betracht verschiedener Aspekte untersucht, die speziell wichtig sind um Reaktionen in angeregten Zuständen zu beschreiben. Zu diesen Aspekten zählt die Genauigkeit von nicht-adiabatischen Kopplungsvektoren, die Beschreibung von konischen Verschneidungen, sowie die Beschreibung von lokal angeregten Zuständen, die beeinflusst sind von der Gegenwart von Elektronentransferanregungen (CT-Anregungen), die von TDDFT fehlerhaft beschrieben werden.

Die Beschreibung der Kopplungsvektoren stimmt qualitativ überein mit Ergebnissen der SA-CASSCF Methode, wobei jedoch die Beträge der Vektoren von TDDFT/PBE unterschätzt werden. Wie erwartet, ist adiabatische TDDFT nicht in der Lage exakt konische Verschneidungen zum Grundzustand vorherzusagen. Jedoch können Verschneidungen näherungsweise konisch beschrieben werden, die der Form von Verschneidungen beschrieben mit SA-CASSCF ähneln. Anhand eines Elektronendonator-Brücke-Akzeptormolekül wird gezeigt, dass der CT Fehler von TDDFT die Beschreibung von lokal angeregten Zuständen entscheidend verfälschen kann. Es ist somit nicht empfohlen, TDDFT mit den konventionellen Austausch-Korrelations-Funktionalen (xc-Funktionalen) zur Beschreibung solcher Systeme zu benutzen. Die Second-Order Approximate Coupled Cluster (CC2) Methode in Verbindung mit Basissätzen von guter Qualität ist jedoche in der Lage, lokale sowie CT Anregungen gleich gut und mit hoher Genauigkeit zu beschreiben. Die Anwendung dieser Methode in AIMD Simulationen ist auf diesem Niveau jedoch noch zu rechenaufwendig für grössere Systeme.

Jedoch ist TDDFT eine relative junge Methode und einige Versuche zur Behebung dieser Fehler wurden schon gemacht. Diese Versuche betreffen zumeist die Verbesserung der Näherungen im xc-Funktional und dem damit verbundenen TDDFT Kern. Die TDDFT-SH Methode, die in dieser Promotionsarbeit entwickelt wurde, kann im Prinzip mit jeder beliebigen Näherung für das xc-Funktional angewendet werden, vorausgesetzt dass nukleare Gradienten verfügbar sind und der Rechenaufwand angemessen bleibt. Auf diese Weise ist die hier entwickelte Methode in der Lage von den laufenden

Verbesserungen im Feld der xc-Funktionale direkt zu profitieren.

**Schlüsselwörter:** Zeitabhängige Dichtefunktionaltheorie, Tamm-Dancoff Näherung, CC2, nicht-adiabatische Molekulardynamik, Surface Hopping, konische Verschneidung, Ladungstransfer-Fehler, Oxiran, Formaldimin, Donor-Bridge-Acceptor, Photoisomerisierung, Ring-Öffnung, photoinduzierter Elektronentransfer.



# Chapter 1

## Introduction

Photoprocesses are physical and chemical processes that involve absorption or emission of visible or ultraviolet light [1]. They may be further classified as either photochemical or photophysical depending on the kind of process (Fig. 1.1), but such a distinction might not always be clearly defined. In photochemical reactions a molecule A is transformed into a chemically different molecule B, so photochemical reactions usually involve the making and/or breaking of chemical bonds. Typical examples are photoinduced fragmentation or polymerisation reactions. In contrast, photophysical processes do not transform a molecule into a chemically different species. They might transform a molecule into another state of the same species, or simply involve absorption or emission of light, decay, and energy transfer phenomena. Fluorescence and phosphorescence are examples of photophysical processes. Some processes might be included in one or the other group, depending on whether one might define the reaction product as a new chemical species or not. Intramolecular photoinduced electron transfer reactions or photoisomerization reactions are examples of processes that might be assigned to either branch.

Photoprocesses are abundant in nature and have a large impact on the organization of life on earth. Photosynthesis in plants [3] is probably the most well known example of a photoreaction. In photosynthesis sun light is converted into chemical energy that is used to synthesize biomolecules. This occurs in a very specific manner requiring a precise fine tuning of the photochemical properties of biochromophores. Other examples of photoprocesses in living organisms are the process of vision, and chemiluminescence and phosphorescence phenomena in insects and fishes. However, the exposure to light can also damage biomolecules, which can have fatal consequences for a living organism [4–6]. This

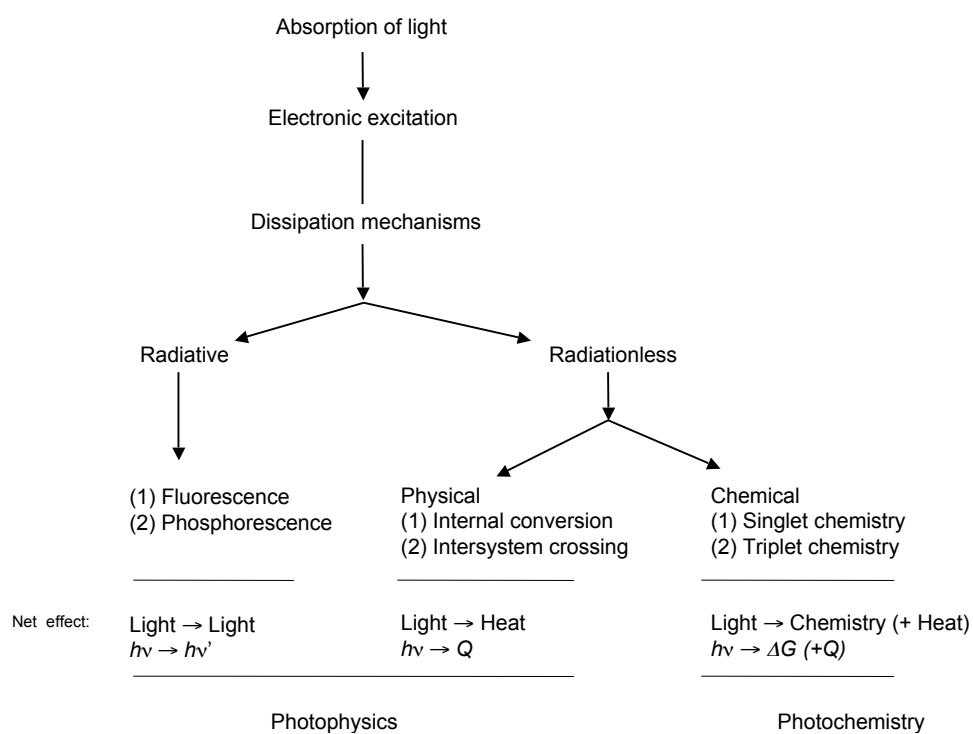


Figure 1.1: Possible decay pathways for a photoinduced process, according to Ref. [2].

---

is not surprising considering that most degradation and transformation reactions of the atmosphere are initiated by the absorption of light [7].

Industrial applications of photochemistry include chemical synthesis, and increasingly also modern technologies such as photovoltaic, optical switches, and light driven molecular motors [8,9] have their basis in photophysical principles.

The scientific understanding of photoprocesses in nature as well as the optimization of photochemical properties of molecules in nano science requires accurate computational tools and physical models to describe these processes.

The central requirement for such theoretical tools is their ability to describe ground and excited state potential energy surfaces with high accuracy. Furthermore, the accurate description of the dynamical behavior of the system is of special interest in photochemistry. While ground state reactions can often be described properly by a minimum energy pathway that is constructed by examination of minima and transition states along the reaction coordinate, this is not the case for photoreactions, which are characterized by a high excess energy and often occur far from equilibrium conditions [10]. Finally, much importance lies in the ability to describe radiationless non-adiabatic transitions, which are electronic transitions that are coupled to the movement of the nuclei. Research in theoretical chemistry over the last number of decades, has shown that these kind of transitions are “the rule rather than the exception” in photoprocesses [11] and often determine reaction rates.

Molecular dynamics is a tool to model physical and chemical processes on an atomic level in real time. *Ab Initio* Molecular Dynamics (AIMD) [12] usually refers to a mixed quantum and classical form of MD. In this model, the nuclear motion is described classically as the motion of point charges with a given mass, whereas the potential energy surface is obtained by a quantum mechanical electronic structure method. The advantage of this approach is that no predefined force-field is required, because the nuclear forces are computed “on the fly” as derivatives of the total potential energy.

AIMD in the electronic ground state is well established [12, 13] and usually relies on Density Functional Theory (DFT) as quantum mechanical method to describe the electrons. DFT is computationally less expensive than most wavefunction based methods, but can only be applied for the electronic ground state. For this reason, non-adiabatic excited state simulations usually imply wavefunction based electronic structure methods ([14] and references therein), such as Multi-Configurational Self-Consistent

Field (MCSCF) methods. Such methods can usually be applied by specialists only because the choice of the kind and number of configurations that must be included is not trivial. An inappropriate choice of the active configurations can bias the evolution of the system. Moreover, the computational expense grows fast with the size of the system and can get intractable for larger molecules.

As alternative to these approaches, special extensions of ground state DFT such as the multiplet-sum method [15, 16] or the Restricted Open-Shell Kohn-Sham (ROKS) approach provide approximate descriptions of excited states, that are however limited either to special symmetries or to a small number of excited states. For instance the ROKS method [17] provides a description of the first excited state and has been applied within a non-adiabatic dynamics scheme [18].

However, during the last 10 years, Time-Dependent Density Functional Theory (TDDFT) [19] has become a popular method for static calculations of electronically excited states [20]. The main advantage of this theory is that it provides in principle an exact description of electronically excited states for a reasonable computational cost. In contrast to MCSCF methods, the application of TDDFT does not require any information about the chemistry of the system. Recently, TDDFT nuclear gradients have been implemented in several public domain and commercial computer codes and thus applications to excited state MD have become feasible.

The aim of this thesis is to explore the possibility to use TDDFT for the modeling of non-adiabatic photodynamical processes. The first objective is the development of a non-adiabatic AIMD method based on TDDFT [21]. The second topic, is the application of the developed method to different chemical systems and to assess the accuracy of TDDFT. Although being in principle an exact theory, in practice the use of TDDFT requires unavoidable approximations. These approximations can eventually lead to a decrease in accuracy and sometimes to a qualitatively incorrect description. To gauge the accuracy of the obtained results they are compared to predictions of other theoretical approaches and experimental data.

In Chapter 2, theoretical principles of molecular dynamics are summarized. Subsequently, different ground and excited state electronic structure methods are reviewed (Chapter 3). In Chapter 4, a non-adiabatic MD approach based on the surface hopping method and TDDFT is developed and applied to a model system. The next Chapter investigates the accuracy of non-adiabatic coupling vectors that were used in the surface hopping approach. In Chapter 6 the TDDFT-SH method is applied to the excited state



reactions of oxirane and compared to experimental data, with a special focus on the description of conical intersections by TDDFT. The last application (Chapter 7) investigates the photophysical properties of an electron donor-acceptor molecule. This study employs TDDFT and Second-Order Approximate Coupled Cluster (CC2) calculations, and compares the performance of the two methods. The last chapter (Chapter 8) provides a summary and outlook.



## Chapter 2

# Basic Principles of Non-Adiabatic Molecular Dynamics

This chapter reviews some of the basic concepts that have been found to be useful for the understanding and modeling of photoprocesses. For more detailed information the reader is referred to textbooks, review articles, and the original articles that cover these aspects in more detail. For example derivations of the Born-Oppenheimer (BO) approximation [22], the BO expansion [23], and the theory of non-adiabatic couplings can be found in the first article [24] of the textbook on conical intersections [11] and elsewhere [25,26]. Aspects on the topological properties of potential energy surfaces may be found in textbooks on photochemistry and photophysics [1,2,25]. Born-Oppenheimer and non-adiabatic molecular dynamics methods are the subject of several review articles [12,27–29].

### 2.1 Born-Oppenheimer Expansion and Non-Adiabatic Couplings

The electronic Hamiltonian is usually defined as

$$\hat{H}_e = \hat{V}_{NN} + \hat{T}_e + \hat{V}_{Ne} + \hat{V}_{ee}, \quad (2.1)$$

where  $\hat{V}_{NN}$  denotes the nuclear-nuclear repulsion,  $\hat{T}_e$  is the kinetic energy of the electrons,  $\hat{V}_{Ne}$  denotes the attraction between nuclei and electrons, and  $\hat{V}_{ee}$  is the electron-electron repulsion. The solutions of

the time-independent *electronic* Schrödinger equation

$$\hat{H}_e(\mathbf{R}, \mathbf{r})\Phi_i(\mathbf{R}, \mathbf{r}) = V_i(\mathbf{R})\Phi_i(\mathbf{R}, \mathbf{r}), \quad (2.2)$$

define the adiabatic electronic states  $\Phi_i(\mathbf{R}, \mathbf{r})$  and their eigenvalues  $V_i(\mathbf{R})$ . Here,  $\mathbf{R}$  and  $\mathbf{r}$  refer to the entire set of the nuclear and electronic coordinates, respectively.

By adding the nuclear kinetic energy operator  $\hat{T}_N$  to  $\hat{H}_e$ , we may define the total Hamiltonian of a molecular system

$$\hat{H} = \hat{T}_N + \hat{V}_{NN} + \hat{T}_e + \hat{V}_{Ne} + \hat{V}_{ee}. \quad (2.3)$$

The eigenfunctions  $\Phi_k$  of the electronic Schrödinger equation form a complete orthonormal basis and thus the time-independent total wavefunction of the total molecular system  $\Psi(\mathbf{R}, \mathbf{r})$  can be described as linear combination of the adiabatic states

$$\Psi(\mathbf{R}, \mathbf{r}) = \sum_i \Phi_i(\mathbf{R}, \mathbf{r})\chi_i(\mathbf{R}). \quad (2.4)$$

This equation is called the BO expansion and constitutes an exact expression in the limit of including an infinite number of all adiabatic states. Inserting (2.4) into the Schrödinger equation of the total system

$$\hat{H}(\mathbf{R}, \mathbf{r})\Psi(\mathbf{R}, \mathbf{r}) = E\Psi(\mathbf{R}, \mathbf{r}), \quad (2.5)$$

multiplying by  $\Phi_j^*$  from the left and integrating over the electronic coordinates we arrive at an expression that can be used to determine the coefficients  $\chi_i$  in the BO expansion [24]

$$[\hat{T}_N + V_i(\mathbf{R})]\chi_i(\mathbf{R}) - \sum_j \hat{\Lambda}_{ji}\chi_j(\mathbf{R}) = E\chi_j(\mathbf{R}). \quad (2.6)$$

The dynamical interaction between the nuclear and electronic motion is described by the non-adiabatic coupling term

$$\hat{\Lambda}_{ji} = \delta_{ji}\hat{T}_N - \langle \Phi_j(\mathbf{R}) | \hat{T}_N | \Phi_i(\mathbf{R}) \rangle. \quad (2.7)$$

Using the usual expression for the nuclear kinetic operator  $\hat{T}_N = -\frac{1}{2M}\nabla_{\mathbf{R}}^2$ , with the average nuclear

mass  $M$  [24], the non-adiabatic coupling operator can be rewritten as

$$\hat{\Lambda}_{ji} = \frac{1}{2M} [2\mathbf{d}_{ji} \cdot \nabla_{\mathbf{R}} + G_{ji}], \quad (2.8)$$

with the derivative non-adiabatic coupling vector  $\mathbf{d}_{ji}$  defined as

$$\mathbf{d}_{ji}(\mathbf{R}) = \langle \Phi_j(\mathbf{R}) | \nabla_{\mathbf{R}} \Phi_i(\mathbf{R}) \rangle \quad (2.9)$$

and the scalar non-adiabatic coupling term  $G_{ji}$  defined as

$$G_{ji}(\mathbf{R}) = \langle \Phi_j(\mathbf{R}) | \nabla_{\mathbf{R}}^2 \Phi_i(\mathbf{R}) \rangle \quad (2.10)$$

## 2.2 Born-Oppenheimer Approximation

Let us assume that due to the slow motion of heavy nuclei, the much lighter electrons immediately adjust when nuclear positions are changed. In this case the total wavefunction is separable and can be written as a product of the nuclear and the electronic wavefunction, leading to a simplified version of (2.4):

$$\Psi(\mathbf{R}, \mathbf{r}) = \Phi_i(\mathbf{R}, \mathbf{r}) \chi_i(\mathbf{R}). \quad (2.11)$$

Using this expression, the equation for the nuclear motion corresponding to (2.6) reads

$$[\hat{T}_N + \hat{\Lambda} + \hat{V}(\mathbf{R})] \chi(\mathbf{R}) = E \chi(\mathbf{R}), \quad (2.12)$$

where indices  $i$  have been dropped because only one adiabatic state is under consideration. The BO adiabatic approximation is obtained by further simplification where  $\hat{\Lambda}$  is set to zero, i.e.,

$$[\hat{T}_N + \hat{V}(\mathbf{R})] \chi(\mathbf{R}) = E \chi(\mathbf{R}). \quad (2.13)$$

Since  $\hat{\Lambda}$  scales inversely with the average nuclear mass  $M$  (2.8) the BO adiabatic approximation can be expected to be valid for systems with large nuclear masses. To illustrate more precisely the limits in which the adiabatic approximation is valid, we consider an alternative expression for the derivative

couplings. Applying the gradient to the electronic Schrödinger equation (2.2), multiplying from the left with  $\Phi_k^*$  and integrating over the electronic coordinates we obtain [27]

$$\mathbf{d}_{kj} = \frac{\langle \Phi_k | \nabla_{\mathbf{R}} \hat{H}_e(\mathbf{R}) | \Phi_j \rangle}{E_j(\mathbf{R}) - E_k(\mathbf{R})}. \quad (2.14)$$

From this expression it is evident that the derivative coupling vanishes for large energy gaps therefore making the adiabatic approximation valid when adiabatic states are well separated from one another. For small energy gaps on the other hand, one cannot expect the adiabatic approximation to be valid.

### 2.3 Potential Energy Surfaces

For each set of fixed nuclear coordinates  $\mathbf{R}$  of a system there is an infinite number of solutions for the electronic Schrödinger equation (2.2). Solving this equation for a given number of adiabatic states at all possible nuclear positions  $\mathbf{R}$  defines the manifold of adiabatic potential energy surfaces (PESs) of a system. The dimensionality of this hypersurface depends on the number of internal nuclear degrees of freedom (DOF) of the system, which amounts to  $3N - 6$  in case of a polyatomic nonlinear molecule containing  $N$  atoms. As schematically shown in Fig. 2.1, the minima (b) and transition states (c) on the PESs indicate possible reaction pathways. Special importance is attributed to points or regions on this hypersurface that connect two or more surfaces and mediate radiationless transitions (d, e). These regions, denoted as *funnels*, can further be distinguished into two types. If a funnel has two or more surfaces touching one another (e) they are called *conical intersections* whereas in regions where two surfaces come close to one another without touching (d) they are usually referred to as *avoided crossings*. Funnels provide decay pathways to the ground state PES and proceed orders of magnitude faster than decay processes involving emission (fluorescence (f) and phosphorescence (g)).

### 2.4 Semiclassical Non-Adiabatic Molecular Dynamics

To describe the evolution of a chemical system in time, one has to solve the time-dependent Schrödinger equation at a fully quantum mechanical level

$$\hat{H}\Psi(\mathbf{R}, \mathbf{r}, t) = i \frac{\partial}{\partial t} \Psi(\mathbf{R}, \mathbf{r}, t). \quad (2.15)$$

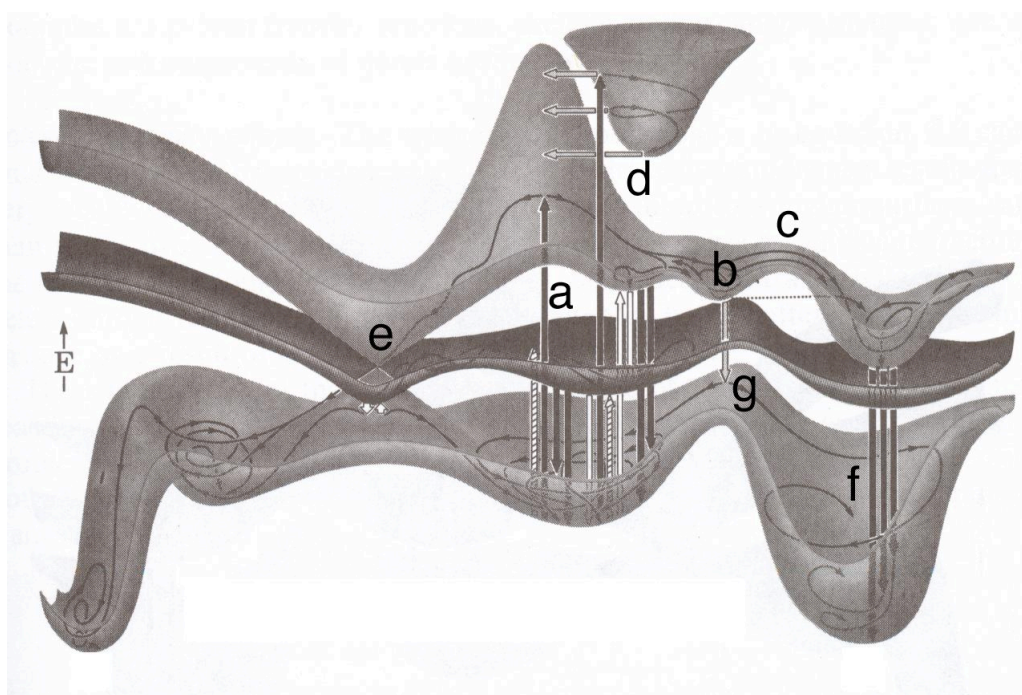


Figure 2.1: Schematic representation of ground and excited state potential energy surfaces. The grey surfaces stand for singlet states and the dark surface indicates a triplet state. a) singlet excitations, b) energetic minimum, c) saddle point, d) avoided crossing, e) conical intersection, f) fluorescence, and g) phosphorescence. The labels were added to the picture taken from Ref. [1] with permission of V. Bonačić-Koutecký.

However, due to the high computational cost, a full quantum mechanical solution is only possible for systems containing a few atoms. The number of DOFs and thus the computational cost can be decreased using classical or semiclassical approximations to describe the system evolving in time. In classical molecular dynamics (MD) a system is described by propagating only the nuclear DOFs in time using Newton's equation of motion. This level of description is useful for large systems and can be carried out on the nanosecond to microsecond time scale. Bond breaking and chemical reactions, however, can not be described simply through classical MD because the electronic structure is completely ignored.

A better alternative to describe chemical reactions evolving in time is the semiclassical approximation, which relies on a partitioning of the system into a classical and a quantum part. The classical part contains the slow DOFs while the quantum mechanical part contains the fast DOFs. In the following development, the conventional partitioning into classical and quantum parts will be used, that is the classical part refers to nuclear DOFs and the quantum part describes the electronic motion. Other partitionings might also be useful depending on the nature of the system.

One possibility of a semiclassical approximation is the mean-field Ehrenfest method that is based on an ansatz for the total time-dependent wavefunction  $\Psi(\mathbf{R}, \mathbf{r}, t)$  that consists of a product of the slow and fast DOFs, described by  $\chi(\mathbf{R}, t)$  and  $\psi(\mathbf{R}, \mathbf{r}, t)$ , respectively,

$$\Psi(\mathbf{R}, \mathbf{r}, t) = \psi(\mathbf{r}, t)\chi(\mathbf{R}, t)\exp(i/2\pi \int \langle \Psi | H | \Psi \rangle_{\mathbf{R}, \mathbf{r}} dt) \quad (2.16)$$

Substituting this ansatz into the time-dependent Schrödinger equation (2.15) and some further transformations [27] lead to Time-Dependent Self-Consistent Field (TDSCF) equations, which describe the motion of the fast DOFs in an average field of the slow DOFs and vice versa. Using the division of the Hamiltonian of (2.1) the TDSCF equations read

$$i \frac{\partial}{\partial t} \psi = \hat{T}_e + \langle \chi | \hat{V}_{NN} + \hat{V}_{Ne} + \hat{V}_{ee} | \chi \rangle \quad (2.17)$$

$$i \frac{\partial}{\partial t} \chi = \hat{T}_N + \langle \psi | \hat{H}_e | \psi \rangle \quad (2.18)$$

Finally the Ehrenfest method is achieved by taking the classical limit for nuclei in (2.17) leading to the two central equations

$$\mathbf{F} = M\ddot{\mathbf{R}} = -\nabla_{\mathbf{R}} \langle \psi | \hat{H}_e | \psi \rangle \quad (2.19)$$



$$i\frac{\partial}{\partial t}\psi(\mathbf{r}, t) = \hat{H}_e\psi(\mathbf{r}, t) \quad (2.20)$$

The first expression is used to propagate the nuclei, while the second one describes the electronic motion in the field of the nuclei. Using the Hellmann-Feynman theorem, (2.19) can be written in a more suitable way, if  $\psi$  is an exact eigenfunction of  $H_e$ . Then

$$\mathbf{F} = -\langle\psi|\nabla_{\mathbf{R}}\hat{H}_e|\psi\rangle. \quad (2.21)$$

If we assume that at time  $t_0$  the system is in a pure adiabatic state [ $\psi(\mathbf{R}, \mathbf{r}, t_0) = \Phi_k(\mathbf{R}, \mathbf{r})$ ], by propagating according to (2.20) it will evolve into a superposition of adiabatic states at later times

$$\psi(\mathbf{R}, \mathbf{r}, t) = \sum_k C_k(t)\Phi_k(\mathbf{R}, \mathbf{r}). \quad (2.22)$$

In many chemical reactions such an admixture of adiabatic states is physically unrealistic because no clearly defined chemical species can be associated with such a mixed state. In addition, the nuclear forces may be averaged over completely different species leading to unphysical nuclear forces and therefore to incorrect trajectories.

If we recover the BO approximation and propagate the system on a purely adiabatic state  $\Phi_k$  (2.21), we might have a good description of the nuclear motion and are able to identify a clear chemical species. For a wide range of chemical problems this treatment might provide an accurate description, but it neglects non-adiabatic effects.

The surface hopping (SH) method has been developed to overcome the problems of Ehrenfest and BO descriptions. In SH the slow DOFs are always propagated on a pure adiabatic PES, but non-adiabatic effects are incorporated by allowing transitions between the adiabatic states. To derive the working equations of the SH method we expand the time-dependent wavefunction in terms of adiabatic states according to (2.22). Substituting this ansatz into the time-dependent Schrödinger equation and further manipulations [27] yield a first order differential equation for the expansion coefficients

$$i\dot{C}_k(t) = \sum_{j=0}^{N_{ad}} C_j(t)[V_{kj} - i\dot{\mathbf{R}} \cdot \mathbf{d}_{kj}]. \quad (2.23)$$

The elements of the time-dependent density matrix are given by the coefficients

$$a_{kj} = C_k C_j^* \quad (2.24)$$

where the diagonal elements define the populations of the adiabatic states and the off diagonal elements are known as the coherence terms. Thus equation (2.23) describes the evolution of the state populations under the influence of the non-adiabatic coupling that enters by the derivative coupling vector  $\mathbf{d}_{kj}$ , previously defined in (2.9). Note that the scalar couplings (2.10) do not enter (2.23), because the coefficients  $C_i(t)$  only depend on time and not on nuclear coordinates in contrast to the  $\chi(\mathbf{R}, t)$  in the BO expansion (2.4).

SH methods differ in the way the probabilities for switching PES is evaluated. Tully [30] developed a way to compute a switching probability that minimizes the number of surface hops but represents the correct statistical distribution of the trajectories (“fewest switches criterion”). Taking this requirement into consideration, the probability of changing adiabatic states in the time interval  $\Delta$  reads

$$g_{k,j}(t, \Delta) = \max \left( 0, -2 \int_t^{t+\Delta} d\tau \frac{\Re[\tilde{C}_j(\tau) \tilde{C}_k^*(\tau) (\dot{\mathbf{R}} \cdot \mathbf{d}_{jk})(\tau)]}{\tilde{C}_k(\tau) \tilde{C}_k^*(\tau)} \right). \quad (2.25)$$

A trajectory is obtained by propagating the nuclei on an adiabatic surface. At each time step the hopping probability (2.25) is evaluated and compared to a number randomly chosen from the interval  $\theta \in [0, 1]$ . If  $\theta > g_{k,j}$  the system switches from adiabatic state  $k$  to  $j$ , and the forces are evaluated for the new electronic state until another surface hop occurs. An ensemble of trajectories generated in this way reflects the statistical distribution of the different reaction branches [30].

## Chapter 3

# Electronic Structure Methods

In this chapter the basic concepts of a few ground and excited state electronic structure methods that were used in this thesis are presented. More extensive information and derivations of the methods can be found in the following references. The wavefunction based approaches, Hartree-Fock (HF), Configuration Interaction (CI), Multi-Configurational Self-Consistent Field (MCSCF), and the Coupled Cluster (CC) method are described in detail in the book of Szabo and Ostlund [31] and the more recent book of Helgaker, Jørgensen and Olsen [32]. In addition, approximate CC methods and Linear Response Coupled Cluster (LR-CC) theory is reviewed in an article by Christiansen [33] but for a more detailed description the reader is referred to the original literature [34]. Density functional theory (DFT) is subject of many textbooks [35–38]. Several reviews about Time-Dependent Density Functional Theory (TDDFT) have been published [39, 40] and recently, also a textbook on TDDFT appeared [41]. A comparison between single-reference excited-states methods based on HF and DFT can be found in a recent review of Dreuw and Head-Gordon [42].

Modern electronic structure methods aim to solve as exactly as possible the time-independent electronic Schrödinger equation (2.2) using a non-relativistic Hamiltonian (2.3). Most wavefunction based methods, like HF, CI, MCSCF are based on the variational principle. In these methods the total energy is obtained by minimization of the expectation value of the Hamiltonian, i.e.,

$$E = \min \frac{\langle \Psi | \hat{H} | \Psi \rangle}{\langle \Psi | \Psi \rangle} \quad (3.1)$$

Variational methods have the advantage that the resultant energy is always an upper bound of the true

ground-state electronic energy. This is also true for exact DFT, which is also based on the variational principle. However, the approximations made for the exchange-correlation can lead to total energies that are not necessarily an upper bound of the true energy. In contrast CC methods are usually not formulated in a variational way but solve a projected Schrödinger equation. Some excited state methods like the Time-Dependent Hartree-Fock (TDHF), linear response TDDFT (LR-TDDFT), and LR-CC use the linear response of a reference state to a perturbation to obtain energies and properties of excited states.

### 3.1 The Hartree-Fock Approximation

One of the simplest approximations for solving the stationary Schrödinger equation for a  $N$ -electron system is provided by Hartree-Fock (HF) theory. The approximation consists of treating the interaction between one electron with the remaining  $N-1$  electrons, represented as a mean field. This is done by approximating the many electron ground-state wavefunction  $\Psi_0$  by an antisymmetrized product of *non-interacting* spin orbitals  $\chi(\mathbf{x}_i) = \phi(\mathbf{r})\sigma(s)$ , with  $\sigma(s) = \alpha(s), \beta(s)$ , where  $\mathbf{x}_i$  collects spatial coordinates  $\mathbf{r}$  and spin coordinates  $s$  of electron  $i$ . An antisymmetrized product changes sign if any of the two electrons are interchanged. This property is necessary because of the fermionic nature of the electrons. In practice such an  $N$ -electron wavefunction is constructed by ordering the orbitals in a *Slater determinant*  $\Phi_{SD}$ , i.e.,

$$\Psi_0 \approx \Phi_{SD}(\mathbf{x}_1, \mathbf{x}_2, \dots, \mathbf{x}_N) = \frac{1}{\sqrt{N!}} \begin{vmatrix} \chi_1(\mathbf{x}_1) & \chi_2(\mathbf{x}_1) & \cdots & \chi_N(\mathbf{x}_1) \\ \chi_1(\mathbf{x}_2) & \chi_2(\mathbf{x}_2) & \cdots & \chi_N(\mathbf{x}_2) \\ \vdots & \vdots & \ddots & \vdots \\ \chi_1(\mathbf{x}_N) & \chi_2(\mathbf{x}_N) & \cdots & \chi_N(\mathbf{x}_N) \end{vmatrix}. \quad (3.2)$$

For simplicity, let us consider a closed shell system with doubly occupied spatial orbitals  $\phi_i(\mathbf{r})$ . In this case we can neglect the spin part  $\sigma(s)$  from the following development (see Chapter 3.4 of Ref. [31]). According to the variational principle, minimization of the electronic energy using this ansatz provides

an upper bound for the ground-state energy within the HF approximation. The HF energy reads

$$E_{HF} = \min \langle \Phi_{SD} | \hat{H}_e | \Phi_{SD} \rangle = 2 \sum_i^{N/2} \langle \phi_i | \hat{h} | \phi_i \rangle + \sum_{ij}^{N/2} [2(ii|\hat{f}_H|jj) - (ij|\hat{f}_H|ji)], \quad (3.3)$$

with the one-electron operator  $\hat{h}_i$  containing the kinetic energy operator and the Coulomb interaction between the electron and the nuclear charges  $Z_A$  at positions  $\mathbf{R}_A$

$$\hat{h}_i = -\frac{1}{2} \nabla_i^2 - \sum_A \frac{Z_A}{|\mathbf{r}_i - \mathbf{R}_A|} \quad (3.4)$$

and the Hartree kernel describes the electron-electron interactions

$$\hat{f}_H = \hat{f}_H(\mathbf{r}, \mathbf{r}') = \frac{1}{|\mathbf{r} - \mathbf{r}'|} \quad (3.5)$$

The electron repulsion integrals on the right hand side of (3.3) are written in the Mulliken notation

$$(rs|\hat{f}|pq) = \int \int \phi_r^*(\mathbf{r}) \phi_s(\mathbf{r}) \hat{f}(\mathbf{r}, \mathbf{r}') \phi_p^*(\mathbf{r}') \phi_q(\mathbf{r}') d\mathbf{r} d\mathbf{r}' \quad (3.6)$$

Minimization is usually done by solving the one-electron HF equations in a self-consistent manner

$$\hat{f}_i \phi_i(\mathbf{r}) = \epsilon_i \phi_i(\mathbf{r}), \quad (3.7)$$

where  $\hat{f}$  is the closed-shell Fock operator containing the Coulomb and exchange operators  $\hat{J}$  and  $\hat{K}$

$$\hat{f}_i = \hat{h}_i + \sum_j^{N/2} [2\hat{J}_j - \hat{K}_j], \quad (3.8)$$

$$\hat{K}_j(\mathbf{r}) \phi_i(\mathbf{r}) = \left[ \int d\mathbf{r}' \frac{\phi_j^*(\mathbf{r}') \phi_i(\mathbf{r}')}{|\mathbf{r} - \mathbf{r}'|} \right] \phi_j(\mathbf{r}), \quad (3.9)$$

$$\hat{J}_j(\mathbf{r}) \phi_i(\mathbf{r}) = \left[ \int d\mathbf{r}' \frac{\phi_j^*(\mathbf{r}') \phi_j(\mathbf{r}')}{|\mathbf{r} - \mathbf{r}'|} \right] \phi_i(\mathbf{r}). \quad (3.10)$$

$\epsilon_i$  are the orbital energies. In the initial ansatz (3.2), HF does not account for electron correlation. The difference between  $E_{HF}$  of a system and its true energy  $E_0$  defines the *correlation energy*

$$E_C = E_0 - E_{HF}. \quad (3.11)$$

## 3.2 The Time-Dependent Hartree-Fock Method

The Time-Dependent HF method (TDHF) provides an extension of the HF method to describe electronically excited states. In analogy to ground-state HF, TDHF assumes that the time-dependent many electron state can be approximated by an SD  $\Phi_{SD}(\tilde{\mathbf{r}}, t)$  of time-dependent orbitals  $\phi_i(\mathbf{r}, t)$ . Consider the time-dependent electronic Schrödinger equation

$$\hat{H}(t)\Psi(\tilde{\mathbf{r}}, t) = i\frac{\partial}{\partial t}\Psi(\tilde{\mathbf{r}}, t) \quad (3.12)$$

with a time-dependent electronic Hamiltonian  $\hat{H}(\tilde{\mathbf{r}}, t) = \hat{H}_e(\tilde{\mathbf{r}}) + \hat{V}(\tilde{\mathbf{r}}, t)$ , containing a time-dependent single particle potential  $\hat{V}(\tilde{\mathbf{r}}, t)$ , for instance an oscillating electromagnetic field. The vector  $\tilde{\mathbf{r}}$  collects all the spatial coordinates of the individual electrons. Substitution of a time-dependent SD yields the equivalent time-dependent Schrödinger equation formulated for non-interacting electrons:

$$\hat{F}(\tilde{\mathbf{r}}, t)\Phi_{SD}(\tilde{\mathbf{r}}, t) = i\frac{\partial}{\partial t}\Phi_{SD}(\tilde{\mathbf{r}}, t), \quad (3.13)$$

where  $\hat{F}(\tilde{\mathbf{r}}, t)$  is defined as

$$\hat{F}(\tilde{\mathbf{r}}, t) = \sum_i \hat{f}_i(\mathbf{r}) + \hat{V}(\tilde{\mathbf{r}}, t) \quad (3.14)$$

In the time-dependent Fock operator  $\hat{F}$  the Coulomb and exchange operators, (3.10), (3.9) are defined using orbitals  $\phi_i(\mathbf{r}, t)$ , that also depend on time. To obtain the TDHF equations, linear response (LR) time-dependent perturbation theory is applied to solve (3.13). Therefore one assumes that at time  $t = 0$  the system is described by a time-independent SD. If a small perturbation  $\hat{V}(\mathbf{r}, t)$  is turned on, the time-dependent response of the orbitals can be assumed to be sufficiently described by the linear part of the

response. This treatment yields the non-Hermitian eigenvalue equation [42]

$$\begin{bmatrix} \mathbf{A} & \mathbf{B} \\ \mathbf{B} & \mathbf{A} \end{bmatrix} \begin{pmatrix} \mathbf{X}_I \\ \mathbf{Y}_I \end{pmatrix} = \omega_I \begin{bmatrix} +1 & \mathbf{0} \\ \mathbf{0} & -1 \end{bmatrix} \begin{pmatrix} \mathbf{X}_I \\ \mathbf{Y}_I \end{pmatrix}, \quad (3.15)$$

also known as the LR-TDHF equations in the random phase approximation (RPA). The matrix elements of  $\mathbf{A}$  and  $\mathbf{B}$  are given by

$$A_{ia,jb} = \delta_{i,j}\delta_{a,b}(\epsilon_a - \epsilon_i) + 2 \left( ia|\hat{f}_H|jb \right) - \left( ij|\hat{f}_H|ba \right) \quad (3.16)$$

$$B_{ia,jb} = \left( ia|\hat{f}_H|bj \right) - \left( ib|\hat{f}_H|aj \right), \quad (3.17)$$

where  $i$  and  $j$  refer to occupied orbitals, and  $a$  and  $b$  to unoccupied ones. The response vectors  $\mathbf{X}_I$  and  $\mathbf{Y}_I$  can be used to interpret the excited state by means of singly excited determinants.

A simplification of (3.15) can be achieved by setting  $\mathbf{B} = 0$ , leading to the simpler Hermitian eigenvalue problem known as the Tamm-Dancoff approximation (TDA)

$$\mathbf{A}\mathbf{X}_I = \omega_I\mathbf{X}_I. \quad (3.18)$$

It can be shown that this equation yields the excitation energies equivalent to those obtained by the variational Configuration Interaction Singles (CIS) method [42].

### 3.3 The Configuration Interaction Method

In Configuration Interaction [31] the ansatz for the many electron wavefunction reads

$$\begin{aligned} |\Psi_{\text{CI}}\rangle &= c_0|\Phi_{\text{HF}}\rangle + \sum c_a^r|\Phi_a^r\rangle + \sum c_{ab}^{rs}|\Phi_{ab}^{rs}\rangle + \sum c_{abc}^{rst}|\Phi_{abc}^{rst}\rangle + \dots \\ &= c_0|\Phi_{\text{HF}}\rangle + \sum c_S|S\rangle + \sum c_D|D\rangle + \sum c_T|T\rangle + \dots \end{aligned} \quad (3.19)$$

where  $|\Phi_{\text{HF}}\rangle$  is the HF ground state and  $|\Phi_a^r\rangle, |\Phi_{ab}^{rs}\rangle, |\Phi_{abc}^{rst}\rangle, \dots$  refer to singly, doubly, triply, ..., excited determinants, constructed from the optimized HF orbitals. The sums in (3.19) run over all possible excitations of the corresponding order. This ansatz leads to an exact representation of the many electron

wavefunction, provided that all possible determinants are included. The CI method consists of finding the coefficients  $c_i$  in ansatz (3.19), that minimize the expectation value of the total energy

$$E_{\text{CI}} = \min_{c_0, c_S, \dots} \frac{\langle \Psi_{\text{CI}} | \hat{H}_e | \Psi_{\text{CI}} \rangle}{\langle \Psi_{\text{CI}} | \Psi_{\text{CI}} \rangle} \quad (3.20)$$

When all excitations in a given basis set are included, the method is known as *full CI* (FCI). Because the number of determinants increases rapidly with each order of excitation, FCI calculations are computationally very demanding and can only be carried out for systems containing a few atoms. However, since the method can in principle provide exact results, it is often used as benchmark. In practice, the FCI expansion is usually truncated at a certain order of excitation. For instance, the CIS method only includes singly excited determinants, while the CISD and CISDT method include single and double excitations, and single, double, and triple excitations, respectively. Truncation of the CI expansion leads to a description which is not size-extensive.

In the CIS method for excited states the ansatz for the many electron state includes only singly excited determinants

$$|\Psi_{\text{CIS}}\rangle = \sum_{ai} c_a^i |\Phi_a^i\rangle. \quad (3.21)$$

Minimization of expression (3.20) using ansatz (3.21) yields the singlet excitation energies

$$\sum_{ai} \langle \Phi_j^b | \hat{H} | \Phi_i^a \rangle = E_{\text{CIS}} \sum_{ia} c_i^a \delta_{ij} \delta_{ab}. \quad (3.22)$$

The excitation energies in CIS are defined relative to the HF ground state

$$\omega_{\text{CIS}} = E_{\text{CIS}} - E_{\text{HF}}. \quad (3.23)$$

$\omega_{\text{CIS}}$  can also be obtained by solving the eigenvalue problem of TDHF in the TDA (3.18) [43].



### 3.4 Multi-Configurational Self-Consistent Field Method

Multi-Configurational Self-Consistent Field (MCSCF) methods are related to the CI method because they also use a multi-determinantal ansatz to describe the many electron wavefunction:

$$|\Psi_{\text{MCSCF}}\rangle = \sum_k c_k |\Phi_k\rangle, \quad (3.24)$$

where  $k$  is a general index denoting all chosen excited determinants. While CI uses fixed HF orbitals and optimization only concerns the expansion coefficients,  $c_i$  in (3.19), the MCSCF method also minimizes the energy in conjunction with an optimization of the orbitals  $\phi_i$ , that enter  $\Phi_k$

$$E_{\text{MCSCF}} = \min_{c_k, \phi_i} \frac{\langle \Psi_{\text{MCSCF}} | \hat{H}_e | \Psi_{\text{MCSCF}} \rangle}{\langle \Psi_{\text{MCSCF}} | \Psi_{\text{MCSCF}} \rangle}. \quad (3.25)$$

This leads to higher accuracy with the same number of basis functions than in CI. The Complete Active Space Self-Consistent Field (CASSCF) method is a special version of the MCSCF method, in which a chemically active space is defined. The active space contains a limited number of occupied and unoccupied orbitals. The determinants  $\Phi_k$  refer to all possible configurations that are obtained by distributing the electrons of the active occupied orbitals within the active space.

Excited state energies of states with different symmetry than the ground state can be obtained by restricting the active space in such a way that the resulting determinants  $\Phi_k$  have the same symmetry as the state of interest.

The state averaging (SA) method, provides a way to obtain simultaneously the energies of different states that have the same symmetry. In the SA-CASSCF approach an energy function is minimized that consists in a sum of non-interacting orthonormal configurations  $\Psi_i$

$$E_{\text{SA}} = \sum_i w_i \langle \Psi_i^{\text{SA}} | \hat{H} | \Psi_i^{\text{SA}} \rangle \quad (3.26)$$

that are weighted by  $w_i$ . The orbitals are simultaneously optimized for several electronic states and are thus not optimal for each electronic state [32]. Therefore the obtained ground state energy  $E_0^{\text{SA-CASSCF}}$

is an upper bound to the conventional CASSCF energy

$$E_0^{\text{CASSCF}} \leq E_0^{\text{SA-CASSCF}}. \quad (3.27)$$

### 3.5 Coupled Cluster Methods

The coupled cluster (CC) ansatz is based on the FCI ansatz (3.19), but has the advantage that it provides a size-extensive description even at truncated level and converges faster to the FCI limit than do truncated CI methods. To derive the CC ansatz we may write the FCI ansatz in form of a product [32]

$$|\Psi_{\text{FCI}}\rangle = |\Psi_{\text{CC}}\rangle = \left[ \prod_{ai} (1 + \hat{X}_i^a) \right] \left[ \prod_{a>b, i>j} (1 + \hat{X}_{ij}^{ab}) \right] \dots |\Phi_{\text{HF}}\rangle. \quad (3.28)$$

where  $\hat{X}_i^a$ ,  $\hat{X}_{ij}^{ab}$ , ... are excitation operators times an expansion coefficient  $c_\mu$ , using the notation of second quantization [32] they read

$$\begin{aligned} \hat{X}_i^a &= c_i^a \hat{a}_a^\dagger \hat{a}_i \\ \hat{X}_{ij}^{ab} &= c_{ij}^{ab} \hat{a}_a^\dagger \hat{a}_b^\dagger \hat{a}_i \hat{a}_j. \end{aligned} \quad (3.29)$$

Note that the coefficients  $c_\mu$  differ from the coefficients  $c_k$  in the CI ansatz (3.19). By using a Taylor expansion of the exponential, (3.28) can be transformed leading to the CC ansatz for the wavefunction [32]:

$$|\Psi_{\text{CC}}\rangle = \exp(\hat{T}) |\Phi_{\text{HF}}\rangle, \quad (3.30)$$

where the cluster operator of a  $N$  electron system is defined as

$$\hat{T} = \hat{T}_1 + \hat{T}_2 + \hat{T}_3 + \hat{T}_4 + \dots + \hat{T}_N = \sum_{\mu} t_{\mu} \hat{\tau}_{\mu}. \quad (3.31)$$

The excitation operators  $\hat{\tau}_{\mu}$  and their associated cluster amplitudes  $t_{\mu}$  correspond to a given degree of excitation, for instance single, double or triple excitations. In the notation of second quantization the

cluster operators for singles and doubles,  $\hat{T}_1$  and  $\hat{T}_2$ , are given by

$$\hat{T}_1 = \sum_{ai} t_i^a \hat{a}_a^\dagger \hat{a}_i = \sum_{ai} t_i^a \hat{\tau}_i^a \quad (3.32)$$

$$\hat{T}_2 = \frac{1}{4} \sum_{aibj} t_{ij}^{ab} \hat{a}_a^\dagger \hat{a}_i \hat{a}_b^\dagger \hat{a}_j = \sum_{aibj} t_{ij}^{ab} \hat{\tau}_{ij}^{ab}. \quad (3.33)$$

The faster convergence to the FCI limit in case of truncation arises from the fact that even if series (3.31) is truncated at a given excitation level, the CC ansatz still contains contributions from all FCI determinants through the indirect, or *disconnected* clusters. To illustrate this, we write the exponential ansatz in form of the expansion in which the excitation levels are ordered in a different way than before

$$\exp(\hat{T})|\Phi_{HF}\rangle = \sum_i^N \hat{C}_i |\Phi_{HF}\rangle, \quad (3.34)$$

where

$$\hat{C}_0 = 1 \quad (3.35)$$

$$\hat{C}_1 = \hat{T}_1 \quad (3.36)$$

$$\hat{C}_2 = \hat{T}_2 + \frac{1}{2} \hat{T}_1^2 \quad (3.37)$$

$$\hat{C}_3 = \hat{T}_3 + \hat{T}_1 \hat{T}_2 + \frac{1}{6} \hat{T}_1^3 \quad (3.38)$$

$$\hat{C}_4 = \hat{T}_4 + \hat{T}_1 \hat{T}_3 + \frac{1}{2} \hat{T}_2^2 + \frac{1}{2} \hat{T}_1^2 \hat{T}_2 + \frac{1}{24} \hat{T}_1^4. \quad (3.39)$$

For instance, if we only include excitations up to  $\hat{T}_2$ , a part of the  $\hat{C}_4|\Phi_{HF}\rangle$  determinant is included through the disconnected  $\hat{T}_2$  and  $\hat{T}_1$  excitations that appear in (3.39). The commonly used truncation levels are  $\hat{T} = \hat{T}_1$  for CCS,  $\hat{T} = \hat{T}_1 + \hat{T}_2$  for CCSD, and  $\hat{T} = \hat{T}_1 + \hat{T}_2 + \hat{T}_3$  for CCSDT.

Because of the non-linear parametrisation of the Coupled Cluster model (3.28), variational optimization of the wavefunction leads to complicated functions and can only be performed for very small systems [32]. In an alternative approach the Coupled Cluster energy is obtained by projection onto the HF reference state

$$E_{CC} = \langle \Phi_{HF} | \hat{H} \exp(\hat{T}) | \Phi_{HF} \rangle. \quad (3.40)$$

Therefore the CC method cannot be considered as variational. The cluster amplitudes are obtained by projection onto the excited determinants  $\mu$

$$\langle \mu | \exp(-\hat{T}) \hat{H} \exp(\hat{T}) | \Phi_{\text{HF}} \rangle = 0. \quad (3.41)$$

The number of equations determined by (3.41) is equal to the number of connected clusters and thus depends on the truncation level of the CC approximation.

Using perturbation theory, excitations of higher order than the actual truncation level can be estimated, leading to the second-order approximate CC models, CC2 and CC3. CC2 provides an approximation for CCSD, while CC3 approximates CCSDT. In contrast to non-iterative perturbative approaches like MP2 or CCSD(T), the CC2 and CC3 models can be used to obtain frequency dependent properties through linear response time-dependent perturbation theory and are therefore suited to treat electronically excited states [33].

### 3.6 Kohn-Sham Density Functional Theory

In density functional theory (DFT) the central quantity is the electronic (spin) density  $n(x, y, z)$ , that depends only on 3 spatial coordinates plus a spin coordinate in the case of spin polarized DFT. This provides a considerable simplification compared to wavefunction based methods, in which the  $N$ -electron wavefunction depends on  $3 \times N$  spatial plus  $N$  spin coordinates. The two Hohenberg-Kohn (HK) theorems [44], provide a way to determine the properties of a system only on the basis of its electron density.

The first theorem states that the external potential  $V_{ext}$  of a system is (up to a constant) uniquely determined by the ground-state density  $n_0$ . Since  $\hat{H}$  depends on  $V_{ext}$ , it depends also on the density and therefore the true electronic ground state and all its properties are determined by  $n_0$ .

$$n_0 \Rightarrow \{N, Z_A, \mathbf{R}_A\} \Rightarrow \hat{H} \Rightarrow \Psi_0 \Rightarrow E_0. \quad (3.42)$$

Thus the ground-state energy  $E_0$  can be written as a functional of  $n_0$ ,

$$E_0[n_0] = E_{Ne}[n_0] + T[n_0] + E_{ee}[n_0] \quad (3.43)$$

that can be split into a system dependent part  $E_{Ne}$ , defined by the positions  $\mathbf{R}_A$  and charges  $Z_A$  of the nuclei through the external potential  $V_{ext}$ , and a system independent part, containing the kinetic energy of the electrons  $T[n]$  and the electron-electron interaction  $E_{ee}[n]$ . The system independent functional is called the *universal* or *HK functional*

$$F[n] = T[n] + E_{ee}[n]. \quad (3.44)$$

The second HK theorem provides a way to determine the true ground-state density  $n_0$  of a system. Based on the variational principle, it states that the trial density  $\tilde{n}$ , that minimizes the ground-state energy functional  $E_0$ , is equal to the true ground-state density  $n_0$  of the system. Therefore, any density  $\tilde{n}$ , that satisfies certain boundary conditions, provides an upper bound of the true ground-state energy

$$E[\tilde{n}] = \int V_{ext}(\mathbf{r})\tilde{n}(\mathbf{r})d\mathbf{r} + F[\tilde{n}] \geq E_0 = E[n_0]. \quad (3.45)$$

Provided that we know the expression for the universal functional we are in principle able to search for the ground-state energy, by minimizing  $E[\tilde{n}]$  in some way. Still, we do not know the exact dependence of the electronic kinetic energy on the density and so no exact relationship between the non-classical electron-electron interaction and the density is known.

The Kohn-Sham (KS) approach [45] provides a way of evaluating the largest parts of the unknown terms. In this approach,  $T[n]$  and  $E_{ee}[n]$  are split each into two parts

$$T[n] = T_S[\{\phi_i\}] + T_C[n] \quad (3.46)$$

$$E_{ee}[n] = J[n] + E_{ncl}[n]. \quad (3.47)$$

$T_S[\{\phi_i\}]$  denotes the electronic kinetic energy of a non-interacting reference system and  $E_{ncl}$  stands for the non-classical electron-electron interaction terms. The electrons of the non-interacting system are described by orbitals  $\phi_i$ , satisfying

$$\sum_i^N |\phi_i(\mathbf{r})|^2 = n(\mathbf{r}), \quad (3.48)$$

where it is assumed that the density of the reference system  $n$  is equal to the true density  $n_0$  of the

system ( $n = n_0$ ).  $T_C$  is defined as the difference between the kinetic energy of the interacting system and  $T_S$  and arises due to the interaction of the electrons including all quantum effects. The advantage of this splitting is that by introducing non-interacting orbitals  $\phi_i$  that integrate to  $n$ ,  $T_S$  can be determined in the same way as in HF theory

$$T_S[\phi_i] = -\frac{1}{2} \sum_i \langle \phi_i | \nabla^2 | \phi_i \rangle \quad (3.49)$$

The term  $J[n]$  in the second equation is just the classical Coulomb energy

$$J[n] = \frac{1}{2} \int \int \frac{n(\mathbf{r})n(\mathbf{r}')}{|\mathbf{r} - \mathbf{r}'|} d\mathbf{r}d\mathbf{r}' \quad (3.50)$$

and  $E_{ncl}$  is the non-classical contribution of the electron-electron interaction energy. The remaining quantities  $E_{ncl}[n]$  and  $T_C[n]$  are still unknown. However, the KS approach relies on the assumption that these two quantities are rather small compared to the other terms and that they can be approximated in some way. By defining the *exchange correlation* functional  $E_{xc}[n]$

$$E_{xc}[n] = T_C[n] + E_{ncl}[n], \quad (3.51)$$

the HK functional can be rewritten as

$$F[n] = T_S[\{\phi_i\}] + J[n] + E_{xc}[n]. \quad (3.52)$$

Provided we have an approximation for  $E_{xc}$ , the ground-state energy  $E_0$  can be found by minimizing the functional

$$\begin{aligned} E_0[n] &= E_{Ne}[n] + T_S[\phi_i] + J[n] + E_{xc}[n] \\ &= -\sum_i \int \sum_A \frac{Z_A}{|\mathbf{R}_A - \mathbf{r}|} |\phi_i(\mathbf{r})|^2 d\mathbf{r} \\ &\quad -\frac{1}{2} \sum_i \langle \phi_i | \nabla^2 | \phi_i \rangle \\ &\quad + \frac{1}{2} \sum_i \sum_j \int \int |\phi_i(\mathbf{r})|^2 \frac{1}{r_{ij}} |\phi_j(\mathbf{r}')|^2 d\mathbf{r}d\mathbf{r}' + E_{xc}[n]. \end{aligned} \quad (3.53)$$

Similarly to HF theory, minimization of  $E_0$  can be carried out by solving self-consistently a set of

equations, for non-interacting electrons moving in an effective potential  $V_{eff}$

$$\left[-\frac{1}{2}\nabla^2 + V_{eff}(\mathbf{r})\right]\phi_i(\mathbf{r}) = \epsilon_i\phi_i(\mathbf{r}) \quad (3.54)$$

that yields the optimal non-interacting orbitals. The difference with HF theory lies in the form of the effective potential

$$V_{eff}(\mathbf{r}) = V_{xc}(\mathbf{r}) + \int \frac{n(\mathbf{r}')}{|\mathbf{r}' - \mathbf{r}|} d\mathbf{r}' - \sum_A \frac{Z_A}{|\mathbf{R}_A - \mathbf{r}|} \quad (3.55)$$

with

$$V_{xc} = \frac{\delta E_{xc}[n]}{\delta n}. \quad (3.56)$$

The optimized orbitals  $\phi_i$  of (3.54), are called *Kohn-Sham* orbitals and differ from the HF orbitals.

The remaining task consists in finding a good approximation for the exchange-correlation term. At present, a large variety of xc-functionals exist relying on different assumptions. The major approaches are outlined here. The first and simplest approximation is based on the xc-expression for the homogeneous electron gas which has been computed exactly by Quantum Monte-Carlo. This approach is usually denoted as the local density approximation (LDA), as it is local in sense that  $E_{xc}^{LDA}[n(\mathbf{r})]$  depends only  $n(\mathbf{r})$ . In the generalized gradient approximation (GGA) the expression is refined and depends on  $n(\mathbf{r})$  and its gradient  $\nabla n(\mathbf{r})$  ( $E_{xc}^{GGA}[n(\mathbf{r}), \nabla n(\mathbf{r})]$ ). Hybrid approaches mix a GGA functional to some extent  $c_X$  with exact (“Hartree-Fock”) exchange  $E_x^X$

$$E_{xc}^{hybrid} = c_X E_x^X + (1 - c_X) E_x^{GGA} + E_c^{GGA} \quad (3.57)$$

The three approaches described here are often referred to as *conventional* xc-functionals. Further information on xc-functionals can be found for instance in Chapter 6 of Ref. [37].

## 3.7 Time-Dependent Density Functional Theory

### 3.7.1 The Time-Dependent Kohn-Sham Equations

In analogy to the first HK theorem of ground-state DFT, the Runge-Gross theorem [19] states that there exists a one-to-one mapping between the time-dependent one-body density  $n(\mathbf{r}, t)$  and the time-

dependent external potential  $V_{ext}(\mathbf{r}, t)$  plus a spatially constant purely time-dependent function  $C(t)$ . Up to a phase factor  $\alpha$ , the time-dependent wavefunction is then determined by the initial stationary wavefunction  $\Psi(t_0)$  and the time-dependent density  $n(\mathbf{r}, t)$

$$\Psi(t) = \Psi[n, \Psi(t_0)] \exp[-i\alpha(t)] \quad (3.58)$$

In the original formulation of Runge and Gross, an analog to the second HK theorem for the time-dependent case was derived by making the Dirac-Frenkel action stationary. However, this formalism was proved to violate the causality principle. Van Leeuwen proposed a different formalism based on the Keldysh formalism [46, 47].

By introducing again a fictitious system with non-interacting electrons in orbitals  $\phi_i(\mathbf{r}, t)$  we can write down the time-dependent KS equations

$$\left[-\frac{1}{2}\nabla^2 + V_{eff}(\mathbf{r}, t)\right]\phi_i(\mathbf{r}, t) = i\frac{\partial}{\partial t}\phi_i(\mathbf{r}, t) \quad (3.59)$$

where

$$V_{eff}(\mathbf{r}, t) = V_{ext}(\mathbf{r}, t) + \int \frac{n(\mathbf{r}', t)}{|\mathbf{r} - \mathbf{r}'|} d\mathbf{r}' + V_{xc}(\mathbf{r}, t) \quad (3.60)$$

Usually applications of TDDFT imply the *adiabatic* approximation (ALDA) in which the exchange-correlation potential is approximated as

$$V_{xc}[n](\mathbf{r}, t) \approx \frac{\delta E_{xc}[n_t]}{\delta n_t(\mathbf{r})} = V_{xc}[n_t](\mathbf{r}) \quad (3.61)$$

where  $n_t$  denotes the density evaluated at one particular time  $t$ . The xc-potential is thus independent of the time evolution of the density but depends only on the density at that particular time. This approximation assumes that the xc-potential instantaneously follows changes in the charge density, neglecting all kinds of retardation effects.

### 3.7.2 Linear Response TDDFT

If the system is perturbed by a weak electric field at time  $t = 0$ , the evolution of the density can be described by propagating the time-dependent KS equations. The Fourier transform of the time dependent



dipole moment in response to a delta function impulse yields the optical absorption of the system. However, assuming that the perturbation is weak we can also apply linear response theory, which is done by most quantum chemistry codes. This treatment has the advantage that it is formulated on the basis of pure ground state properties. If we apply a perturbation  $v_{appl}(\mathbf{r}, t)$  to the system, linear response TDDFT (LR-TDDFT) consists in evaluating the first order change of the density  $\delta n$ , which is related to the linear response of the density matrix  $\delta P(\omega)$  of the KS reference system:

$$\delta n(\mathbf{r}) = \sum_{ij}^{\text{all orbitals}} \phi_i(\mathbf{r}) \delta P_{ij} \phi_j(\mathbf{r}) \quad (3.62)$$

The *generalized susceptibility* of the non-interacting reference system reads

$$\chi_{ij} = \frac{f_i - f_j}{\omega - (\epsilon_j - \epsilon_i)}, \quad (3.63)$$

where  $\epsilon_i$  are the energies of the orbitals and  $f_i$  their occupation numbers.

The generalized susceptibility connects the first order change of the effective potential  $\delta v_{ij}^{eff}(\omega)$  with the first order change of the density matrix:

$$\delta P_{ij}(\omega) = \frac{f_i - f_j}{\omega - (\epsilon_i - \epsilon_j)} \delta v_{ij}^{eff}(\omega) \quad (3.64)$$

Here,  $\delta v_{ij}^{eff}(\omega)$  contains the frequency dependent perturbation  $v_{appl}(\omega)$  and the linear response of the SCF potential  $\delta v_{ij}^{SCF}$ , which in turn, can be evaluated by  $\delta P(\omega)$  and the coupling matrix  $K_{ij}$ ,

$$\delta v_{ij}^{SCF} = \sum_{kl} K_{ij,kl}(\omega) \delta P_{kl} \quad (3.65)$$

The coupling matrix is defined as

$$K_{ij,kl} = 2(ij|f_H|kl) + (ij|f_{XC}|kl), \quad (3.66)$$

and is determined by purely ground state properties through the Hartree kernel  $f_H$  (3.5) and the xc-kernel, defined as

$$f_{XC}(\mathbf{r}, \mathbf{r}') = \frac{\delta^2 E_{XC}[n]}{\delta n(\mathbf{r}) \delta n(\mathbf{r}')}, \quad (3.67)$$

when the ALDA is used.

Assuming that the perturbation takes the form of an oscillating time-dependent electric field,  $\delta P(\omega)$  can be used to compute the tensor components of the frequency dependent dynamic polarizability. Excitation energies are obtained as the poles of the dynamic polarizability. Determination of these poles and thus of the excitation energies can be done by solving the following matrix equations, also known as the Casida equations [20]

$$\begin{bmatrix} \mathbf{A} & \mathbf{B} \\ \mathbf{B} & \mathbf{A} \end{bmatrix} \begin{pmatrix} \mathbf{X}_I \\ \mathbf{Y}_I \end{pmatrix} = \omega_I \begin{bmatrix} +1 & \mathbf{0} \\ \mathbf{0} & -1 \end{bmatrix} \begin{pmatrix} \mathbf{X}_I \\ \mathbf{Y}_I \end{pmatrix}, \quad (3.68)$$

where the matrices  $\mathbf{A}$  and  $\mathbf{B}$  are defined as

$$\begin{aligned} A_{ia,jb} &= \delta_{i,j} \delta_{a,b} (\epsilon_a - \epsilon_i) + 2 (ia|f_H|jb) \\ &\quad - c_X (ij|f_H|ab) \\ &\quad + (1 - c_X) (ia|f_X|jb) \\ &\quad + (ia|f_C|jb) \\ B_{ia,jb} &= 2 (ia|f_H|bj) - c_X (ib|f_H|aj) \\ &\quad + (1 - c_X) (ia|f_{XC}|bj) \\ &\quad + (ia|f_C|bj). \end{aligned} \quad (3.69)$$

The two matrices have been defined for a general hybrid XC-functional (Eq. 3.57) with an amount  $c_X$  of exact exchange, where  $f_X$  and  $f_C$  are the GGA exchange and correlation kernels, defined in analogy to (3.67). By setting  $c_X = 1$  and neglecting the term containing  $\hat{f}_C$ , we recover the TDHF equations (3.17).

In the same way the TDA is achieved in TDHF by setting the matrix  $\mathbf{B} = 0$ , also TDDFT-TDA can be obtained. The TDDFT-TDA provides a simplification of the eigenvalue problem and has been shown to give similar results as the full LR-TDDFT treatment for most closed shell systems at equilibrium geometries. In contrast to the TDA to TDHF, which can also be derived by the CIS method, no other route exists in deriving the TDDFT-TDA. The connections between TDHF, CIS, TDDFT, and TDDFT-TDA are schematically summarized in Fig. 3.1. TDDFT-TDA has even been shown to give more reasonable

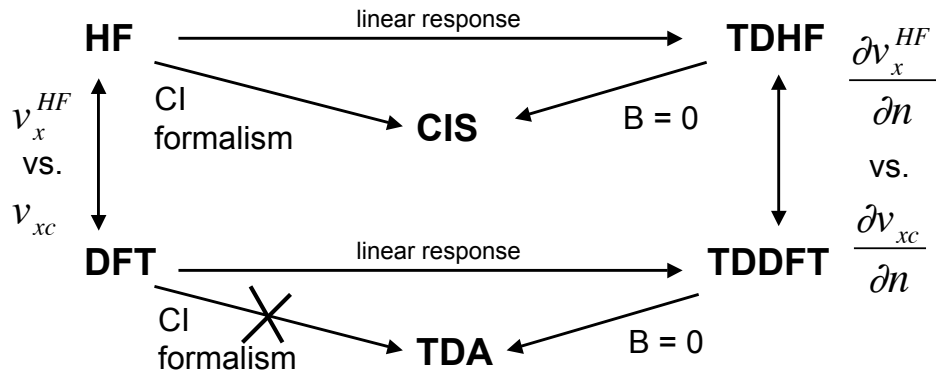


Figure 3.1: Connection between the different excited state methods based on HF and DFT. Picture according to Ref. [42].

results in regions where the LR-TDDFT treatment exhibits triplet or singlet instabilities [48, 49]. However, one should keep in mind that TDHF and TDDFT both obey the Thomas-Reiche-Kuhn rule for the oscillator strengths, which is not the case for CIS and TDDFT/TDA [20].



## Chapter 4

# Trajectory surface hopping within linear response TDDFT

### Abstract

A fewest switches trajectory surface hopping algorithm based on linear response time-dependent density functional theory is developed and implemented into the plane wave *ab initio* molecular dynamics package CPMD. A scheme to calculate non-adiabatic couplings using a multi determinantal approximation of the excited state wavefunction is introduced. The method is applied to the study of the photorelaxation of protonated formalimine, a minimal model of the rhodopsin chromophore retinal. A good agreement of the structural and dynamic behavior is found with respect to state averaged multiconfiguration self consistent field based trajectory surface hopping.

### 4.1 Introduction

*Ab initio* molecular dynamics (AIMD) [13] has become an established tool to study physical and chemical processes in condensed matter physics and molecular sciences. Because of its modest computational cost, Kohn-Sham (KS) density functional theory (DFT) [44] is currently the preferred electronic structure method for AIMD. Most DFT-AIMD simulations are performed in the ground state, but recently also excited state dynamics has become available.

Several time-independent KS DFT methods, like for instance  $\Delta$ SCF or the restricted open shell KS

(ROKS) [17] approach, have been proposed to approximate excited state energies (for a review see [20, 39]) and forces [17, 50]. Although these methods perform well in certain cases, the assumptions made are difficult to justify in general [20, 39]. In this work, we use time-dependent DFT (TDDFT) [19, 20, 39] which corresponds to an exact reformulation of time-dependent (TD) quantum mechanics. Within linear response (LR) theory, TDDFT provides a treatment of electronically excited states, which is exact up to first order [20]. Excitation energies [48, 51] as well as excited state nuclear forces can be derived in this framework [52–54].

Originally formulated in the Born-Oppenheimer (BO) approximation, TDDFT based AIMD can only be successfully applied to adiabatic processes, where nuclear and electronic motion are decoupled. However, when nuclear and electronic degrees of freedom are strongly coupled (non-adiabatic (NA) processes), several electronic states are necessary to properly describe nuclear motion. Scattering processes and a large number of photochemical reactions belong to the group of NA processes. To overcome the limitation of AIMD to adiabatic processes a complete quantum description of both electrons and nuclei (multicomponent DFT [55]) should be applied. However, this level of accuracy is only suited for the study of very small systems, while computationally more promising methods are based on a semi-classical approach, in which nuclei are treated as classical particles. Semiclassical NA AIMD [28] schemes either use a mean field (Ehrenfest) approximation [56] for the joined electron-nuclear dynamics or make use of trajectory surface hopping (TSH) technique [30]. Advantages and disadvantages of both methods have been discussed extensively in the literature [57]. In particular, the TSH approach is preferable when reactions pass regions of close lying electronic states but end up in a state, which is well described by a single BO potential energy surface (PES).

The TSH technique requires the computation of the NA coupling (NAC) term  $\sigma_{kj} = \dot{\mathbf{R}} \cdot \mathbf{d}_{kj} = \dot{\mathbf{R}} \cdot \langle \Phi_k(\mathbf{r}; \mathbf{R}(t)) | \nabla_{\mathbf{R}} \Phi_j(\mathbf{r}; \mathbf{R}(t)) \rangle$  between two electronic states  $k, j$ .  $\mathbf{r}$  and  $\mathbf{R}$  denote collective electronic and nuclear coordinates, respectively and  $\mathbf{d}_{kj}$  is the NAC vector. Within DFT, difficulties to calculate NACs arise from the fact that the many electron wavefunctions for the adiabatic states are not available. In the first NA DFT-AIMD method based on ROKS [18], NACs are obtained from orbital velocities of the fictitious electron dynamics of the Car-Parrinello scheme. Finite difference schemes based on KS orbitals or single KS Slater determinants (SDs) can be used if the excited state configuration is sufficiently well described by a single SD [50, 58]. Recently, several alternative approaches to compute

NACs within DFT have been proposed [54, 58, 59].

In this letter we combine the *fewest switches* TSH scheme [30] with LR-TDDFT AIMD [52]. The method is applied to the study of the photophysics of protonated formalimine ( $\text{CH}_2\text{NH}_2^+$ ), a minimal model for the chromophore of the visual photoreceptor rhodopsin. Compared to existing DFT TSH methods, namely the ROKS based TSH [18] and the TD-KS TSH method of Craig et al. [50], an important improvement consists in the use of theoretically rigorous excited state PESs and nuclear forces. In the method of Craig et al. [50], total energies are approximated as expectation values of KS-SDs, and excited state wavefunctions are taken simply as singly excited SDs. Therefore the nuclear forces in their approach are only very approximative. In contrast, our approach uses LR-TDDFT to calculate both, excited state energies and forces, increasing considerably the accuracy and reliability of the PESs. The use of LR-TDDFT also allows the inclusion of an in principle unlimited number of excited states, overcoming one of the major limitations of ROKS AIMD, which is capable to treat only the lowest lying excited state. Therefore the method can be applied to the study of systems with a dense manifold of excited states. The NAC term is computed by finite differences using a multi determinantal approximation of the excited state configuration as proposed by Casida [20]. Since excited states are in general not well described by a single SD, we expect a clear improvement of the quality of the computed NACs.

## 4.2 Theory and Implementation

In TD perturbation theory the response of the density to a periodic perturbation with frequency  $\omega$  and amplitude  $\delta V^\pm$  can be expressed by means of the LR orbitals  $\{\phi_j^\pm\}$ , defined by the coupled KS equations [60]. Excitation energies  $\omega_k$  can be found by solving the non-Hermitian eigenvalue problem

$$\sum_{ij}^{N_o} (H^{KS} \delta_{ij} - \epsilon_{ij}) |\phi_j^\pm\rangle + \delta V^{SCF}(\pm\omega) |\phi_i\rangle = \mp \omega_k |\phi_i^\pm\rangle. \quad (4.1)$$

KS orbitals  $\{\phi_i\}$  and Lagrange multipliers  $\epsilon_{ij}$  are determined previously in a ground state calculation.  $N_o$  is the number of occupied orbitals,  $H^{KS}$  is the KS Hamiltonian and  $\delta_{ij}$  is the Kronecker delta.  $\delta V^{SCF}(\pm\omega)$  represents the response of the effective potential to the first order change in the electronic density. It is composed of the Hartree plus the exchange-correlation kernel and is determined self consistently via the LR orbitals. The kernel corrects the KS orbital energy differences to the true excitation

energies. In the Tamm-Dancoff approximation (TDA) [48, 52] the linear response associated with the orbitals  $\{\phi^+\}$  is neglected and Eq. (4.1) can therefore be approximated by a Hermitian eigenvalue problem, with good accuracy [48, 52].

According to the assignment ansatz by Casida [20], the expansion coefficients  $c_{ov}^k$  for the configuration of the excited state  $k$

$$\begin{aligned} |\Phi_k(\mathbf{r}; \mathbf{R})\rangle &\approx \sum_{o=1}^{N_o} \sum_{v=N_o+1}^{N_o+N_v} c_{ov}^k \hat{a}_v^\dagger \hat{a}_o |\Phi_0(\mathbf{r}; \mathbf{R})\rangle \\ &= \sum_{o=1}^{N_o} \sum_{v=N_o+1}^{N_o+N_v} c_{ov}^k |\Phi_o^v(\mathbf{r}; \mathbf{R})\rangle, \end{aligned} \quad (4.2)$$

are obtained by projecting the LR orbitals on a subset of  $N_v$  unoccupied KS orbitals  $\{\phi_v\}$

$$c_{ov}^k = \sqrt{\frac{\epsilon_v - \epsilon_o}{\omega_I}} \langle \phi_o^- | \phi_v \rangle. \quad (4.3)$$

In Eq. (4.2),  $\hat{a}_i$  is the annihilation operator acting on KS orbital  $i$  and indices  $o, v$  refer to occupied and unoccupied space, respectively. The ground state wavefunction  $\Phi_0(\mathbf{r}; \mathbf{R})$  is taken to be the single SD of the occupied KS orbitals,  $|\Phi_0\rangle$ .

Following Tully [30], we derive a *fewest switches* TSH algorithm based on LR-TDDFT quantities. We expand the TD many electron wavefunction  $\Psi(\mathbf{r}, \mathbf{R}, t)$  as a linear combination of the stationary KS-SDs

$$|\Psi(t)\rangle = C_0(t)|\Phi_0\rangle + \sum_{j=1}^{\infty} C_j(t) \sum_{o,v} c_{o,v}^j |\Phi_o^v\rangle. \quad (4.4)$$

Substituting this ansatz into the TD Schrödinger equation, one can derive a first order differential equation for the expansion coefficients  $C_j(t)$

$$i\hbar \dot{C}_k(t) = \sum_{j=0}^{N_{ad}} C_j(t) \{V_{kj} - i\hbar(t)\sigma_{kj}\}, \quad (4.5)$$

where the equality  $\sigma_{kj} = \langle \Phi_k | \frac{\partial \Phi_j}{\partial t} \rangle = \dot{\mathbf{R}} \cdot \mathbf{d}_{kj}$  was used. The expansion is truncated at  $N_{ad}$  adiabatic states. In the adiabatic representation the matrix  $V_{kj} = \langle \Phi_k | H | \Phi_j \rangle$  is diagonal and the  $V_{jj}$  can be



replaced by relative energies  $\tilde{V}_{jj} = V_{jj} - \langle \Phi_0 | H | \Phi_0 \rangle$  [61], here  $H$  refers to the Hamiltonian of the interacting system. The  $\tilde{V}_{jj}$  can be interpreted as the TDDFT excitation energies  $\omega_j$ , which simplifies Eq. (4.5) into

$$i\hbar\dot{\tilde{C}}_k(t) = \tilde{C}_k(t)\omega_k - i\hbar \sum_{j=0}^{N_{ad}} \tilde{C}_j(t)\sigma_{kj}. \quad (4.6)$$

Note that this substitution transforms the  $C_j(t)$  into a new set of coefficients  $\tilde{C}_j(t)$ , which are used to calculate the switching probability [61]. The NAC term  $\sigma_{kj}$  can be directly approximated by the finite differences

$$\sigma_{kj}|_{t+\Delta/2} = \frac{1}{2\Delta} [\langle \Phi_k(\mathbf{r}; \mathbf{R}(t)) | \Phi_j(\mathbf{r}; \mathbf{R}(t + \Delta)) \rangle - \langle \Phi_k(\mathbf{r}; \mathbf{R}(t + \Delta)) | \Phi_j(\mathbf{r}; \mathbf{R}(t)) \rangle]. \quad (4.7)$$

Eq. (4.7) is evaluated using the expansion in Eq. (4.2) for the states  $\Phi_k$  and  $\Phi_j$ , taken at subsequent classical time steps  $t$  and  $t+\Delta$ . The switching probability  $g_{kj}$  between states  $k$  and  $j$  in the interval  $[t, t + \Delta]$  is finally computed from the solutions of Eq. (4.6)

$$g_{k,j}(t, \Delta) \approx -2 \int_t^{t+\Delta} d\tau \frac{\Re[\tilde{C}_j(\tau)\tilde{C}_k^*(\tau)\sigma_{jk}(\tau)]}{\tilde{C}_k(\tau)\tilde{C}_k^*(\tau)}, \quad (4.8)$$

where  $\sigma_{jk}(\tau)$  is obtained by linear interpolation.

The algorithm was implemented into the plane wave code CPMD [62] using the recently implemented LR-TDDFT scheme for the calculation of excited state energies and nuclear forces [52]. At each time step, an electronic spectra calculation provides the eigenvalues  $\omega_k$  of all included adiabatic states and the corresponding many electron wavefunctions according to Eqs. (4.2) and (4.3).  $\sigma_{kj}$  is calculated from Eq. (4.7) using the overlap matrix between the KS orbitals at time  $t$  and  $t + \Delta$   $\langle \phi_i(\mathbf{r}; \mathbf{R}(t)) | \phi_j(\mathbf{r}; \mathbf{R}(t + \Delta)) \rangle$ . The  $\tilde{C}_k(t)$  are propagated by integration of Eq. (4.6) using a standard Runge-Kutta 4th order algorithm, and  $g_{kj}$  is evaluated at each time step via Eq. (4.8). In a Monte-Carlo step a random number from  $[0; 1]$  is compared to  $g_{k,j}$ . If the random number is smaller than  $g_{k,j}$  the system switches PES and the nuclear forces are taken from the new state  $j$ , while the  $\tilde{C}_j$  are continuously propagated. In order to conserve total energy, the ionic velocities are rescaled isotropically if a switch is accepted. For the case in which the trajectory hits an intersection point and the NAC is undefined, a

switch between adiabatic surfaces is forced following the electronic character of the current state and interchanging the labels of the  $\tilde{C}_j$  of the two involved states. This scheme does not include spin-orbit coupling and therefore it is not able to describe intersystem crossings.

### 4.3 Results

As an application of the described method, we studied the photorelaxation process of the protonated Schiff base  $\text{CH}_2\text{NH}_2^+$ , the smallest model compound of rhodopsin chromophore. The mechanism of the light induced cis-trans isomerization in retinal has been subject of many experimental and theoretical studies [63]. In  $\text{CH}_2\text{NH}_2^+$ , the second excited singlet state ( $S_2: \pi - \pi^*$ ) exhibits an oscillator strength orders of magnitude larger than the one of the first excited singlet state ( $S_1: \sigma - \pi^*$ ). Photoexcitation promotes the system mainly into  $S_2$  and the following relaxation involves at least 3 states,  $S_2$ ,  $S_1$  and  $S_0$ . The aim of our study is to test the implemented scheme, in particular its capability to include several excited states, and to identify the main reaction pathways. A complete statistical description of all possible reaction branches on the other hand is beyond the scope of this work. The quality of our results is checked against reference data obtained from high level wavefunction based methods [64, 65].

All calculations employ the PBE exchange-correlation functional [66]. Further details are given in reference <sup>1</sup> If not specified differently, dynamics were performed in the microcanonical ensemble (NVE). In order to investigate the effect of heat dissipation, we also carried out some simulations in the NVT ensemble using a Nosé-Hoover thermostat. An ensemble of 20 starting geometries, taken from a Boltzmann distribution at 300 K, was excited into  $S_2$ . The ionic degrees of freedom were propagated with a time step of 10 a.u. (0.241 fs) whereas for the propagation of the  $\tilde{C}_j$  a time step of  $10^{-5}$  a.u. was used. Starting in the Franck-Condon region, the system loses potential energy, resulting in a fast increase of temperature up to 3000 K. In most trajectories, relaxation to the ground state occurs after 30–100 fs, but also trajectories with excited state lifetimes longer than 200 fs were found (Fig. 4.1). For a typical trajectory the time evolution of the energies of the relevant electronic states and their state populations are shown in Fig. 4.2. The  $S_2$  lifetimes typically range from 10 up to 50 fs, whereas  $S_1$  lifetimes are

---

<sup>1</sup>Calculations employ norm conserving pseudopotentials [67] and a cutoff of 70 Ry for the plane wave basis set. The simulations were carried out using an isolated cubic box with an edge of 8 Å. In order to converge the description of the relevant excited states, a total of 8 excited states were included in the calculations. In addition to the 6 occupied states 8 virtual KS orbitals were computed, leading to a total of 48 excited SDs.

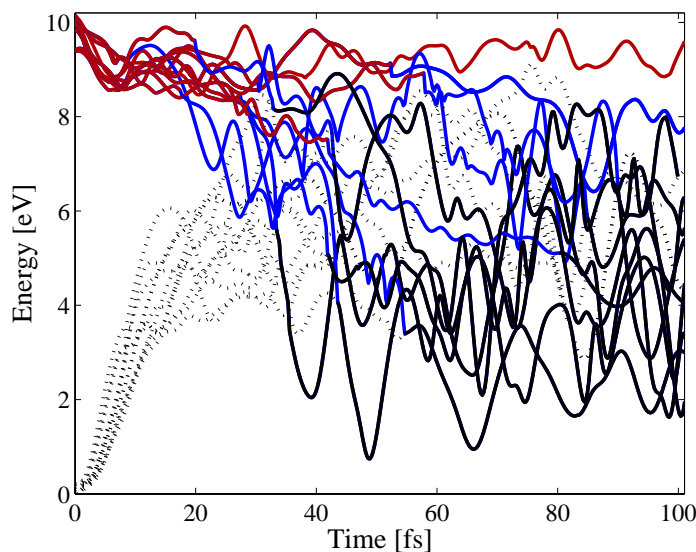


Figure 4.1: Potential energy surfaces of a swarm of 10 trajectories. The state where nuclear forces were taken from (—) and  $S_0$  (- -) are shown. Red and blue colors stand for  $S_2$  and  $S_1$  respectively, whereas black indicates that the system has relaxed into  $S_0$ . Most trajectories relax to  $S_0$  within 100 fs.

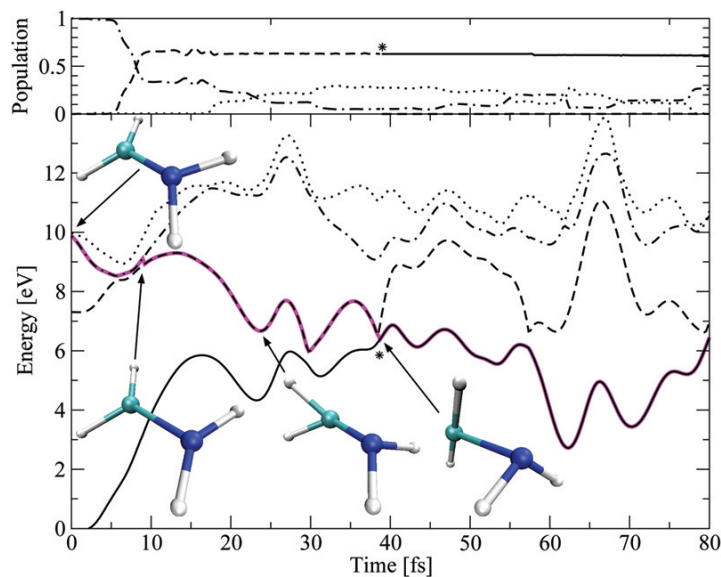


Figure 4.2: Evolution of the state populations (upper panel) and of the potential energy surfaces (lower panel)  $S_0$  (—),  $S_1$  (- -),  $S_2$  (- ·) and  $S_3$  (· ·) together with some characteristic molecular structures for a typical trajectory. The state that drives the dynamics is shown in red. The main structural change in  $S_2$  during the first 10 fs is a CN bond elongation (C cyan, N blue). After 6 fs the system enters the avoided crossing region between  $S_2$  and  $S_1$ . Population is transferred until a switch to  $S_1$  is accepted after 10 fs. In  $S_1$ , the geometry at N changes from planar to pyramidal. After 40 fs the system reaches the intersection between  $S_1$  and  $S_0$  (\*) and relaxes to  $S_0$ .

found to be in the range 10–100 fs. The ratio of the lifetimes qualitatively agree with the ones obtained using a state averaged multiconfiguration self consistent field (SA-MCSCF) TSH approach [65]. For comparison, we also computed the NAC terms for some geometries of the trajectory using the complete active space self consistent field (CASSCF) method [68]<sup>2</sup> The relative magnitudes of the CASSCF NACs are consistent with the NACs obtained by LR-TDDFT. Typical structural changes following excitation are the CN bond elongation in the first 10 fs and subsequent pyramidalization of the nitrogen center (see molecular structures in Fig. 4.2). These geometrical changes are identical to the ones reported in the SA-MCSCF study [65].

Different forces in the excited states as well as the excess kinetic energy, accumulated during the relaxation process, trigger different reaction channels. If the system is cooled down to 300 K upon  $S_1 \rightarrow S_0$  transition, we find that half of the trajectories isomerize around the CN bond. Without thermostat, the kinetic energy is sufficiently high to allow multiple rotations around the CN bond. Another possible reaction channel is intramolecular proton transfer, leading to  $\text{CH}_3\text{NH}^+$  which remains stable in  $S_1$  for several tens of fs. After thermalization at 300 K in  $S_0$ , the proton is transferred back, leading eventually to an isomerized product. Some trajectories also exhibit the experimentally observed  $\text{H}_2$  abstraction [69].

## 4.4 Conclusion

In summary, we have developed and implemented a new TSH scheme based on LR-TDDFT, which makes use of a multideterminantal approximation of the excited states for the computation of the NACs. The presented method benefits from a formally exact description of excited state energies and nuclear forces at the LR-TDDFT level. The relatively low computational costs allows the study of relatively large systems and multiple trajectories. Furthermore, the number of excited states included in the NA dynamics is in principle unlimited. We have applied this method to the photorelaxation of the retinal model compound  $\text{CH}_2\text{NH}_2^+$ . The relative magnitudes of the NAC terms compare well to NACs obtained by CASSCF. Observed lifetimes and structural relaxation are also in remarkably good agreement with wavefunction based methods.

---

<sup>2</sup>We computed the full non-adiabatic coupling vectors  $d_{k,j}$  between the  $2^{nd}$  and  $1^{st}$  excited states at a CASSCF level of theory. A (6,5)-active space and the cc-pVTZ basis set were used. The coupling terms were calculated using the ionic velocities from the CPMD trajectory according to  $\sigma_{k,j} = \dot{R} \cdot d_{k,j}$ .

We thank Ari P. Seitsonen and Mauricio D. Coutinho-Neto for discussions and the Swiss National Science Foundation for financial support.



## Chapter 5

# LR-TDDFT Calculation of Non-Adiabatic Coupling Vectors

### Abstract

Non-adiabatic coupling (NAC) transition matrix elements have recently been computed by Time-Dependent Density Functional Theory (TDDFT) within surface hopping dynamics [Phys. Rev. Lett., 98, 023001, 2007] using Casida's assignment ansatz for the excited states. Here, we use the same principle combined with a finite difference scheme to compute the full derivative NAC vectors. We evaluate their accuracy by means of a comparison to wavefunction based methods. The scheme is applied to compute vectors coupling  $S_1/S_0$  and  $S_2/S_1$  states for a few organic model compounds. Comparison with vectors computed by the Complete Active Space Self-Consistent Field (CASSCF), confirms a good qualitative agreement regarding the directions of the vectors. However in general, TDDFT underestimates their magnitudes when compared with CASSCF, but this is not related to the found underestimation of the energy gap by TDDFT. Therefore it is suggested that the underestimation of the magnitudes of the NAC vectors is due to the differences in the density distributions resulting from CASSCF and TDDFT. In addition, within the finite difference scheme the influence of the size of the nuclear displacement on the accuracy of the NAC vectors is evaluated.

## 5.1 Introduction

Because of the large difference between nuclear and electronic masses, most quantum chemical methods assume a separation between the motion of electrons and nuclei (Born-Oppenheimer approximation) [22]. This assumption leads to a considerable simplification to solve the electronic structure problem; the time-independent Schrödinger equation is solved using an electronic Hamiltonian parametrically dependent on the positions of the nuclei. Solution of this problem yields the adiabatic states  $\Phi_k$ , which often provide a useful picture to explain, e.g., reaction dynamics. Nevertheless many chemical problems do not fall in the regime where nuclei and electrons can be considered to be decoupled. For those cases, the non-adiabatic coupling (NAC) that accounts for the coupling between the motion of nuclei and electrons is non-negligible. Most photoreactions pass through regions of the potential energy surface (PES), such as conical intersections (CXs) or avoided crossings, in which non-adiabatic effects are sizeable or crucial. Semiclassical methods that have been developed to describe these type of processes make use of the *derivative* NAC vector

$$\mathbf{d}_{kj} = \langle \Phi_k(\mathbf{r}; \mathbf{R}(t)) | \nabla_{\mathbf{R}} \Phi_j(\mathbf{r}; \mathbf{R}(t)) \rangle \quad (5.1)$$

to correct for non-adiabatic effects. For instance in surface hopping (SH) dynamics [30], NAC matrix elements  $\sigma_{kj} = \dot{\mathbf{R}} \cdot \mathbf{d}_{kj}$  are used to evaluate transition probabilities between adiabatic states, and ionic velocities are scaled along the direction of the NAC vector after surface hops in order to conserve the total energy. NAC vectors are also used to locate special points on the potential energy surface (PES), such as CXs [70].

Approximate excited state DFT methods, based on the Slater transition state density [71, 72] and restricted open-shell Kohn-Sham theory [17], have been used to compute NAC vectors [58, 73]. In the last decade, time-dependent density functional theory (TDDFT) [19] has been used increasingly to describe excited states. The extension of TDDFT to non-adiabatic processes creates the need to compute NACs on this level of theory. To our knowledge, Chernyak and Mukamel were the first to use TDDFT to compute NACs, which was based on a density matrix formulation of TDDFT [74]. Later, Baer proposed a method to compute NAC vectors by real time propagation [59]. A scheme within linear response (LR)-TDDFT via implicit differentiation has been proposed by Doltsinis and Kosov [54]. Within the



TDDFT-SH dynamics we have introduced a method to compute NAC matrix elements [21], based on Casida's ansatz for the assignment of the excited states [20]. A more direct but similar procedure using LR-TDDFT has been published at the same time by Sugino [75] and co-workers.

In the present study, we use again the Casida ansatz to compute the full NAC vectors by TDDFT. This is done via a finite difference (FD) scheme similar to the one proposed by Billeter [58]. The aim of this paper is to assess the quality of NAC vectors obtained from TDDFT and to compare them to the results of state-average complete active space self consistent field method (SA-CASSCF) calculations. We have also evaluated the influence of the displacement parameter  $\epsilon$  in the FD calculations, as it provides information for the choice of a computationally efficient the time step in TDDFT-SH dynamics without compromising the accuracy of the NAC elements. NAC vectors cannot be measured experimentally and therefore the only possible validation is a comparison to other theoretical methods, for which we have chosen SA-CASSCF. However, NAC vectors computed with CASSCF are not necessarily more accurate than TDDFT, because CASSCF depends strongly on the chosen active space and moreover it is only able to include static electron correlation, neglecting dynamic correlation effects. The reason for this choice is that SA-CASSCF is widely used as underlying electronic structure method in SH dynamics [14]. In addition, to date, SA-CASSCF seems to be the only method that provides NACs in a standard computation, as implemented in a few electronic structure codes [14, 68, 76].

## 5.2 Method

Our scheme to compute NAC vectors is based on the LR-TDDFT formulation of Hutter [52], applied within the Tamm-Dancoff approximation [48] (TDA). The TDA has been shown to give similar results as full LR-TDDFT for equilibrium geometries of closed shell systems [48, 52].

In this formulation, the response of the ground state electronic density to a periodic perturbation with frequency  $\omega$  and amplitude  $\delta V$  is expressed by means of the LR orbitals  $\{\phi_j^1\}$  [60]. The excitation energies  $\omega_k$  are computed solving the Hermitian eigenvalue equations of TDDFT in the TDA,

$$\sum_{ij}^{N_o} (\hat{H}_{KS} \delta_{ij} - \epsilon_{ij}) |\phi_j^1\rangle + \delta V_{SCF}(\omega) |\phi_i\rangle = \omega_k |\phi_i^1\rangle. \quad (5.2)$$

Kohn-Sham (KS) orbitals  $\{\phi_i\}$  and Lagrange multipliers  $\epsilon_{ij}$  are determined previously in a ground

state calculation.  $N_o$  is the number of occupied orbitals,  $\hat{H}_{KS}$  refers to the KS Hamiltonian and  $\delta_{ij}$  to the Kronecker delta.  $\delta V_{SCF}(\omega)$  represents the response of the effective potential to the first order change in the electronic density induced by a perturbation proportional to  $e^{i\omega t}$ . The excited state wavefunction can be described using the Casida ansatz in which the LR orbitals  $\{\phi^1\}$  are projected on a subset of  $N_v$  unoccupied KS orbitals  $\{\phi_v\}$ . This procedure yields the expansion coefficients  $c^k$

$$c_{ov}^k = \langle \phi_o^- | \phi_v \rangle \quad (5.3)$$

for the expansion of the excited state in terms of singly excited KS determinants [77],

$$|\Phi_k(\mathbf{r}; \mathbf{R})\rangle \approx \sum_{o=1}^{N_o} \sum_{v=N_o+1}^{N_o+N_v} c_{ov}^k |\Phi_o^v(\mathbf{r}; \mathbf{R})\rangle, \quad (5.4)$$

where  $|\Phi_o^v(\mathbf{r}; \mathbf{R})\rangle = \hat{a}_v^\dagger \hat{a}_o |\Phi_0(\mathbf{r}; \mathbf{R})\rangle$  is a singly excited KS Slater determinant. Using expression (5.4) and approximating the ground state wavefunction by a single closed shell KS Slater determinant we have the required approximations for the adiabatic states to compute the NAC vector (5.1). To apply the FD scheme proposed in Ref. [58], we need only to solve (5.2), (5.3), and (5.4) for different sets of nuclear coordinates, generated by Cartesian displacements  $\epsilon_\alpha$ ,  $\alpha = x, y, z$ , around the reference geometry:

$$\begin{aligned} \langle \Phi_k | \frac{\partial}{\partial R_{I,\alpha}} | \Phi_j \rangle &\approx d_{kj}^{\epsilon, I, \alpha} = \frac{\langle \Phi_k | \Phi_j^{\epsilon, I, \alpha} \rangle s_+ - \langle \Phi_k | \Phi_j^{-\epsilon, I, \alpha} \rangle s_-}{2\epsilon}, \\ s_\pm &= \begin{cases} 1 & \text{if } \langle \Phi_k | \Phi_j^{\pm\epsilon, I, \alpha} \rangle > 0 \\ -1 & \text{if } \langle \Phi_k | \Phi_j^{\pm\epsilon, I, \alpha} \rangle < 0 \end{cases} \end{aligned} \quad (5.5)$$

Here  $k, j$  label the two electronic states of interest and the index  $I$  runs over all atoms. Using the derivative operator in (5.5) defined in Cartesian coordinates does not ensure the NAC vector to be translationally invariant. To achieve translational invariance we correct  $\mathbf{d}_{kj}$  using

$$d_{kj}^{I,\alpha} = \langle \Phi_k | \frac{\partial}{\partial R_{I,\alpha}} | \Phi_j \rangle - \frac{1}{N_{atoms}} \sum_{I',\alpha} \langle \Phi_k | \frac{\partial}{\partial R_{I',\alpha}} | \Phi_j \rangle \quad (5.6)$$

as proposed in Ref. [73].

### 5.3 Computational Details

Molecular geometries were optimized using DFT/PBE as implemented in the TURBOMOLE package [78] and the TZVP basis set [79]. Convergence criteria for the nuclear gradients were set to  $10^{-3}$  a.u. Optimizations were done imposing the highest possible symmetry point group of the given molecule, that is,  $C_{2v}$  for  $\text{H}_2\text{O}$  and  $\text{CH}_2\text{NH}_2^+$ , and  $C_s$  for thymine. All TDDFT calculations also employ the PBE functional [66] and make use of the TDA [48,52]. NAC vectors were computed for the optimized ground state equilibrium geometries.

The TDDFT-FD scheme described above (5.5) was implemented in the plane wave *ab initio* package CPMD [62] based on the TDDFT implementation of Hutter [52]. The criteria for the convergence of the wavefunctions was set to  $10^{-6}$  a.u. In expansion (5.4), four virtual orbitals were included in the case of water, whereas for  $\text{CH}_2\text{NH}_2^+$  and thymine, eight orbitals were included. A plane wave cutoff 70 Ry was sufficient to converge excitation energies for all test molecules. We use pseudopotentials of the Troullier-Martins type [67] to integrate out the effects of core electrons. Molecules are placed in the center of orthorhombic supercells while the Poisson equation is solved for isolated systems. The box dimensions for both,  $\text{H}_2\text{O}$  and  $\text{CH}_2\text{NH}_2^+$  measure  $12 \times 12 \times 10 \text{ \AA}^3$ . For thymine a box of dimensions  $14 \times 14 \times 10 \text{ \AA}^3$  is used. Nuclear displacements  $\epsilon$  are varied between to 0.005 and 0.500 Bohr (1 Bohr  $\approx 0.5292 \text{ \AA}$ ).

SA-CASSCF calculations were done with the programm GAUSSIAN03 [68]. To obtain the NAC vectors we use the routine for the optimization of conical intersection geometries. All CASSCF calculations employ the 6-31+G\*\* [80, 81] basis set. We use a 6-electron, 6-orbital active space [CAS(6,6)] for  $\text{H}_2\text{O}$  and  $\text{CH}_2\text{NH}_2^+$ . For thymine a 8-electron, 6-orbital active [CAS(8,6)] is used. Equal weights for all states were applied for the state averaging procedure.

The comparison of NAC vectors computed by different methods is based on the following quantities. The length  $L$  of the vector is defined as

$$L = \sqrt{\sum_I \sum_{\alpha} d_{I,\alpha}^2} \quad (5.7)$$

Applying the Hellman-Feynman theorem to (5.1), yields the well-known expression for the NAC vector that is inversely proportional to the energy gap  $\Delta E = E_j(\mathbf{R}) - E_k(\mathbf{R})$  between the two adiabatic

states

$$\mathbf{d}_{kj} = \frac{\langle \Phi_k | \nabla_{\mathbf{R}} H_{el} | \Phi_j \rangle}{E_j(\mathbf{R}) - E_k(\mathbf{R})} \quad (5.8)$$

Equation (5.8) indicates that the lengths of the NAC vectors strongly depend on the excitation energies predicted by the particular electronic structure method. To decouple the lengths of the vectors from the energy gap and achieve a somewhat more objective evaluation criteria, we also report the *scaled* length  $L'$  of the vectors defined as

$$L' = \Delta E \sqrt{\sum_I \sum_{\alpha} d_{I,\alpha}^2} \quad (5.9)$$

The root mean square deviation (RMS) between two vectors  $d$  and  $d'$  is evaluated as

$$RMS = \frac{1}{3N_{atoms}} \sqrt{\sum_I \sum_{\alpha} (d_{I,\alpha} - d'_{I,\alpha})^2}. \quad (5.10)$$

In the following we will only report the RMS between the energy scaled vectors. To measure the deviation between the directions of two vectors we define the correlation  $C$

$$C = \sum_I \frac{\mathbf{d}'_I \cdot \mathbf{d}_I}{|\mathbf{d}'_I| \cdot |\mathbf{d}_I|} \quad (5.11)$$

## 5.4 Results

For all of the TDDFT NAC vectors reported here, we refer to vectors that have been corrected for translational invariance according to (5.6). For the water molecule, CASSCF is able to reproduce accurately the experimental first excitation energy of 7.4 eV, while TDDFT underestimates it by about 0.8 eV. Regarding the directions of the  $S_1$ - $S_0$  NAC vectors (Fig. 5.1), both methods agree qualitatively, which is also reflected by the correlation of 1.00 for most values of  $\epsilon$  (Table 5.1). However, CASSCF predicts the lengths of the NAC vector to be about 10 times larger than TDDFT, although the  $S_1$ - $S_0$  gap is considerably larger in CASSCF than in TDDFT. Because of the inverse relationship (5.8), one would expect the contrary behavior, so the divergence of the magnitudes becomes even larger if one considers the scaled vectors. Regarding the effect of the finite nuclear displacement on the magnitude of the NAC, we see that the length of the vectors diminishes at displacements of 0.1 Bohr and larger, whereas the correlation is basically not affected by changing  $\epsilon$ .

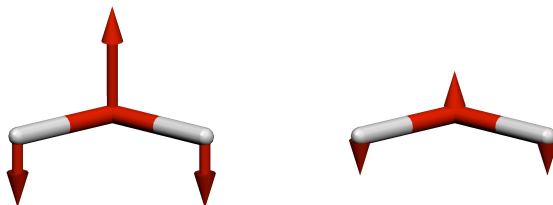


Figure 5.1:  $S_1$ - $S_0$  NAC vectors of  $\text{H}_2\text{O}$  computed by CASSCF (left) and TDDFT (right). The lengths of the NAC vectors as shown is proportional to their actual magnitudes.

Method	$\Delta E$	$\epsilon$	$L$	$L'$	RMS	$C$
TDDFT-FD	6.261	0.005	0.0325	0.0075	0.0251	0.9998
		0.010	0.0325	0.0075	0.0251	1.0000
		0.020	0.0325	0.0075	0.0251	1.0000
		0.100	0.0316	0.0073	0.0252	1.0000
		0.200	0.0302	0.0069	0.0253	1.0000
CAS(6,6)	7.437	-	0.3031	0.0844	(ref)	(ref)
experiment <sup>a</sup>	7.4	-	-	-	-	-

Table 5.1:  $S_1$ - $S_0$  NAC vectors of  $\text{H}_2\text{O}$  computed by TDDFT and CASSCF. <sup>a</sup> Experimental value was taken from Ref. [82].  $\epsilon$  is given in Bohr;  $L$ ,  $L'$ , and RMS are given in Bohr<sup>-1</sup>;  $\Delta E$  is given in eV.

For  $\text{CH}_2\text{NH}_2^+$  we computed not only the coupling between  $S_1$  and the ground state, but also the NAC vector between the two excited states  $S_2$  and  $S_1$ . CASSCF overestimates the first singlet excitation energy (Table 5.2) by about 0.7 eV with respect to the high-level ab initio value, while TDDFT again underestimates the energy by about 0.8 eV. In contrast, the energy gap between  $S_2$  and  $S_1$  is overestimated by more than 1.8 eV by TDDFT, whereas it is better described by CASSCF, which underestimates the gap by only 0.2 eV. Comparing the qualitative appearance of the NAC vectors (Fig. 5.2), it is evident that the two methods CASSCF and TDDFT agree well in the qualitative description of the nuclear motion associated with the transitions between both  $S_2$ - $S_1$  and  $S_1$ - $S_0$ . In both cases, the associated mode can be characterized as a twist around the N-C bond. Also with respect to the relative magnitudes both methods agree, and predict the  $S_2$ - $S_1$  coupling to be much larger than the  $S_1$ - $S_0$  coupling. Regarding the absolute lengths (Table 5.2), TDDFT predicts about 10% smaller couplings than CASSCF in the case of  $S_1$ - $S_0$ . In the case of  $S_2$ - $S_1$ , TDDFT underestimates the length by 30%. If we consider the scaled vectors, the underestimation rises up to 30% for the  $S_1$ - $S_0$  coupling and turns into an overestimation of about 25% in the case of  $S_2$ - $S_1$ , due to the much larger  $S_2$ - $S_1$  gap in TDDFT.

The displacement parameter exhibits the same trend as in the case of water, and displacements larger

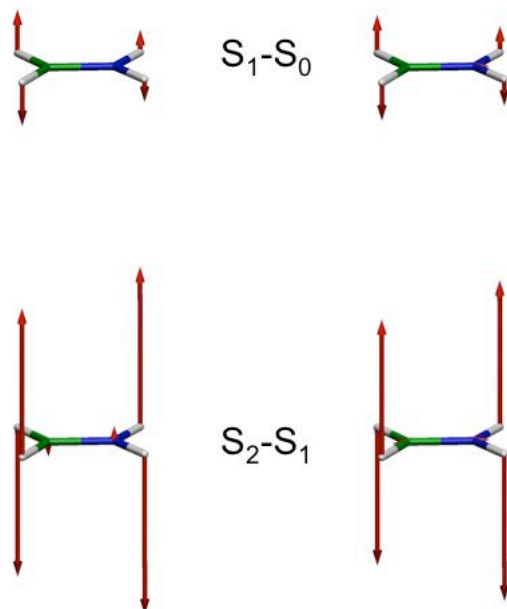


Figure 5.2: NAC vectors of  $\text{CH}_2\text{NH}_2^+$  computed by CASSCF (left) and TDDFT (right).

than 0.1 Bohr lead to a drop in the lengths of the vectors. For the direction of the  $S_1$ - $S_0$  vectors we see a good correlation between CASSCF and TDDFT, whereas for the  $S_2$ - $S_1$  coupling a special behavior is encountered: for some values of  $\epsilon$ , the correlation drops to  $\approx 0.7$ . This is due to the very small vector components at the carbon and nitrogen atoms, which lead to a C-N stretching (only marginally visible in Fig. 5.2). By excluding the vector components of carbon and nitrogen, a correlation of 1.00 between CASSCF and TDDFT can be found for all values of  $\epsilon$ . These vector components are absent in the CASSCF vectors for the equilibrium geometry investigated here, and the TDDFT vectors computed at smallest displacement of 0.005 Bohr do not exhibit these components either. However, it has been shown that also within CASSCF, this stretching mode occurs by approaching the  $S_2$ - $S_1$  conical intersection [65]. This divergence shows how sensitive the magnitude of the NAC vectors are to the shape of the PES.

For thymine, TDDFT underestimates the  $S_1$  excitation energy by more than 1 eV, whereas CASSCF agrees within 0.4 eV of the experimental value (Table 5.3). The underestimation of TDDFT could be due to the partial charge transfer character of the transition [83], indicated by the different spatial distribution of donor and acceptor orbitals (Fig. 5.4). This reasoning is confirmed by the fact that we find a higher

States	Method	$\Delta E$	$\epsilon$	$L$	$L'$	RMS	$C$
$S_1-S_0$	TDDFT-FD	7.505	0.005	0.2945	0.0812	0.0086	1.0000
			0.010	0.2945	0.0812	0.0086	1.0000
			0.020	0.2942	0.0811	0.0086	1.0000
			0.100	0.2916	0.0804	0.0097	0.9976
			0.200	0.2743	0.0757	0.0106	0.9970
	CAS(6,6)	9.095	-	0.3367	0.1125	(ref)	(ref)
	MR-CISD+Q <sup>b</sup>	8.35	-	-	-	-	-
$S_2-S_1$	TDDFT-FD	2.556	0.005	2.0669	0.1941	0.0334	0.9999 ( 1.0000 )
			0.010	2.0656	0.1940	0.0334	0.6791 ( 1.0000 )
			0.020	2.0602	0.1935	0.0332	0.7071 ( 1.0000 )
			0.100	1.9053	0.1790	0.0298	0.7771 ( 1.0000 )
			0.200	1.5747	0.1479	0.0225	0.8333 ( 1.0000 )
	CAS(6,6)	0.632	-	2.2591	0.0525	(ref)	(ref)
	MR-CISD+Q <sup>b</sup>	0.82	-	-	-	-	-

Table 5.2: NAC vectors of  $\text{CH}_2\text{NH}_2^+$  computed by TDDFT and CASSCF. <sup>b</sup> The multireference configuration interaction singles and doubles, corrected for size extensivity (MR-CISD+Q) result taken from Ref. [65]. The values for  $C$  given in parenthesis refer to the correlation where vectors on carbon and nitrogen were excluded in the evaluation. For units see caption of Fig. 5.1.

excitation energy of 4.4 eV if the hybrid PBE0 functional is used. However, for the sake of comparison we will only report NACs computed by PBE here.

The  $S_1-S_0$  NAC vectors of CASSCF and TDDFT are shown in Fig. 5.3. As in the previous two cases, CASSCF predicts overall stronger coupling between  $S_1$  and  $S_0$  (Table 5.3), regardless of the energy gap. The overestimation amounts to approximately 15 and 40% for the unscaled and scaled lengths, respectively. At the positions of most atoms the directions of the NAC vectors correlate well but the relative lengths vary between the two methods. For atom N6 (Fig. 5.3), we find the TDDFT NAC vectors pointing in the opposite direction than the CASSCF vector. This divergence as well as the differences in the relative magnitudes are indicated by the different orbitals that constitute the major component of the  $S_0-S_1$  electronic transition according to the two methods (Fig. 5.4). Large differences in the correlations are found for the components located on the methyl group (C3, H12-14) and H10, leading to a very weak correlation between CASSCF and TDDFT NAC vectors of 30-60%. The lengths of these vectors are at the limit of the accuracy of the method and their directions deviate largely within the TDDFT computations with different values for  $\epsilon$ . To explain the small magnitudes of the vector components on these atoms, we consider the orbitals that constitute the dominant transition as shown in Fig. 5.4. According to CASSCF and TDDFT the amplitudes of the orbitals on these atoms are both very

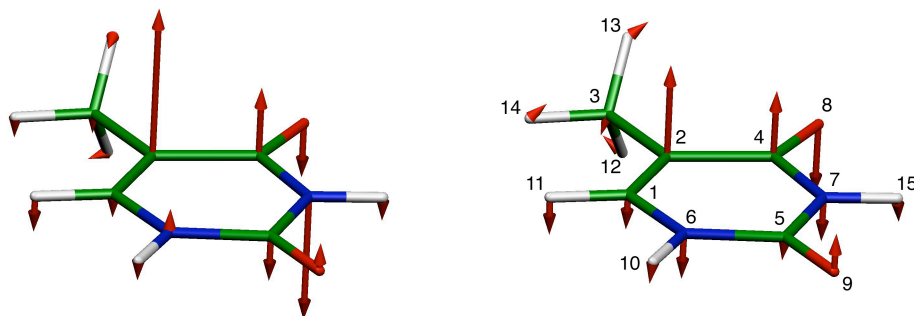


Figure 5.3:  $S_1$ - $S_0$  NAC vectors of thymine computed by CASSCF (left) and TDDFT (right). The lengths of the NAC vectors as shown is proportional to their actual magnitudes.

small, leading to a small overlap and thus to small components of the NAC vectors. The exclusion of the vectors on atoms C3, H12-14, and H10, due to their very small magnitudes, leads to an increase of the correlation of up to 70%, and the results are also less sensitive to the choice of  $\epsilon$ . Due to the opposite direction of the vector located on atom N6 a better agreement cannot be obtained. As in the previous cases, the absolute lengths of the TDDFT-FD vectors are no longer reliable at displacements larger than 0.1 Bohr.

Method	$\Delta E$	$\epsilon$	$L$	$L'$	RMS	$C$
TDDFT FD	3.463	0.005	0.2563	0.0331	0.0040	0.4206 (0.5289)
		0.010	0.2384	0.0308	0.0035	0.5103 (0.5300)
		0.020	0.2287	0.0296	0.0032	0.6480 (0.6881)
		0.100	0.1671	0.0216	0.0022	0.5796 (0.7256)
		0.200	0.1163	0.0150	0.0016	0.3110 (0.7262)
		0.500	0.0549	0.0071	0.0014	0.0483 (0.3614)
CAS(8,6)	5.083	-	0.2700	0.0504	(ref)	(ref)
experiment <sup>c</sup>	4.5-4.7	-	-	-	-	-

Table 5.3:  $S_1$ - $S_0$  NAC vectors of thymine computed by TDDFT and CASSCF. <sup>c</sup> Experimental value taken from Ref. [84]. The values for  $C$  given in parenthesis were evaluated excluding C3, H12-13, and H10, according to the numbering defined in Fig. 5.3. For units see caption of Fig. 5.1.

## 5.5 Conclusions

In the case of the three model systems investigated here, the excitation energies computed with CASSCF are in better agreement with experiment or with high-level *ab initio* calculations than when calculated using TDDFT/TDA using the PBE functional. With the exception of the  $S_2$  state of  $\text{CH}_2\text{NH}_2^+$ , TDDFT



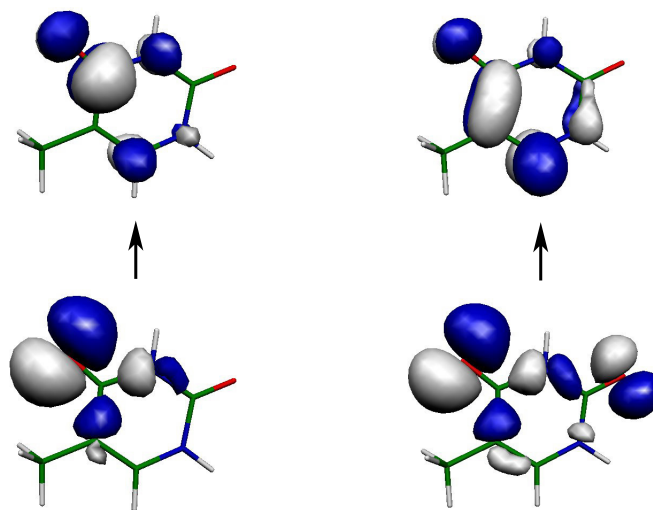


Figure 5.4: Comparison between CASSCF and KS orbitals of thymine. Left: Major single particle transition contributing to  $S_1$  according to CASSCF. Right: Major single particle transition contributing to  $S_1$  according to TDDFT. The lengths of the NAC vectors as shown is proportional to their actual magnitudes.

systematically underestimates the excitation energies by  $\approx 0.8$ - $1.8$  eV. In contrast, CASSCF gives quite accurate excitation energies, exhibiting deviations from the given reference values of less than 0.8 eV. The performance of TDDFT could probably be improved using other approximations for the exchange-correlation functional. Hybrid or asymptotic corrected functionals are both likely to improve the quality of the TDDFT excitations energies.

Concerning the calculation of the NAC vectors, for the small molecules  $H_2O$  and  $CH_2NH_2^+$  we find a very good correlation for the direction of the vectors computed with CASSCF and TDDFT. In the case of thymine, the correlation is worse, but the descriptions of the collective molecular displacement associated to the non-adiabatic transitions are nevertheless in good agreement with one another.

The agreement between the two methods is worse for the lengths of the NAC vectors. In all cases, CASSCF predicts stronger NACs between  $S_1$ - $S_0$  surfaces than TDDFT. On average the difference of the NAC vector magnitudes amounts to 10-40% (see Tables 5.2 and 5.3), but in the case of water, it becomes larger. For this molecule we measured a ratio of 10:1 between the CASSCF and TDDFT NAC vectors.

Surprisingly, the discrepancies in the magnitudes of the vectors cannot be straightforwardly associated with differences in the energy gaps between the surfaces of interest. On the contrary, the energy

gap is always found to be larger in CASSCF than in TDDFT, in the case of the  $S_1$ - $S_0$  couplings. This leads to even larger differences between the rescaled NAC vectors (5.8). In only the case of the  $S_2$ - $S_1$  coupling can the large magnitude of the CASSCF vector be explained by the small CASSCF energy gap. We conclude therefore that the difference in the length of the NAC vectors measured with TDDFT and CASSCF is more likely related to a difference of the orbital overlaps than to a difference in energy gaps.

Regarding densities, a larger delocalization of the KS orbitals compared to stronger localization of the orbitals in CASSCF might be the reason for the differences in the relative lengths of the vectors and is indicated by the spatial extent of the thymine orbitals shown in Fig. 5.4. However, the shape of the PES might also influence the couplings for the present examples as we have seen in the case of the  $S_2$ - $S_1$  coupling of  $\text{CH}_2\text{NH}_2^+$ , where at the equilibrium geometry the N-C stretching mode could not be observed on the CASSCF level whereas it has been found for other geometries which are probably closer to the  $S_2$ - $S_1$  conical intersection [65].

Regarding the sensitivity of the NAC vectors to the displacement parameter, we find that for most systems the lengths of the NAC vectors decrease for values of  $\epsilon$  larger than 0.1 Bohr. On average, the best correlation between CASSCF and TDDFT results is found for values between 0.02 – 0.1 Bohr. In the case of the on-the-fly calculation of the NAC vectors during non-adiabatic TDDFT-SH dynamics [21] we therefore suggest to take classical time steps in such a way that atomic displacements ( $2\epsilon$ ) are within 0.04 and 0.2 Bohr.

The influence of different exchange-correlation functionals on the TDDFT NACs remains to be investigated and a comparison with NACs obtained from *ab initio* methods that includes dynamic correlation is also desirable.

The finite difference scheme has been found to be not optimal, because the displacements are difficult to control. An improvement could be introduced in TDDFT-SH dynamics if NACs are computed by analytic gradient methods. However, as a first approximation a qualitatively correct description of the coupling between nuclear and electronic motion can also be achieved within the present approach.

We gratefully thank Salomon Billeter for explanations and discussions.

## Chapter 6

# Mixed Time-Dependent Density-Functional Theory/Classical Trajectory Surface Hopping Study of Oxirane Photochemistry

### Abstract

We present a mixed time-dependent density-functional theory (TDDFT)/classical trajectory surface hopping (SH) photochemical dynamics study of oxirane ring opening. Previous preparatory work limited to the symmetric CC ring-opening pathways of oxirane concluded that the Tamm-Dancoff approximation (TDA) is important for improving the performance of TDDFT away from the equilibrium geometry. This observation is supported by the present TDDFT TDA/SH calculations which successfully confirm the main experimentally-derived Gomer-Noyes mechanism for the photochemical CO ring opening of oxirane and, in addition, provide important state-specific information not easily accessible from experiments. In particular, we find that, while one of the lowest two excited states is photochemically relatively inert, excitation into the other excited state leads predominantly to rapid ring opening, *cyclic*-C<sub>2</sub>H<sub>4</sub>O → •CH<sub>2</sub>CH<sub>2</sub>O•. This is followed by hopping to the electronic ground state where hot (4000 K) dynamics leads to further reactions, namely •CH<sub>2</sub>CH<sub>2</sub>O• → CH<sub>3</sub>CHO → •CH<sub>3</sub> + •CHO and CH<sub>4</sub> + CO. We note

that, in the dynamics, we are not limited to following minimum energy pathways and several surface hops may actually be needed before products are finally reached. The performance of different functionals is then assessed by comparison of TDDFT and diffusion Monte Carlo potential energy curves along a typical TDDFT TDA/SH reaction path. Finally, although true ( $S_0, S_1$ ) conical intersections are expected to be absent in adiabatic TDDFT, we show that the TDDFT TDA is able to *approximate* a conical intersection in this system.

## 6.1 Introduction

Since the introduction of linear response (LR) equations [20,85,86] for time-dependent density-functional theory (TDDFT) [19,41], LR-TDDFT (usually referred to as just TDDFT) has become, with few exceptions [83], the single-reference method of choice for extracting information about electronic excited states of medium and large-sized molecules. As such, TDDFT has become a standard part of the photochemical modelers' toolkit as evinced by several recent papers [87–98]. While TDDFT is formally exact, its accuracy is limited in practice by the need to use approximate functionals [99]. Nevertheless TDDFT is for some purposes computationally more than competitive with other tools in the photochemical modelers' toolkit. This is why TDDFT is often used to predict absorption spectra, to optimize excited-state geometries needed for modeling fluorescence spectra, and to examine the beginning and end of photochemical reactions. In contrast, many questions surround the use of TDDFT in the in between region where the ground and excited state become energetically degenerate or nearly degenerate and biradicals (or biradicaloids) are formed as bonds are broken. This is precisely the region where traditional wisdom says that multireference methods, such as CASSCF, are required. Relatively little is known about how TDDFT works or how rapidly TDDFT fails in approaching this region, hence the need to troubleshoot TDDFT for photochemical applications. This troubleshooting is further complicated by the possibility of different types of photochemical reaction mechanisms [1], some of which may prove more problematic than others. Thus a realistic assessment of TDDFT for a given photochemical reaction involves studying not just the local quality of electronic potential energy surfaces (PESs) but predicting entire reaction mechanisms. One way to do this is the “pathway method” in which minimum energy pathways (MEPs) are mapped out on excited state PESs between the initial Franck-Condon points obtained by vertical excitations and minima or conical intersections. However a better way is to carry

out photochemical dynamics since, unlike thermal reactions, photochemical reactions often have excess energy and so need not follow MEPs, and surface hopping depends on dynamical details and not just energy. Once the physically relevant pathways have been determined, the quality of TDDFT with different functionals can be assessed for a given photochemical reaction. We report just such a study of oxirane photochemical ring opening where we find TDDFT to give a remarkably good description of the physically relevant parts of the important PESs.

Some of the ground work for this article has been laid by a previous article that we shall refer to as Oxirane I (Ref. [49]). The objective of Oxirane I was to troubleshoot TDDFT as a potential method for *ab initio* molecular photodynamics calculations, using oxirane as a simple example where “TDDFT ought to work.” The quality of TDDFT for calculating vertical excitation spectra and potential energy curves along symmetric CC ring opening pathways was investigated by comparison with experiments and with high-quality quantum Monte Carlo (QMC) results. Well-known problems of TDDFT [99], including the artificially low ionization threshold [100], problems due to lack of explicit two-electron excitations [101, 102], and triplet (and singlet) instabilities [103], were treated in detail. No charge transfer excitations were encountered, so the well-known underestimation of charge transfer excitations in TDDFT [83] was not a concern. The main difficulty encountered with TDDFT turned out to be the triplet instability problem which could be largely circumvented by using the Tamm-Dancoff approximation (TDA) [48]. Since conventional wisdom suggests that symmetric ring-opening should be governed by the Woodward-Hoffman rules, con- and disrotatory ring opening were also investigated. However experimental investigations indicate that photochemical ring opening of oxirane most likely proceeds via asymmetric breaking of the CO  $\sigma$  bond, which is probably best investigated via a mixed quantum/classical surface hopping (SH) trajectory treatment.

Semiclassical trajectory SH methods [27, 30, 56] have been used extensively to study photochemical processes [18, 104–115]. The potential energy surfaces (PESs) used in these studies are either experimentally-derived fit functions or are calculated on-the-fly using a semiempirical or *ab initio* electronic structure method. *Ab initio* molecular dynamics (AIMD) is based upon the calculation of forces using parameter-free *ab initio* quantum chemical methods such as the complete active space self-consistent field (CASSCF) method. While CASSCF calculations with a suitably chosen active space can provide a chemically satisfying description of the bond making and breaking, the choice of the active

space is nontrivial and cannot be automatized and CASSCF calculations rapidly increase in expense as the molecules treated grow in size. For this reason it is highly desirable to explore other computationally simpler approaches such as time-dependent density-functional theory (TDDFT) for applications in photochemical AIMD [28].

The basic technology needed to carry out TDDFT/SH calculations is just becoming available. A prerequisite is the availability of TDDFT excited-state nuclear gradients, which have now been implemented in many quantum chemistry programs [52–54, 116–119]. In particular, the implementation of TDDFT TDA analytic gradients in the Car-Parrinello molecular dynamics code CPMD [52] has led to a few mixed TDDFT TDA/classical dynamics studies of electronic excited states [120–122] albeit without SH. Important pioneering work by Craig, Duncan, and Prezhdo [50] did incorporate SH into a crude form of TDDFT obtained by neglecting the exchange-correlation kernel. Consequently neither the excitation energies nor the associated forces could be considered accurate. This deficiency has only recently been corrected by the work of Tapavicza, Tavernelli, and R othlisberger [21] who implemented Tully’s fewest switches (FS) SH algorithm [30] finally permitting full TDDFT/SH calculations.

In the next section, we briefly review the TDDFT/SH method. The results of oxirane TDDFT/SH calculations are given in Sec. 6.3 where a detailed picture emerges of how the photochemical ring opening of oxirane takes place, in very good agreement with the mechanism previously proposed by Gomer and Noyes [123]. Having determined the principle photochemical mechanism predicted by TDDFT, we are in an excellent position to evaluate the real importance along this path of varying the density functional and this is done in Sec. 6.4.

An important debate which arose during the preparation of Oxirane I and of this work concerns the question of the existence of conical intersections in TDDFT. Levine, Ko, Queeneville, and Martinez have made a good case against the existence of true conical intersections in TDDFT [102], casting doubt on the utility of TDDFT for photochemical modeling. For this reason, we examine the critical region of the oxirane potential energy surfaces in Sec. 6.5 and report our finding of an approximate TDDFT conical intersection.

Section 6.6 summarizes and concludes.

## 6.2 Theoretical Methods

The primary theoretical methods used in this paper are TDDFT, TDDFT/SH, QMC, and CASSCF. The excited-state QMC methodology used in this paper has been previously presented in Oxirane I and Refs. [124–126]. The CASSCF is now well-established part of *ab initio* quantum chemistry and its description can be found in appropriate textbooks [32]. The basic principles of TDDFT have also been reviewed in Oxirane I and more detailed information can be obtained from a recent textbook [41]. In contrast, the TDDFT/SH method [21] is still very recent and plays a central role in this paper. As such it merits presentation here.

In this AIMD approach, the quantum wave packet or ensemble of wave packets describing the nuclear degree of freedom is replaced by an ensemble of classical trajectories, corresponding to different reaction paths and hence giving information about reaction products and corresponding relative yields. Most of the time the trajectories are propagated classically on either an excited-state or on the ground-state Born-Oppenheimer (BO) PES, but non-BO dynamics is also allowed to occur via special nonadiabatic SH techniques when PESs become energetically quasidegenerate. Two SH techniques are used here, namely the phenomenological Landau-Zener (LZ) theory [127–130] and Tully’s fewest switches (FS) theory [27, 30, 56]. While the FS theory is more rigorous than the LZ approach, neither theory is completely rigorous since neither theory is able to take into account the transition between quantum decoherence and coherence as PESs converge and diverge, nor do they take into account Berry phase effects which occur in the neighborhood of conical intersections. Perhaps more importantly the LZ and FS theories were developed in an era when conical intersections (CXs) were felt to be rare and so were designed with avoided crossings (ACs) in mind. A more modern picture is that surface hopping occurs by passing through CXs or perhaps through seams where surfaces cross. This is why modern practice dictates that these regions be referred to as funnels in the absence of further characterization (see for example Ref. [1] p. 22). Neither LZ nor FS theory really applies at the points of surface crossing, but this does not normally pose an obstacle to practical calculations. An exception is  $S_0 \rightarrow S_1$  SH which we chose to make irreversible for reasons discussed in Sec. 6.5. Despite these caveats, we expect our TDDFT TDA/SH calculations to give qualitatively correct reaction mechanisms and order of magnitude estimates of reaction rates.

The LZ theory is in principle only valid for AC-like situations. These may arise either as a true AC

due to remixing of near-lying diabatic states or as effective ACs seen by a trajectory passing near but not through a CX. In practice, switching probabilities are determined purely on the basis of the form of the PES. This means that LZ theory can be applied as soon as PESs have been generated by adding TDDFT excitation energies to DFT ground state energies. SH only occurs at special points along a trajectory which correspond to a minimum in the energy difference,  $\Delta E_{\text{adia}}$ , between two adiabatic states. At these points the switching probability is evaluated as [131],

$$P_{I,J}^{\text{LZ}} = \exp\left(-\frac{\pi^2 \Delta E_{\text{adia}}^2}{h(d|\Delta E_{\text{dia}}|/dt)}\right), \quad (6.1)$$

where the rate of change of the diabatic energy difference,  $\Delta E_{\text{dia}}$ , is evaluated as in Ref. [131] as the maximum of the rate of change of the adiabatic energy difference as the AC is approached.

The LZ scheme is easier to program and is somewhat less expensive than the FS method which will now be described. However no direct account is taken of the nature of the two electronic states.

Tully's theory [30] does take into account the nature of the electronic states. In this approach the nuclear coordinates,  $\mathbf{R}(t)$ , are propagated classically, while the electronic wave function satisfies the equation,

$$\hat{H}_{\text{el}}(\mathbf{R}(t))\Psi(\mathbf{r}, t) = i\hbar \frac{\partial}{\partial t} \Psi(\mathbf{r}, t). \quad (6.2)$$

The electronic wave function  $\Psi(\mathbf{r}, t)$  is a function of the electron coordinates,  $\mathbf{r}$ . Equation (6.2) is solved by expanding,

$$\Psi(\mathbf{r}, t) = \sum_I \Psi_I(\mathbf{r}; \mathbf{R}(t)) C_I(t), \quad (6.3)$$

where the BO states  $\Psi_I(\mathbf{r}; \mathbf{R}(t))$  satisfy the usual equation,

$$\hat{H}_{\text{el}}(\mathbf{R}(t))\Psi_I(\mathbf{r}; \mathbf{R}(t)) = E_I(\mathbf{R}(t))\Psi_I(\mathbf{r}; \mathbf{R}(t)). \quad (6.4)$$

$|C_I(t)|^2$  can be interpreted as the population of state  $I$  at time  $t$ . Inserting Eq. (6.3) into Eq. (6.2) yields an equation for the  $C_I(t)$ , namely

$$i\hbar \dot{C}_I(t) = E_I C_I(t) - i\hbar \sum_J \sigma_{I,J}(t) C_J(t), \quad (6.5)$$



where the nonadiabatic coupling (NAC) matrix elements are defined by

$$\begin{aligned}\sigma_{I,J}(t) &= \int \Psi_I^*(\mathbf{r}; \mathbf{R}(t)) \frac{\partial}{\partial t} \Psi_J(\mathbf{r}; \mathbf{R}(t)) d\mathbf{r} \\ &= \langle I(t) | \frac{\partial}{\partial t} J(t) \rangle.\end{aligned}\quad (6.6)$$

In practice, we compute NAC matrix elements directly via the finite difference scheme,

$$\sigma_{I,J}(t) = \frac{\langle I(t) | J(t + \Delta t) \rangle - \langle I(t + \Delta t) | J(t) \rangle}{2\Delta t}.\quad (6.7)$$

Following Tully's recipe [30], a hop from state  $I$  to state  $J$  is made if and only if,

$$\zeta < g_{I,J}(t, \Delta t),\quad (6.8)$$

where  $\zeta \in [0, 1]$  is a random number and,

$$g_{I,J}(t, \Delta t) = -2 \int_t^{t+\Delta t} \frac{\Re[C_J(\tau)C_I^*(\tau)\sigma_{JI}(\tau)]}{C_I(\tau)C_I^*(\tau)} d\tau.\quad (6.9)$$

Unlike LZ theory, the FS method requires NAC elements which must somehow be extracted from TDDFT. This problem has already been reviewed in some detail in Appendix A of Oxirane I where it is concluded that, at least, the NAC between the ground and excited states can be calculated formally exactly within LR-TDDFT. Recently, several implementations to compute NACs within TDDFT were published [21, 59, 74, 75]. The approach [21] used in the present work adapts Casida's assignment ansatz [20] for the adiabatic excited states,

$$\Phi_K(\mathbf{r}; \mathbf{R}) = \sum_{i=1}^{N_{\text{occ}}} \sum_{a=N_{\text{occ}}+1}^{N_{\text{occ}}+N_{\text{virt}}} c_{ia}^K \Phi_i^a(\mathbf{r}; \mathbf{R}),\quad (6.10)$$

where  $\Phi_i^a = \hat{a}_a^\dagger \hat{a}_i \Phi_0$  is a singly excited Kohn-Sham (KS) determinant, and the ground state wavefunction is approximated by the closed shell single KS Slater determinant. This is sufficient to be able to calculate the NACs via Eq. (6.7). Note that no restriction is placed on the indices  $I$  and  $J$  so that neither need be the ground state.

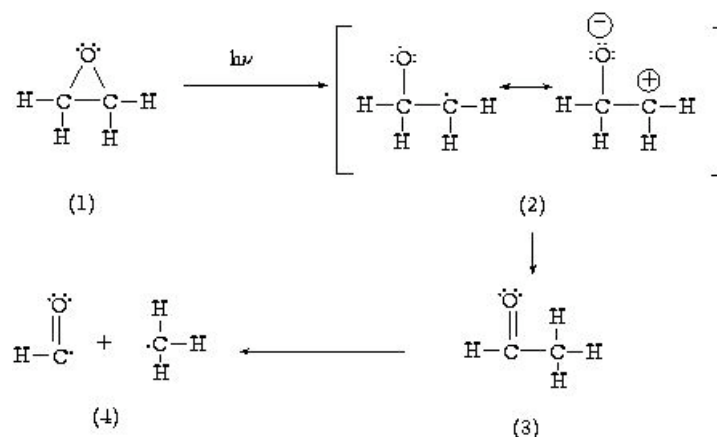


Figure 6.1: Mechanism proposed by Gomer and Noyes [123].

### 6.3 TDDFT/SH Dynamics

In 1950, based upon what was known experimentally at the time, Gomer and Noyes postulated the mechanism shown in **Fig. 6.1** for the photochemical ring opening of oxirane. This mechanism was confirmed experimentally by Kawasaki, Ibuki, Iwasaki, and Takezaki in 1973 [132]. However it is only a rather rough mechanism in the sense that it is not state specific. That is, it does not explain which electronic states are responsible for the reaction (nor why these states should be responsible), the nature of the funnel where the reaction passes from the excited states to the ground state, nor which parts of the reaction occur on the ground state surface. Our TDDFT/SH simulation can answer the question of whether or not TDDFT predicts the same mechanism and will provide state specific information. We will not be able to run the simulation long enough to obtain quantitative information about reaction yields, but the simulation will suggest likely products.

We will restrict our simulation to reactions initiated in the two lowest excited states. Simulation conditions are thus comparable to those of the photolysis experiment of Kawaski, Ibuki, Iwasaki, and Takezaki [132] since the experimental photon energies (0.67-6.95 and 7.11 eV) can be expected to populate only the lowest excited states of oxirane. According to Oxirane I and further analysis given in Subsec. 6.4.2, these are Rydberg-type  ${}^1B_1(n, 3s)$  and  ${}^1B_1(n, 3p_z)$  states. Both transitions have significant oscillator strength. A dark  ${}^1A_2(n, \sigma_{CC}^*)$  state could also conceivably enter into the photochemical reaction through nonadiabatic coupling with the other two states, but this will be included automatically in our simulation. The orbitals in question are shown in **Fig. 6.2**.

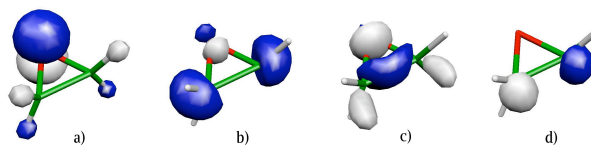


Figure 6.2: Ground state orbitals obtained using the PBE functional at the equilibrium geometry: a) HOMO [ $b_1(n)$ ], b) LUMO [ $a_1(3s)$ ], c) LUMO+1 [ $a_1(3p_z)$ ], and d) LUMO+2 [ $b_2(\sigma^*)$ ].

### 6.3.1 Computational Details

The TDDFT/SH simulations are carried out using the CPMD code [52, 62] and the implementation described in Section 6.2 and Ref. [21]. We use a plane wave basis (PW) with a cutoff of 70 Ry and norm-conserving pseudopotentials of Troullier and Martins [67]. We employ the isolated system module in CPMD, which allows us to study an isolated molecule within periodic boundary conditions, placing the molecule at the center of a cubic box of  $11 \times 11 \times 11 \text{ \AA}^3$ . We always employ the PBE functional [66].

Starting geometries and nuclear velocities are taken from a Boltzmann ensemble at 300 K generated by ground state BO molecular dynamics (MD) in the NVT ensemble using a Nosé-Hoover thermostat. Following the Franck-Condon approximation, the TDDFT/SH simulation is initiated by vertical excitation into either the  $^1(n, 3s)$  ( $S_1$ ) or  $^1(n, 3p_z)$  ( $S_2$  or  $S_3$ ) states. A timestep between 5 and 10 a.u. (1 a.u. = 0.024 fs) was used to propagate the classical degrees of freedom, while the time step to integrate the electronic degrees of freedom [Eq. (6.5)] was  $10^{-4}$  times smaller. The MD simulations are performed in the microcanonical (NVE) ensemble.

About 30 SH trajectories of each LZ and FS type with different starting geometries were generated and initiated in the  $^1(n, 3p_z)$  state. Five of these geometries were also initiated in the  $^1(n, 3s)$  state to perform both LZ and FS SH dynamics. This is too few trajectories to give a complete statistical description of all possible events, but we believe it allows us to identify the main reaction channels, predict reaction products, and to give an estimate about the time scale of the fragmentation reactions. One MD step takes about 9 min on 8 AMD Opteron 240 processors, so typically an excited state MD takes about 18 hours for 60 fs if a timestep of 10 a.u. is used.

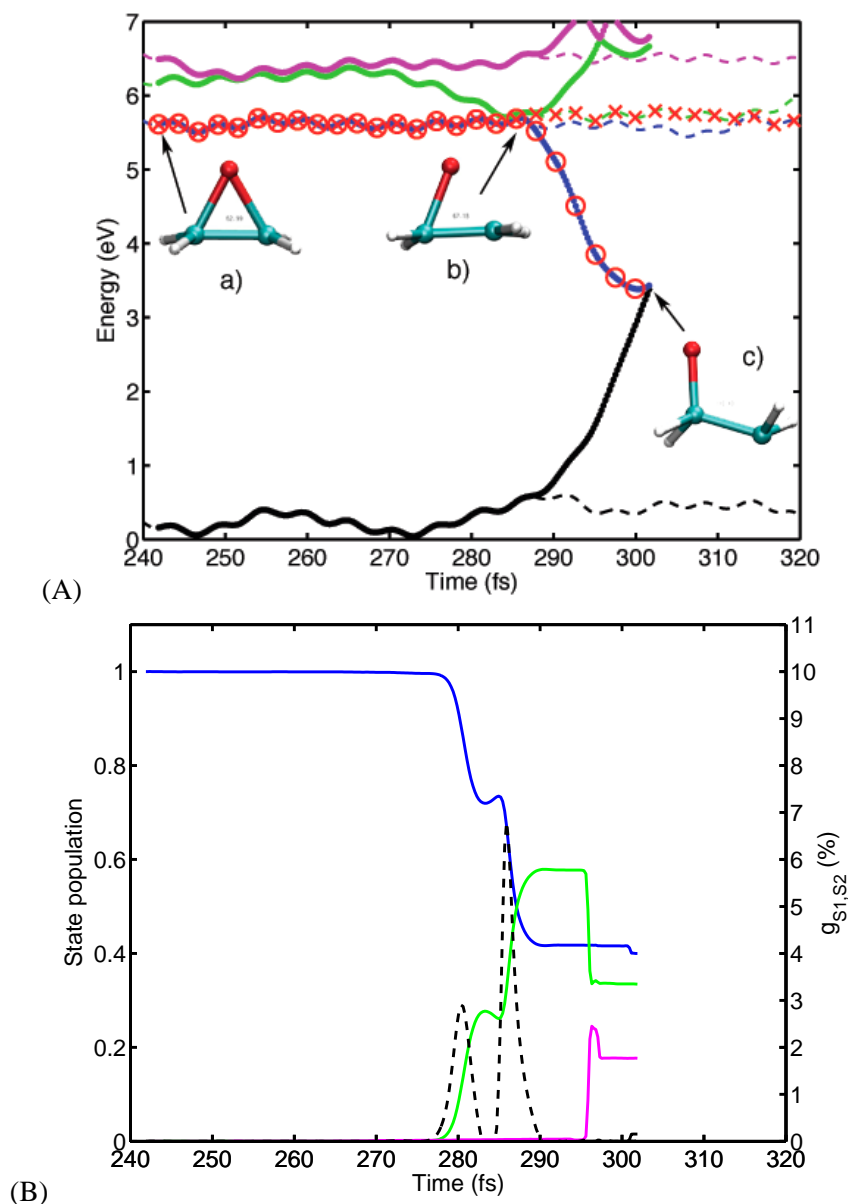


Figure 6.3: (A) Cut of potential energy surfaces along reaction path of a LZ (- -) and a FS (-) trajectory (black,  $S_0$ ; blue,  $S_1$ ; green,  $S_2$ ; magenta,  $S_3$ ). Both trajectories were started by excitation into the  $^1(n, 3s)$  ( $S_1$ ) state, with the same geometry and same initial nuclear velocities. The running states of the LZ and the FS trajectory are indicated by the red crosses and circles, respectively. (B) State populations (black,  $S_0$ ; blue,  $S_1$ ; green,  $S_2$ ; magenta,  $S_3$ ) and  $S_1 \rightarrow S_2$  FS hopping probability (dashed) as a function of time for the FS trajectory shown in (A).

### 6.3.2 Results

Kasha's rule [133] suggests that the first excited triplet ( $T_1$ ) or singlet ( $S_1$ ) is the most likely candidate for the initiation of a photochemical reaction. Since we are neglecting spin orbit coupling here, Kasha's rule implies that we should expect the reaction to begin from the  $S_1$  state which in our simulation is the  $^1(n, 3s)$  state (Subsec. 6.4.2). The results of a typical simulation initiated in the  $1^1B_1(n, 3s)$  state is shown in **Fig. 6.3**. The result of the LZ algorithm is that no reaction occurs during the first 320 fs and the system preserves the electronic character of the  $^1(n, 3s)$  state even at crossings to the  $^1(n, 3p_z)$  state. The FS algorithm does lead to a reaction, but only after the character of the running state changes from  $^1(n, 3s)$  to  $^1(n, 3p_z)$  state due to mixing between  $S_1$  and  $S_2$ . Thus the  $^1(n, 3s)$  state is a nonreactive channel, consistent with the nonbonding character of the orbital (Fig. 6.2). However the  $^1(n, 3s)$  state acts like an energy reservoir which can be tapped by the reactive  $^1(n, 3p_z)$  state via mixing of the states. In their study of the photochemistry of oxirane, Bigot, Sevin, and Devaquet [134] suggested that unreactive Rydberg states could act as just such an energy reservoir for reactive valence states. Perhaps surprisingly, Kasha's rule has given an incorrect description of our simulation since the state which is initially  $S_1$  is the unreactive channel. This is because Kasha's rule (which was initially based upon fluorescence studies) is for slow-enough reactions that radiationless relaxation has time to quench higher excited states. In the present case, the only mechanism for quenching the higher states is via SH and this does eventually lead to geometries where  $^1(n, 3p_z)$  is the  $S_1$  state.

**Figure 6.4** shows the main result obtained when the initial excitation is to the  $2^1B_1(n, 3p_z)$  state. In contrast to the previous case, now it is the FS algorithm that leads to longer reaction times than does the LZ algorithm, but both lead to rapid CO ring opening terminated by SH to the ground state at a CCO angle in the range 107-118°. The electronic reason for the rapid CO ring opening is shown in **Fig. 6.5** where the change in the orbital character is followed along a LZ trajectory. In the beginning of the trajectory (Fig. 6.5a), the active state is best characterized as  $^1(n, 3p_z)$ , whereas later (b,c,d) the active state is best characterized as  $^1(n, \sigma_{CO}^*)$ . While the  $3p_z$  and  $\sigma_{CO}^*$  orbitals share many qualitative similarities and one is easily and continuously changed into the other, the change from Rydberg to valence character helps to explain the rapid fall in energy of the active state and serves as an excellent illustration of the danger of assuming that Rydberg orbitals are too unreactive to be important for photochemistry. The conversion of potential energy into classical kinetic energy of the nuclei leads to a dynamically hot

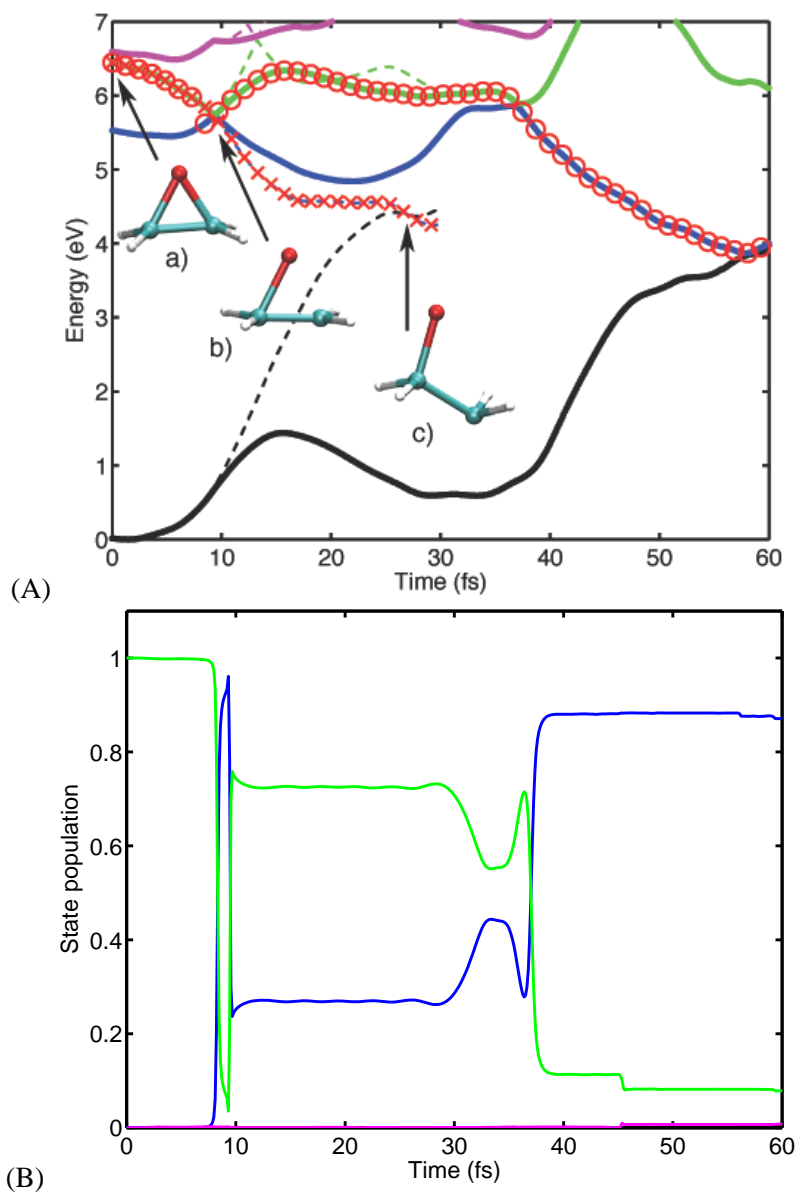


Figure 6.4: (A) Cut of potential energy surfaces along reaction path of a LZ (- -) and a FS (-) trajectory (black,  $S_0$ ; blue,  $S_1$ ; green,  $S_2$ ; magenta,  $S_3$ ). Both trajectories were started by excitation into the  $^1(n, 3p_z)$  ( $S_1$ ) state, with the same geometry and same initial nuclear velocities. The running states of the LZ and the FS trajectory are indicated by the red crosses and circles, respectively. The geometries of the LZ trajectory are shown at time a) 0, b) 10, and c) 30 fs. (B) State populations (black,  $S_0$ ; blue,  $S_1$ ; green,  $S_2$ ; magenta,  $S_3$ ) as a function of time for the FS trajectory shown in (A).

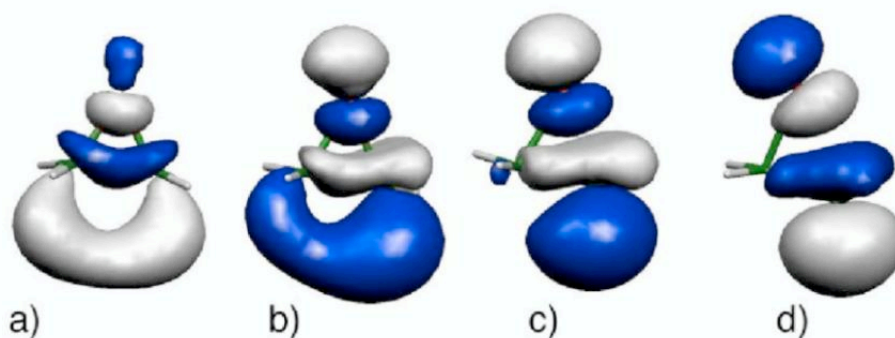


Figure 6.5: Change of character of the active state along the reactive LZ trajectory, shown in Fig. 6.4. Snapshots were taken at times a) 2.6, b) 7.4, c) 12.2, and d) 19.4 fs. For a) and b) the running state is characterized by a transition from HOMO to LUMO+1, while for c) and d) it is characterized by a HOMO-LUMO transition due to orbital crossing. HOMO remains all the time the oxygen nonbonding orbital.

molecule, that undergoes further reactions in the ground state, as will be discussed later.

As mentioned above and shown in greater detail in **Fig. 6.6**, FS leads to longer reaction times than does the LZ algorithm when the initial excitation is into the  $^1(n, 3p_z)$  state. Thus the LZ algorithm leads to reaction times on the order of 20-40 fs, while the FS algorithm leads to reaction times on the order of 50-100 fs. The reason for this will now be explained. LZ SH tends to switch close to or at points of surface crossing. Thus in Fig. 6.4, the LZ SH probabilities are typically about 99% in the  $S_2 \rightarrow S_1$  funnel region, so that basically all LZ trajectories switch adiabatic surface at this point. Unlike LZ SH, which is characterized by switching probabilities at isolated times, the FS SH algorithm is characterized by finite switching probabilities during nontrivial time intervals (Figs. 6.3B and 6.4B). This means, as can be clearly seen in Fig. 6.4A, that FS trajectories can SH before the funnel region and then recross to the original adiabatic state. In this example the system irreversibly jumps to the reactive state at the second passage through the funnel. This is the case in about half of the trajectories starting in the  $^1(n, 3p_z)$  state in Fig. 6.6B, while other trajectories need to pass the funnel region 3 or 4 times. Thus surface recrossing is the reason that reaction times are longer for the FS than for the LZ algorithm.

Had we used the pathway approach we would have followed minimum energy pathways and not seen the rich phenomenology and its impact on time scales resulting from SH between the  $^1(n, 3s)$  and  $^1(n, 3p_z)$  states. We would also not have seen certain other reactions which, though less probable, nevertheless occur. Thus oxygen abstraction was observed in one LZ trajectory (marked with \* in Fig. 6.6A). This reaction always occurs upon  $^1(n, 3p_z)$  excitation if simulations are started from the  $C_{2v}$

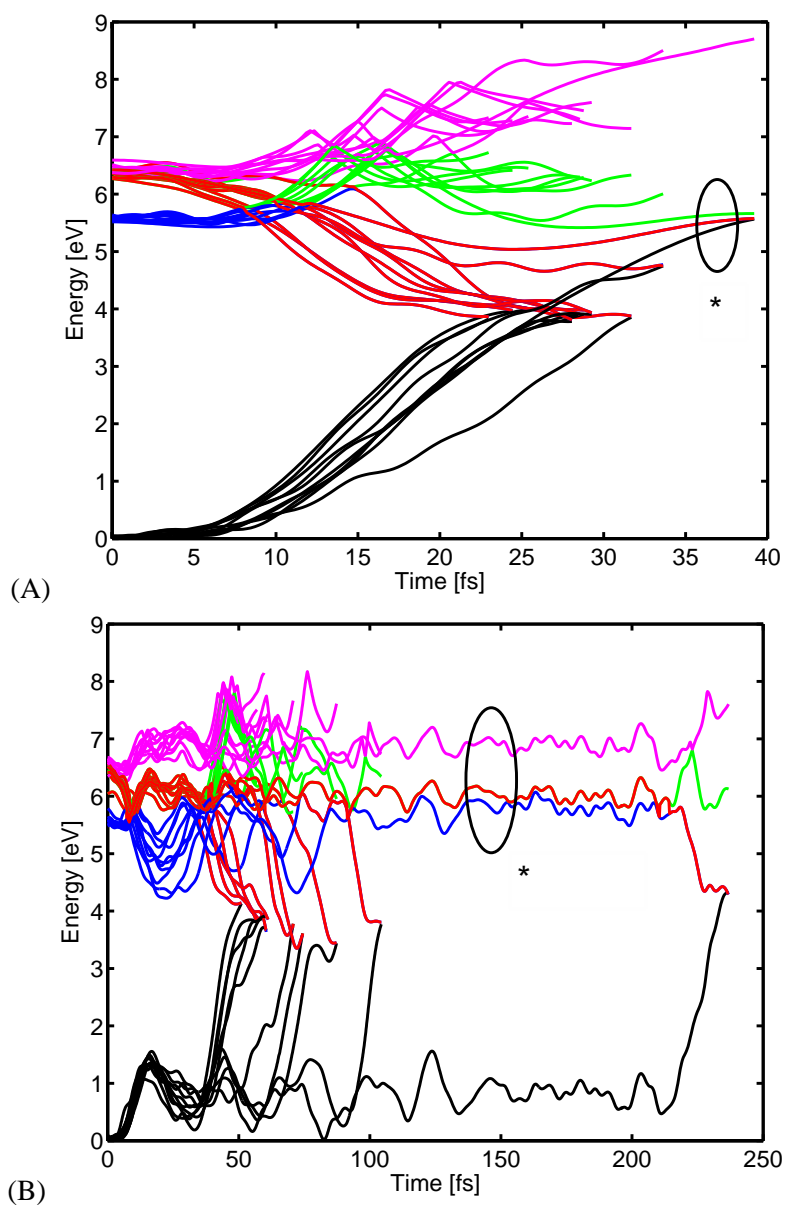


Figure 6.6: A swarm of 10 trajectories, starting in the  $^1(n, 3p_z)$  state (black,  $S_0$ ; blue,  $S_1$ ; green,  $S_2$ ; magenta,  $S_3$ ; red, running state). (A) LZ SH. The trajectory marked with an asterisk corresponds to the oxygen abstraction reaction. The other trajectories all lead the unsymmetric CO bond rupture. (B) FS SH. In the trajectory marked with an asterisk, the molecule is trapped in the unreactive  $^1(n, 3s)$  state. The other trajectories all lead the unsymmetric CO bond rupture.



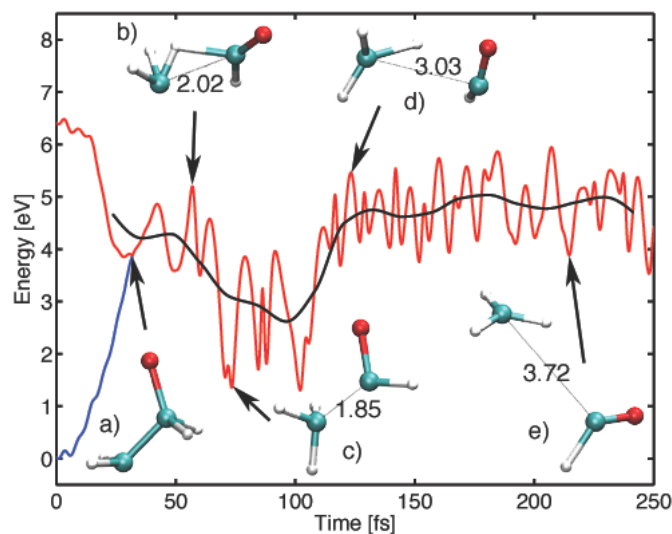


Figure 6.7: Fragmentation to  $\bullet\text{CH}_3$  and  $\bullet\text{CHO}$ . PES of the running state and its time average are shown in red and black, respectively. If  $S_0$  is not the running state, it is shown in blue. Structures were taken at times a) 31 fs, b) 56 fs, c) 72 fs, d) 122 fs, and e) 214 fs. CC distances ( $\text{\AA}$ ) are indicated.

symmetric ground state geometry instead of a structure from the 300 K Boltzmann distribution. The reason for this finding might be the symmetric forces along both CO bonds, inducing a simultaneous rupture of both bonds forming oxygen and ethylene. In another exceptional trajectory, this time using the FS algorithm, (\* in Fig. 6.6B), we find the contrary case of a molecule trapped in the unreactive state for about 200 fs, although it was initialized in the reactive state. In none of the trajectories, was the CC bond breaking observed as an initial step in the photochemistry, though we did find 2 trajectories in which the  $^1(n, \sigma_{CC}^*)$  state was temporarily populated in the first 10 fs after excitation.

Having described excited-state reactions, we will now focus on reactions occurring after the system has relaxed to the ground state. According to the calculations described above, by far the dominant process occurring in the excited state is CO bond rupture and CCO ring opening until the intersection geometry where  $S_0$  and  $S_1$  meet. At this point, much of the nuclear potential energy has been turned into kinetic energy and dynamical temperatures are around 4000 K. The first thing observed is a proton shift to give acetaldehyde [(3) in Fig. 6.1]. Thus our TDDFT/SH calculations fully validate the Gomer-Noyes mechanism up to this step and give the additional information that the proton shift is occurring in the ground electronic state (Fig. 6.7c). After this point, the molecule still has enough excess kinetic energy to undergo further reaction and we observe two different scenarios. The first is decomposition to  $\text{CH}_3\bullet$  and  $\text{CHO}\bullet$  (Fig. 6.7) while the second is formation of  $\text{CH}_4$  and CO (Fig. 6.8). Which of these

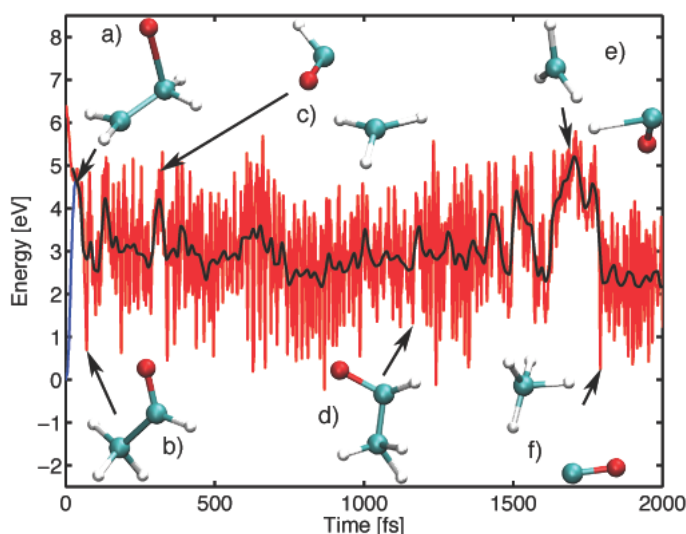


Figure 6.8: Formation of  $\text{CH}_4$  and  $\text{CO}$  (colors as in Fig. 6.7). Structures were taken at times a) 32, b) 70, c) 474, d) 1151, e) 1705, and f) 1792 fs.

two occurs depends on having just the right combination of internal motion. If the CC bond breaks irreversibly, without transferring a second proton, we observe the reaction to  $\text{CH}_3^\bullet$  and  $\text{CHO}^\bullet$ . Since this bond rupture requires surmounting an energy barrier, it does not always occur. Very often, we only observe large fluctuations of the CC bond distances, but the bond stays intact for several hundreds of femtoseconds (Fig. 6.8c,d). In the other scenario, the CC bond breaks and a second proton is transferred at this state, so that  $\text{CH}_4$  and  $\text{CO}$  are formed. While this scenario is less frequent than that forming  $\text{CH}_3^\bullet$  and  $\text{CHO}^\bullet$ , the reaction to form  $\text{CH}_4$  and  $\text{CO}$  from acetaldehyde is exothermic. The energetic order of the minimum and transition state geometries of the hot molecule reactions (see time averaged surfaces in Figs. 6.7 and 6.8) are consistent with the order obtained in recent elaborate computational studies, mapping the ground state PES of the decomposition of  $\text{CH}_3\text{CHO}$  and  $c\text{-C}_2\text{H}_4\text{O}$  [135–137].

Our simulation was set up to permit comparison with the photolysis experiment of Kawasaki, Ibuki, Iwasaki, and Takezaki [132]. Although there are some more recent studies of the decomposition of oxirane, they have focused on thermal rather than photoinduced decomposition [138–140]. Consistent with our prediction, Kawasaki *et al.* detect  $\text{CH}_3^\bullet$  and  $\text{CHO}^\bullet$  as the main photoproduct [(4) in Fig. 6.1]. However, while we have only observed oxygen abstraction once in our simulation, Kawasaki *et al.* find oxygen abstraction to be the dominant result at higher photon energies. This discrepancy between our simulations and their experimental results may be because the experiment was carried out at low temperature while our simulations were carried out from an ensemble of structures equilibrated at 300 K. This

hypothesis is consistent with the fact that oxygen abstraction occurs always upon excitation of the optimal ground state. Another conceivable contribution to the observed discrepancy between our simulation and the experiment is that our initial ensemble was a 300 K classical Boltzmann ensemble. Going from this to the corresponding quantum ensemble is expected to decrease the probability of observing structures near classical turning points by increasing the probability of observing the symmetric equilibrium structure. As remarked earlier such symmetric structures favor oxygen abstraction.

To summarize the results of this section, our TDDFT/SH simulation validates the experimentally-derived Gomer-Noyes mechanism for the photochemical ring-opening of oxirane. At the same time, we have learned much about the role of the  $^1(n, 3p_z)$  state as reactive channel and the role of the  $^1(n, 3s)$  state as an unreactive channel which can serve as an energy reservoir. We have discussed other rare reactions and which parts of the reaction occur when the dynamically-hot molecule returns to the ground state. These latter steps are consistent with the experimental observations of Kawasaki *et al.* who detected  $\text{CH}_3^\bullet$  and  $\text{CHO}^\bullet$  as the main photolysis products.

## 6.4 Functionals

Oxirane I presented a detailed analysis of the behavior of TDB3LYP, TDLDA, and TDLDA TDA  $C_{2v}$  potential energy curves compared against the results of high-quality diffusion Monte Carlo (DMC) calculations. The analysis was facilitated by the high symmetry constraint. The closely-related conrotatory and disrotatory CC ring opening potential energy surfaces were also presented and the relation to Woodward-Hoffmann theory was discussed. Oxirane I is however open to the criticism that the photochemical ring opening reaction proceeds via CO, rather than CC, bond breaking. Assessing the behavior of different types of TDDFT calculations along a more realistic pathway could conceivably lead to different conclusions, either the discovery of new problems or perhaps the discovery that the problems discovered in Oxirane I are less severe than expected. Thanks to the results of our TDDFT/SH calculations we are in a position to do just this. In particular, after briefly revisiting the vertical excitation spectrum (Subsec. 6.4.2) to examine the effects of functionals not treated in Oxirane I, we will take a careful look at the diversity of behavior possible for different types of TDDFT calculations for a typical  $^1(n, 3p_z)$ -initiated LZ ring-opening trajectory up to the point of SH to  $S_0$ .

### 6.4.1 Computational Details

QMC results are obtained with the program package CHAMP [141]. We use scalar-relativistic energy-consistent Hartree-Fock pseudopotentials and the corresponding cc-TZV basis [142] augmented with polarizations and diffuse functions as discussed in Oxirane I. The wave function is of the Jastrow-Slater type and consists of a three-body Jastrow factor multiplied by a CASSCF(4,5) determinantal component. All Jastrow and determinantal parameters are optimized within variational Monte Carlo by energy-minimization, using a weighted average scheme with equal weights if the excited state is not the lowest in its symmetry. For the computation of the  $2^1B_1$  and  $2^1A_1$  vertical excitations at the optimal  $C_{2v}$  ground state geometry, we average over the state of interest and the lower state of the same symmetry. For the geometries along a typical photochemical reaction path with no symmetry, we average over the lowest three states. The trial wave function is then used in diffusion Monte Carlo (DMC), and all QMC results presented in this work are from DMC calculations. See Oxirane I [49] for further details on our QMC calculations.

The TDDFT single-point calculations are performed using either a plane wave (PW) basis and the CPMD code [52, 62] or a localized basis and TURBOMOLE [78, 86].

PW calculations are performed in the same way as in the previous section, except that the box size was increased to  $30 \times 30 \times 30 \text{ \AA}^3$ . We use two different xc-functionals, the local density approximation (LDA) in the parameterization of Vosko, Wilk, and Nusair [143] and the generalized gradient functional of Perdew, Becke, and Ernzerhof (PBE) [66]. The TDDFT calculations using these functionals are denoted as TDLDA and TDPBE, respectively. For comparison TDLDA single point calculations were also carried out as post-SCF calculations using two different asymptotically-correct exchange-correlation model potentials, namely that of van Leeuwen and Baerends (LB94) [144] and the state-average orbital-dependent potential (SAOP) [145]. We use the notation TDLDA/LB94 or TDLDA/SAOP to designate a post-SCF TDLDA calculation where the SCF part of the calculation was carried out respectively with the LB94 or SAOP xc-potential.

The TDDFT spectra computed with TURBOMOLE are obtained using an aug-cc-pVTZ localized Gaussian basis set [146, 147]. Within TURBOMOLE, we use the PBE xc-functional [66] and the hybrid xc-functional PBE0 [148], which replaces 25% of PBE exchange by Hartree-Fock exchange. The TDDFT calculations using this functional are denoted as TDPBE0.

Table 6.1: DMC and experimental excitation energies (eV). DMC energies were computed for the PBE-optimized ground state  $C_{2v}^+$  symmetric structure. Assignment of the experiment are our own.

DMC	Assignment	Expt.
$7.51 \pm 0.02$	$1^1 B_1[b_1(n), a_1(3s)]$	$7.24^{a,b,c}$
$7.62 \pm 0.03$	$2^1 B_1[b_1(n), a_1(3p_z)]$	$7.45^b$
$8.06 \pm 0.02$	$1^1 A_2[b_1(n), b_2(\sigma^*)]$	
$8.64 \pm 0.02$	$2^1 A_1[b_1(n), b_1(3p_x)]$	$7.88^a, 7.89^b$

<sup>a</sup> Ref. [149], <sup>b</sup>Ref. [150], <sup>c</sup>Ref. [151].

### 6.4.2 Vertical Excitation Energies

Although the vertical excitation spectrum was discussed in some detail in Oxirane I, only a few functionals were considered. The discussion of the vertical excitation spectrum is here extended to a wider range of functionals. The primary comparison in Oxirane I for the vertical excitation spectrum was the experimental absorption spectrum. Here we take the results of our DMC calculations.

**Table 6.1** compares the results of our DMC calculations against the experimentally-observed excitation energies. Our calculations imply that the two lowest experimental energies probably correspond to the lowest two  $1^1 B_1$  DMC states, which we describe in orbital terms as  $1(n, 3s)$  and  $1(n, 3p_z)$  (Fig. 6.2). A definite assignment of the two lowest experimental energies would require a more sophisticated model that takes into account vibronic effects [152–154]. This is especially true since we now know that we are in the presence of a photochemically active species where vibronic coupling is likely to be important. These vibronic effects are of course absent in our TDDFT calculations, for which the DMC calculations are the proper point of comparison, rather than experiment.

**Table 6.2** compares TDDFT spectra calculated in the TDA with the DMC results. The TDLDA and TDPBE lead to excitation energies which are underestimated by over 1 eV. An important source of difficulty is the now well-understood phenomenon [100] that the TDDFT ionization threshold lies at minus the energy of the highest occupied molecular orbital (HOMO). Since the asymptotic fall off of the LDA and GGA exchange-correlation potentials is exponential rather than as the correct  $1/r$ , the TDDFT ionization potential is underestimated by about 4 eV (compare the value of  $-\epsilon_{\text{HOMO}}$  given in the footnotes of Table 6.2 with the experimental ionization potential of 10.57 eV [155].) The first three calculated TDLDA and TDPBE excitation energies are just below  $-\epsilon_{\text{HOMO}}$ . This is expected to lead to bound but underestimated excitations, which does indeed seem to be the case. One way to improve the asymptotic

Table 6.2: TDDFT/TDA excitation energies ( $\omega$ ), deviations from corresponding DMC value ( $\Delta = \omega_{TDDFT} - \omega_{DMC}$ ), oscillator strengths ( $f$ ) and assignment. Computations were carried out using a plane wave basis, except for the TDPBE0 calculations where the aug-cc-pVTZ basis was used.

$\omega$ (eV)	$\Delta$ (eV)	$f$	Assignment
TDLDA <sup>a</sup>			
5.902	-1.61	0.00416	$1^1 B_1[b_1(n), a_1(3s)]$
6.321	-1.30	0.00065	$2^1 B_1[b_1(n), a_1(3p_z)]$
6.330	-1.71	0.00000	$1^1 A_2[b_1(n), b_2(\sigma^*)]$
6.343		0.00029	$3^1 B_1$
6.932		0.00185	$2^1 A_1$
TDPBE <sup>b</sup>			
5.772	-1.738	0.00381	$1^1 B_1[b_1(n), a_1(3s)]$
6.191	-1.869	0.00000	$1^1 A_2[b_1(n), b_2(\sigma^*)]$
6.211	-1.409	0.00043	$2^1 B_1[b_1(n), a_1(3p_z)]$
6.244		0.00050	$3^1 B_1$
6.265		0.00194	$2^1 A_1$
TDPBE0 <sup>c</sup>			
6.903	-0.607	0.023	$1^1 B_1[b_1(n), a_1(3s)]$
7.277	-0.343	0.013	$2^1 B_1[b_1(n), a_1(3p_z)]$
7.338	-0.722	0.000	$1^1 A_2[b_1(n), b_2(\sigma^*)]$
7.492		0.016	$2^1 A_1$
7.892		0.000	$2^1 A_2$
TDLDA/SAOP			
7.985	0.48	0.00986	$1^1 B_1[b_1(n), a_1(3s)]$
8.093	0.47	0.00094	$2^1 B_1[b_1(n), a_1(3p_z)]$
8.451	0.39	0.00000	$1^1 A_2[b_1(n), b_2(\sigma^*)]$
8.511		0.00004	$2^1 A_1$
8.565		0.00096	$3^1 A_1$
TDLDA/LB94			
7.597	0.09	0.00748	$1^1 B_1[b_1(n), a_1(3s)]$
7.712	0.09	0.00266	$2^1 B_1[b_1(n), a_1(3p_z)]$
8.076	0.02	0.00000	$1^1 A_2[b_1(n), b_2(\sigma^*)]$
8.280		0.00170	$2^1 A_1$
8.305		0.00170	$3^1 A_1$

<sup>a</sup>For the LDA,  $-\epsilon_{\text{HOMO}} = 6.330$  eV.

<sup>b</sup>For PBE,  $-\epsilon_{\text{HOMO}} = 6.217$  eV.

<sup>c</sup>For PBE0,  $-\epsilon_{\text{HOMO}} = 7.913$  eV.

behavior of the exchange-correlation potential, and thus to shift  $-\epsilon_{\text{HOMO}}$  up in energy, is by introducing some amount of Hartree-Fock exchange. It was demonstrated in Oxirane I through explicit results with the B3LYP functional that hybrid functionals can lead to a significant improvement in TDDFT energies. This is also seen with the TDPBE0 functional in the present work, which has increased  $-\epsilon_{\text{HOMO}}$  by about 1.6 eV compared to either the LDA or PBE approximations and reduces the error in the excitation energies to about half that found with the TDLDA or the TDPBE. However the biggest improvement seen in Table 6.2 is due to the use of the explicitly asymptotically-corrected functionals SAOP and LB94 which lead to  $-\epsilon_{\text{HOMO}}$  of 11.01 and 11.84 eV [156] in reasonable agreement with the experimentally observed ionization potential of about 10.57 eV. In fact, the TDLDA/LB94 excitation energies are in excellent agreement with the DMC energies and the TDLDA/SAOP excitation energies are also acceptable. As we shall see, the superiority of these potentials is less clear when we look at entire potential energy curves.

### 6.4.3 Potential Energy Curves

We now turn our attention to how different TDDFT approaches behave along a typical reaction path. Geometries were taken every 2.4 fs from one of the fast relaxing LZ SH trajectories of Subsec. 6.3 initiated in the reactive  $^1(n, 3p_z)$  state reflecting the main features of the fast decay channel. Snap shots of the trajectory are shown in Fig. 6.4. Since the main motion of the molecule is the opening of the CCO angle, we have chosen to measure the progress of the reaction, not by time, but by the CCO angle.

**Figure 6.9** compares PESs of TDPBE/LR, TDPBE/TDA PESs, and DMC. An unphysical cusp was found in Oxirane I in the  $C_{2v}$  ring-opening curve for the  $1^1A_1$  surface at the point where the CC bond breaks. At this point a triplet instability was observed in the  $1^3B_2$  state and a near singlet instability was observed in the  $1^1B_2$  state at similar bond distances. While  $B_2$  states are too high in energy to be important for the present study, the corresponding initial singlet states for CO bond breaking is the  $1^1B_1(n, 3p_z)$  state. Unless the TDA is made, a singlet instability is indeed observed for this state. We can understand the difference between full LR and TDA results in more detail by using the same two-orbital model for a hypothetical  $^1(i, a)$  transition used in Oxirane I. In this model, the LR singlet excitation energy is,

$$\omega_{LR} = \sqrt{(\epsilon_a - \epsilon_i)[(\epsilon_a - \epsilon_i) + 2(ai|2f_H + f_{xc}^{\uparrow,\uparrow} + f_{xc}^{\uparrow,\downarrow}|ai)]}, \quad (6.11)$$

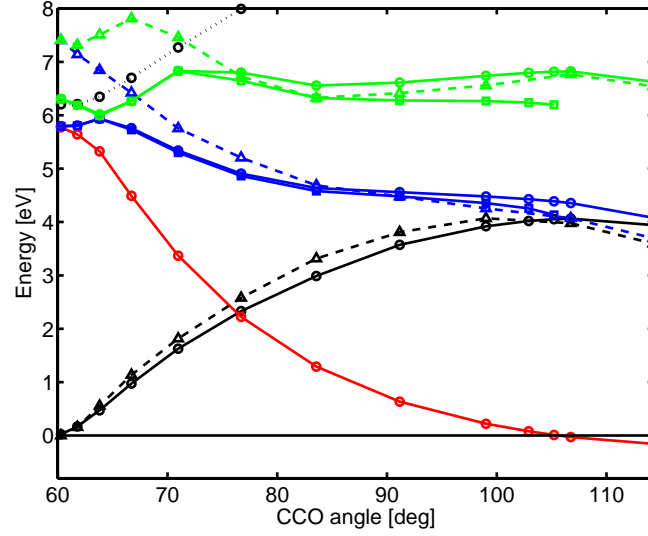


Figure 6.9: Comparison of the DMC (dashed, triangles) PES, TDPBE/TDA (circles), and TDPBE/LR (squares). Also shown are the PBE  $S_0$  curve (black, circles), the HOMO-LUMO gap ( $\epsilon_{\text{LUMO}} - \epsilon_{\text{HOMO}}$ , red), and the TDPBE ionization threshold at  $(-\epsilon_{\text{HOMO}}, \text{dotted, open circles})$ . The (TD)PBE calculations were carried out with TURBOMOLE using the aug-cc-pVTZ basis. Black,  $S_0$ ; blue,  $S_1$ ; green,  $S_2$ .

and the corresponding TDA singlet excitation energy is,

$$\omega_{TDA} = (\epsilon_a - \epsilon_i) + (ai|2f_H + f_{xc}^{\uparrow,\uparrow} + f_{xc}^{\uparrow,\downarrow}|ai). \quad (6.12)$$

Here the  $\epsilon_r$  are orbital energies and

$$(pq|f|rs) = \int \int \psi_p^*(\mathbf{r})\psi_q(\mathbf{r})f(\mathbf{r}, \mathbf{r}')\psi_r^*(\mathbf{r}')\psi_s(\mathbf{r}') d\mathbf{r}d\mathbf{r}', \quad (6.13)$$

where  $f$  can be either the Hartree kernel,

$$f_H(\mathbf{r}_1, \mathbf{r}_2) = 1/r_{12}, \quad (6.14)$$

or the xc-kernel,

$$f_{xc}^{\sigma,\tau}(\mathbf{r}_1, \mathbf{r}_2) = \frac{\delta^2 E_{xc}[\rho_{\uparrow}, \rho_{\downarrow}]}{\delta\rho_{\sigma}(\mathbf{r}_1)\delta\rho_{\tau}(\mathbf{r}_2)}. \quad (6.15)$$

It follows that,

$$\omega_{TDA}^2 - \omega_{LR}^2 = (ai|2f_H + f_{xc}^{\uparrow,\uparrow} + f_{xc}^{\uparrow,\downarrow}|ai)^2 \geq 0, \quad (6.16)$$



so that TDA excited states should lie above the corresponding LR quantities. This is indeed what is seen in Fig. 6.9. The integral over the kernels is typically small and positive. This means that the  $S_0 \rightarrow S_1$  excitation energy is given roughly by the HOMO  $\rightarrow$  LUMO gap, also shown in Fig. 6.9. However Fig. 6.9 also shows that the difference between corresponding TDA and LR curves grows for  $S_1$  as the CCO angle increases. (This difference is even more dramatic for the  $S_2$  state.) This is consistent with the previously noted change in orbital character. In the beginning of the ring opening, the  $^1(n, 3p_z)$  excitation has primarily Rydberg character and the integral over kernels is small because the  $3p_z$  orbital is diffuse. However as the ring opening progresses, the  $S_1$  states takes on more and more  $^1(n, \sigma_{CO}^*)$  valence character. This leads to a larger value of the integral over the kernels, and hence to a larger difference between the corresponding TDA and LR energies. Equation (6.11) shows that the LR singlet excitation energy actually become imaginary when the HOMO-LUMO gap (red curve in Fig. 6.9) passes through zero at about  $105^\circ$  and becomes negative. (Imaginary excitation energies are not shown in the Figure.) This is a singlet instability. In contrast [Eq. (6.12)], the corresponding TDA singlet excitation energies are real positive or negative numbers. The problem of imaginary excitation energies was extensively discussed in Oxirane I in the context of singlet and triplet instabilities where it was recommended to circumvent the problem by using the TDA.

Let us now turn our attention to how the TDPBE and QMC potential energy curves compare. In Fig. 6.9 DMC values for  $S_1$  and  $S_2$  are above  $-\epsilon_{\text{HOMO}}$  at small CCO angles, and fall below the ionization threshold at angles larger than  $\approx 70\text{-}80^\circ$ . According to our previous remarks about TDDFT having an artificially low ionization threshold [100], we should expect better agreement between the TDPBE and DMC calculations when the true excitation energy is below the  $-\epsilon_{\text{HOMO}}$  predicted by PBE. Exactly this is reflected by our calculations, where DMC values are above the ionization threshold predicted by PBE, the discrepancy between DMC and TDPBE curves is considerably larger than at higher CCO angles, where DMC excitation energies fall below  $-\epsilon_{\text{HOMO}}$ . This difference diminishes dramatically for the  $S_1$  state as the CCO angle opens and on the whole the TDPBE/TDA and QMC calculations come into relatively good agreement.

Hybrid functionals help to circumvent the problem of low-lying ionization thresholds because  $-\epsilon_{\text{HOMO}}$  increases with the amount of Hartree-Fock exchange (see Table 6.2). Consequently, the TDPBE0 curves in **Fig. 6.10** are closer to the QMC curves for CCO angles below about  $70^\circ$ . However, at larger CCO

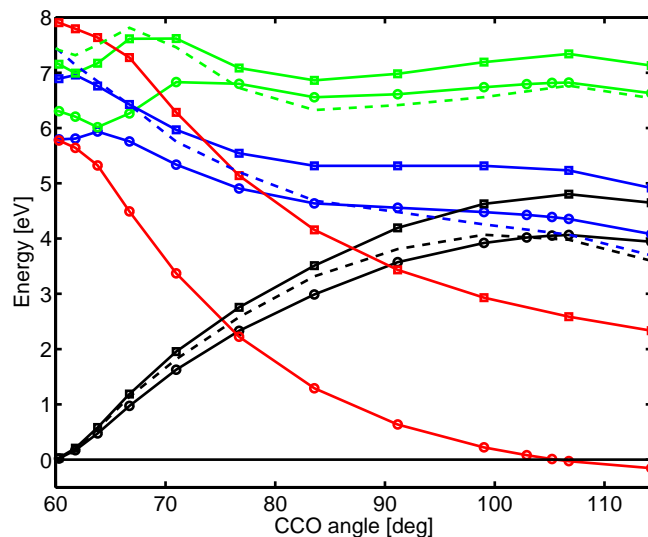


Figure 6.10: Comparison of the PESs of TDPBE/TDA (circles) and TDPBE0/TDA (squares). Also shown are the PBE (black, circles) and PBE0 (black, squares)  $S_0$  curves, and the PBE (red, circles) and PBE0 (red, squares) HOMO-LUMO gap ( $\epsilon_{\text{LUMO}} - \epsilon_{\text{HOMO}}$ , red). The (TD)PBE and (TD)PBE0 calculations were carried out with TURBOMOLE using the aug-cc-pVTZ basis. DMC results (dashed) are also shown. Black,  $S_0$ ; blue,  $S_1$ ; and green:  $S_2$ .

angles the PBE0 ground state potential energy curve overestimates more and more the DMC ground state curves, while pure PBE predicts a  $S_0$  potential energy curve similar to DMC. The overestimation of  $S_0$  by PBE0 and the slightly higher excitation energies by TDPBE0 leads to excited state curves that are too high in energy and also too flat compared to DMC. The overestimation of the  $S_0$  curve by the hybrid PBE0 functional at large CCO angles is consistent with the idea that increasing the amount of Hartree-Fock exchange leads to increasing difficulties describing electron correlation effects present in the CO bond breaking region. The good performance of PBE in describing the  $S_0$  PES leads to TDPBE curves that compare better to DMC than does TDPBE0, at large CCO angles, while TDPBE0 curves are superior to TDPBE when DMC values are above  $-\epsilon_{\text{HOMO}}$ .

We will now investigate how the asymptotically-corrected functionals perform along the reaction path. The TDLDA/LB94 and TDLDA/SAOP curves are qualitatively very similar, therefore we only discuss the PES obtained by TDLDA/SAOP which is shown together with the DMC curves in **Fig. 6.11**. Perhaps surprisingly the TDLDA/SAOP curves appear to have roughly the same strengths and weaknesses as the TDPBE0 method. That is, it compares well with the QMC results at small bond angles but the quality steadily decreases as the CCO angle opens.

Questions of accuracy aside, neither the TDPBE0 nor the TDLDA/SAOP is well-adapted for pho-

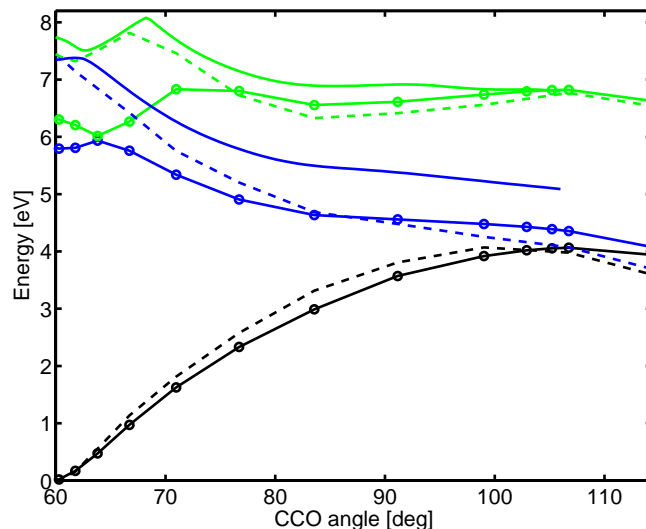


Figure 6.11: Comparison of the TDPBE/TDA (circles) and TDLDA/SAOP (solid) PES to DMC (dashed). Also shown is the TDPBE ionization threshold (dotted). Black,  $S_0$ ; blue,  $S_1$ ; green,  $S_2$ .

tdynamics calculations. Within a PW basis the hybrid TDPBE0 functional is computationally too expensive for carrying out a large number of on-the-fly calculations. The problem with the TDLDA/SAOP method is somewhat different. TDLDA/SAOP analytic gradients are the sum of analytic gradients of the LDA ground state energy and analytic gradients of the TDLDA/SAOP excitation energy. Bypassing the philosophical problem of whether or not exchange-correlation potentials and kernels calculated with different functionals should be mixed in a single calculation, TDLDA/SAOP gradients are simply not yet available. Thus it makes sense to continue carrying out future TDDFT SH dynamics calculations using the PBE functional. Based upon the preceding analysis, we know that at least the order of initial states is reasonably consistent with DMC. The fact that in the Franck-Condon region the deviation between TDPBE and DMC is maximal is worrisome in so far as dynamics starts slowly and so the reaction spends a significant amount of time near the initial geometries. However, as the reaction progresses, it also speeds up and enters a region where the TDPBE excited-state curves and the PBE ground-state curve compare relatively well with the corresponding QMC curves.

## 6.5 Conical Intersections in TDDFT

How conical intersections (CXs) are described in TDDFT has become something of an issue in the photodynamics community. The purpose of this section is to address these concerns both in general and

also in the specific context of our oxirane calculations.

It is useful to begin with a brief review of what is meant by a CX. The potential energy surface of a molecule with  $f$  internal degrees of freedom is an  $f$ -dimensional hypersurface in an  $(f + 1)$ -dimensional hyperspace. If two surfaces just cross without seeing each other, the seam where the surfaces intersect is an  $(f - 1)$ -dimensional hyperline. This is because one degree of freedom must be used in the seam space to maintain the constraint that the two surfaces have the same energy,  $E_I(\mathbf{R}) = E_J(\mathbf{R})$ . However surfaces whose energies are generated by diagonalizing a hamiltonian matrix,  $\mathbf{H}$ , must not only satisfy the constraint that  $E_I(\mathbf{R}) = E_J(\mathbf{R})$  but also that  $H_{I,J}(\mathbf{R}) = 0$ . This means that two degrees of freedom are actually used up to form a CX, which is an  $(f - 2)$ -dimensional hyperpoint. (A more explicit mathematical argument is given in Appendix 6.7.)

Up until the 1990s, CXs between molecular electronic excited states were generally thought of as something rare and largely unimportant. In 1992, Bernardi, Robb, and Olivucci undertook an ambitious project focusing on a systematic investigation of basic organic chromophores and were able to demonstrate low-lying CXs with structures related to the observed photoproducts (see Ref. [157] for a review). This was an important observation because photoreactions need fast routes to pass from excited reactants to ground-state products before other mechanisms such as fluorescence or radiationless relaxation kick in and return the reactants to their ground states. CXs can provide one such fast route and photochemical models should also provide a proper description of CXs.

Unfortunately not all electronic structure methods can correctly describe CXs. For example, typical  $(S_0, S_1)$  CXs for organic reactions are often described as biradicaloids and biradicals are notoriously difficult to describe with a single reference theory. In fact, it is believed that CXs should not normally exist at the configuration interaction singles (CIS) level when the ground state is a closed-shell singlet because the fact that the matrix elements between the ground and excited states are zero ( $H_{0,I} = 0$ ) is a consequence of Brillouin's theorem rather than a constraint that has to be enforced (Appendix 6.7.) Note that exceptions can occur in systems such as  $H_3$  when the ground state is not a closed-shell singlet. [In that case, the electron repulsion integrals which make the state energy difference different from the orbital energy difference vanish (Appendix 6.7.)]

Although Brillouin's theorem does not hold for DFT, there is something very similar in TDDFT. Excited states do not see the ground state surface because excited-state energies are generated by adding

TDDFT excitation energies to ground-state energies, so there are no matrix elements between the ground- and excited-states to zero out. This is the fundamental argument put forth in a recent article by Levine, Ko, Quenneville, and Martínez [102]. (Other articles from the Martínez group which discuss TDDFT with respect to excited state dynamics are Refs. [158–161].) They suggest that TDDFT should generally behave like CIS so that seams should be observed rather than CXs. This is backed up by an explicit calculation on H<sub>2</sub>O. Where surfaces do cross, the TDDFT surfaces showed a too rapid energy variation compared with CASSCF. In particular this too rapid variation is observed in the vicinity of the CX in H<sub>3</sub>. Thus, at first glance, TDDFT seems to be incapable of giving even a qualitatively correct description of conical intersections.

Since this contention seems to be in blatant contradiction with our finding that TDDFT/SH dynamics gives a qualitatively reasonable description of oxirane photochemistry, we decided to take a closer look at CXs in oxirane. Unfortunately we do not have a TDDFT algorithm for finding CXs. So, *faute de mieux*, we calculated TDDFT PESs in the CASSCF branching coordinates around the CASSCF CX. Our results and analysis are presented below.

### 6.5.1 Computational Details

GAUSSIAN03 [68] was used to search for the CX, to generate branching coordinates, and generate the points needed to plot the PESs. CASSCF calculations were carried out using an active space generated by 4 electrons distributed in 5 orbitals and the 6-311G\*\* basis set [162, 163]. Since the two states of interest have the same symmetry, our CASSCF(4,5) calculation was of the state-average type to prevent variational collapse with equal weights for  $S_0$  and  $S_1$ . At the CX between states  $I$  and  $J$ , the two branching coordinates, namely the derivative coupling (DC) vector,

$$h_q^{(I,J)} = \mathbf{C}_I^\dagger \frac{\partial H}{\partial q} \mathbf{C}_J, \quad (6.17)$$

and the unscaled gradient difference (UGD) vector,

$$g_q^{(I,J)} = \mathbf{C}_I^\dagger \frac{\partial H}{\partial q} \mathbf{C}_I - \mathbf{C}_J^\dagger \frac{\partial H}{\partial q} \mathbf{C}_J \quad (6.18)$$

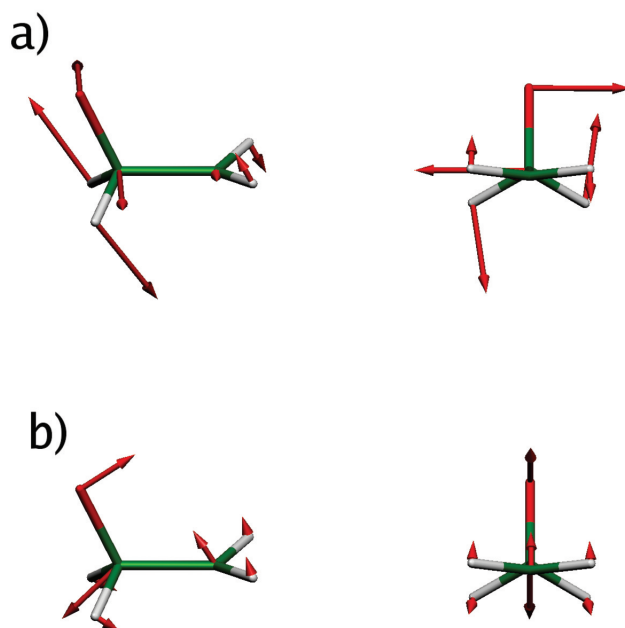


Figure 6.12:  $C_s$  symmetry CASSCF conical intersection structure. The DC vector (a) corresponds to a sort of twisting in opposing directions of the CO and the  $\text{CH}_2$  group to which it is joined. The UGD (b) vector corresponds to the opening of the CCO angle while maintaining  $C_s$  symmetry.

are computed. The grid used to plot the PES around the CX was generated from these vectors as

$$\mathbf{q} = m\mathbf{g} + n\mathbf{kh} , \quad (6.19)$$

where  $m$  and  $n$  vary from -5 to +5 in integer steps, and  $k$  is just a scaling factor that we set to 0.1 in order to assure smooth changes of the geometry.

CIS and TDPBE/TDA calculations are carried out using TURBOMOLE [78, 86] using the aug-cc-pVTZ basis [146, 147]. PESs were plotted using the same grid of geometries as in the CASSCF case.

### 6.5.2 Results

It is worth emphasizing that a CX is an  $(f - 2)$ -dimensional hyperpoint. In oxirane,  $f = 18$  so the CX is 16-dimensional. We found two qualitatively different CASSCF CX geometries and there are undoubtedly infinitely more. However we will focus on the  $C_s$ -symmetry structure shown in **Fig. 6.12** since this

is close to the geometry found in our TDDFT/SH calculations at the point of SH. **Figure 6.13** shows the CASSCF  $S_0$  and  $S_1$  PESs in the branching coordinates (Fig. 6.12) around this geometry. Degeneracy lifting occurs in both directions, confirming that this is indeed a CX. A selection of representative geometries is shown in **Figure 6.14**.

Mechanistically this CX structure should correspond to a resonance hybrid involving two types of resonance structures found in the literature for excited-state ring-opening reactions and shown as **2** in Fig. 6.1. The biradicaloid structure is typical for breaking a  $\sigma$  bond, while the zwitterion represents charge transfer. It might be thought that planarity of the CCH<sub>2</sub> group could be used as a criterion to judge which of these two structures is most important. According to elementary valence shell electron repulsion (VESPR) theory, the CCH<sub>2</sub> group should be planar in the zwitterion structure. The planarity of the CCH<sub>2</sub> group in the biradicaloid structure is less clear, however Herzberg and Shoosmith have shown experimentally that the  $\bullet\text{CH}_3$  radical is planar [164, 165] (this and additional evidence is reviewed in Ref. [166]). Thus the planarity of the CCH<sub>2</sub> group in the CX cannot be used to decide whether the biradicaloid or zwitterion structure is most important. Indeed there seem to be contributions of both in our CASSCF calculations.

Since biradicaloids are exactly the case where we expect to need explicit 2-electron excitations, we do not expect CIS to give a good description of this CX. Shown in Fig. 6.13 are the CIS  $S_0$  and  $S_1$  PESs calculated at the CASSCF geometries around the CX. As already discussed, the formal theory suggests that the best that we can hope to find is a hyperline rather than a hyperpoint. This is essentially what we see in the figure. That is, the surfaces remain essentially degenerate along the CASSCF UGD coordinate in the interval  $-10 \leq m \leq 0$ .

Since TDDFT is a formally exact theory, we do expect to get exact CXs from TDDFT when the exchange-correlation (xc) functional is exact. Furthermore, as discussed in Oxirane I, exact DFT is also expected to be able to describe the ground state of closed-shell singlets without symmetry breaking. In practice, of course, neither DFT nor TDDFT is exact because of the use of approximate xc energy functionals. Under these circumstances, symmetry breaking and the associated triplet instability (Oxirane I) is expected to occur in biradicaloids. Indeed a TDPBE instability is seen in Fig. 6.9 at around 104°. However its nature is fundamentally different than a normal triplet instability. To see what is meant by this, consider the two-orbital model for excitation from an unoccupied orbital  $i$  to an occupied orbital  $a$ .

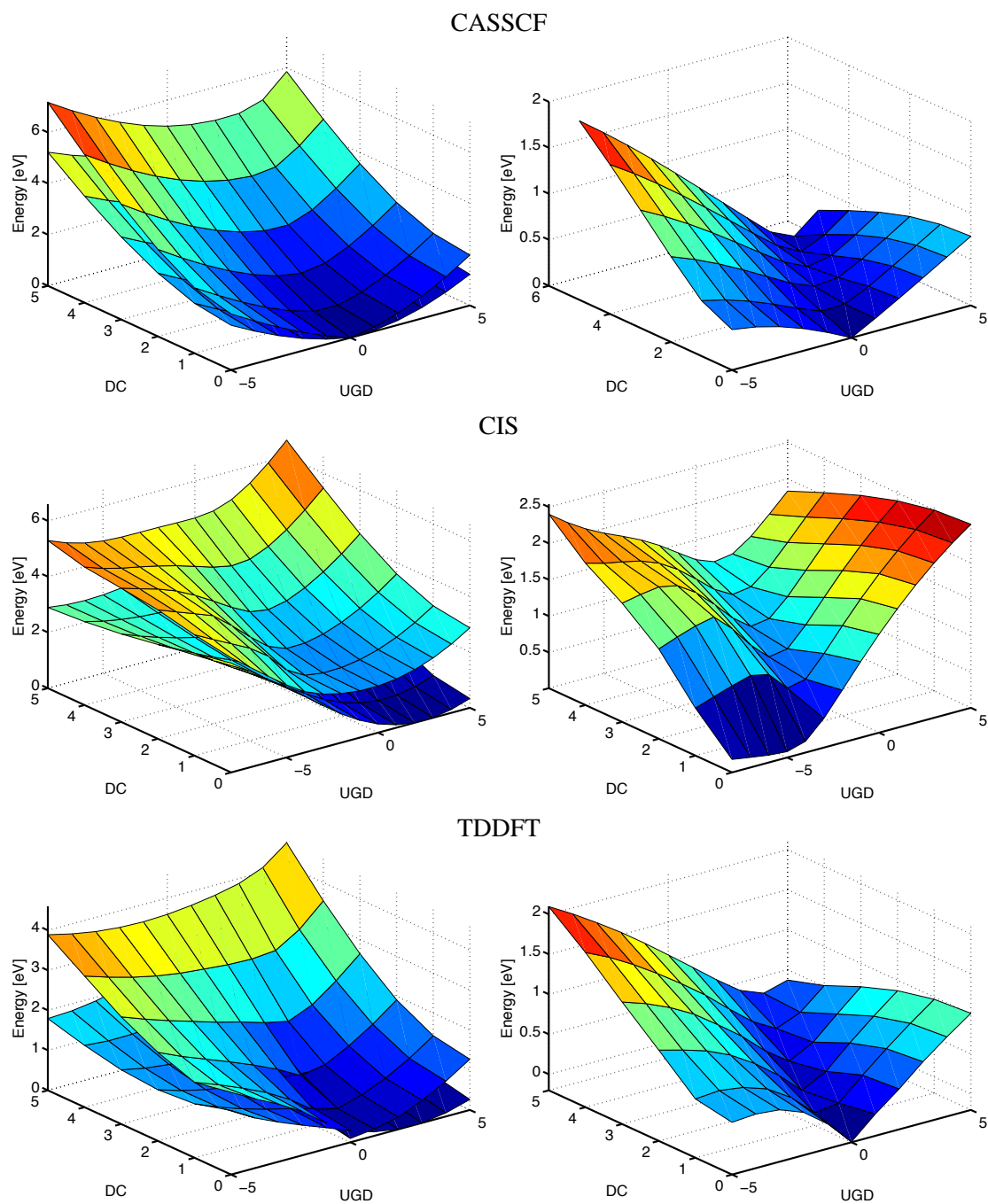


Figure 6.13: On the left hand side are shown the  $S_0$  and  $S_1$  PESs for each method computed as described in the text. On the right hand side are shown the corresponding energy difference,  $\omega(S_1) = E(S_1) - E(S_0)$ .



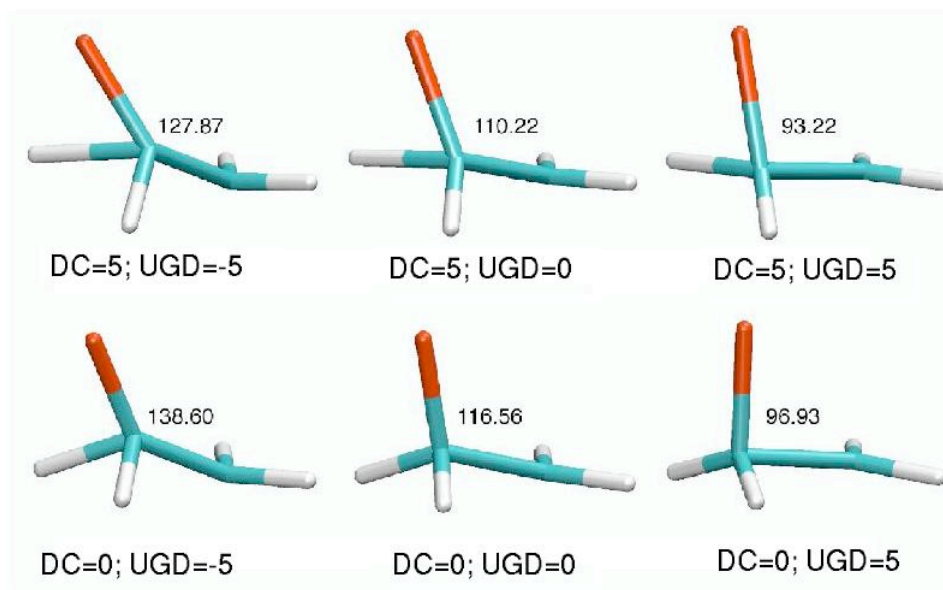


Figure 6.14: A selection of representative geometries and their CCO angles for the coordinates in Fig. 6.13. The  $C_s$  symmetry CASSCF conical intersection structure is at the origin.

The triplet and singlet excitation energies are, respectively,

$$\begin{aligned}
 \omega_T &= \sqrt{(\epsilon_a - \epsilon_i)[\epsilon_a - \epsilon_i + 2(ia|f_{xc}^{\uparrow,\uparrow} - f_{xc}^{\uparrow,\downarrow}|ai)]} \\
 \omega_S &= \sqrt{(\epsilon_a - \epsilon_i)[\epsilon_a - \epsilon_i + 2(ia|2f_H + f_{xc}^{\uparrow,\uparrow} + f_{xc}^{\uparrow,\downarrow}|ai)]}.
 \end{aligned}
 \tag{6.20}$$

In a normal triplet instability,  $\omega_T$  goes to zero and then becomes imaginary because the term in square brackets goes to zero and then becomes negative. Instead for triplet instabilities in the neighborhood of a conical intersection, the orbital energy difference goes to zero and then becomes negative, so that  $\omega_S$  and  $\omega_T$  go to zero at the same time.

The original Kohn-Sham formulation of density functional theory [45] assumed  $v$ -representability. That is, it was assumed that the ground density of the interacting system was also the ground state density of the noninteracting system. This means that the *Aufbau* principle holds and the LUMO energy should never fall below the HOMO energy or, in the language of solid-state physics, there should be no holes below the Fermi level. However holes below the Fermi level often happen in practice in DFT when orbitals are quasidegenerate. One way to understand this is that self-interaction errors in

approximate xc functionals are larger for occupied than for unoccupied orbitals. Thus the occupied member of the quasidegenerate orbitals is destabilized with respect to the unoccupied member and any attempt to change the orbital occupation leads to a reversal of the orbital energy ordering, with the result that the HOMO always remains higher in energy than the LUMO. A closely-related argument involves beginning with empty degenerate orbitals and then making a differential increase in the orbital occupancy. Since

$$\frac{\partial \epsilon_r}{\partial n_r} = (rr|f_H + f_{xc}^{\uparrow,\uparrow}|rr) \quad (6.21)$$

is expected to be dominated by the positive Hartree kernel,  $f_H$ , rather than the typically negative but smaller in magnitude xc kernel,  $f_{xc}$ , the orbital energy will increase as it becomes increasingly occupied, raising the energy of the occupied orbital above the energy of the unoccupied orbitals in the formerly degenerate set. The constrained search formulation of density functional theory allows holes below the Fermi level [167–169]. Indeed holes below the Fermi level are expected for the exact xc functional [169, 170]. We do see holes below the Fermi level in our calculations around the CX in oxirane. They represent a practical problem because convergence failures come from the common Quantum Chemistry practice of enforcing *Aufbau* filling in DFT calculations. In practice convergence is accomplished in a natural manner in the dynamics calculations by a sort of “orbital-following trick” where the initial guess for the electronic structure problem at each geometry is taken from the converged solution to the electronic structure problem from the previous geometry.

The foregoing discussion suggests that TDDFT ( $S_0, S_1$ ) conical intersections should be largely determined by orbital conical intersections between the HOMO and the LUMO. A way around this in exact TDDFT is if the frequency dependence of the xc kernel allows,

$$\lim_{\omega \rightarrow \epsilon_a - \epsilon_i} (\epsilon_a - \epsilon_i) [\epsilon_a - \epsilon_i + 2(ia|f_{xc}^{\uparrow,\uparrow}(\omega) - f_{xc}^{\uparrow,\downarrow}(\omega)|ai)] \neq 0 \quad (6.22)$$

(see for example the form of the exact xc kernel proposed by Maitra [171, 172].) However, in practice, the HOMO-LUMO energy difference is definitely small in our calculations around the CX.

According to Fig. 6.9 the singlet excitation energy becomes imaginary when the HOMO and LUMO energies cross at an OCC angle of about  $104^\circ$ . The exact solution should have neither this singlet instability nor the associated triplet instability. Following the recommendation of Oxirane I, we compensate

for this deficiency in the approximate xc functional by making the TDA in our calculations. The resultant formula,

$$\omega_S = (\epsilon_a - \epsilon_i) + (ia|2f_H + f_{xc}^{\uparrow,\uparrow} + f_{xc}^{\uparrow,\downarrow}|ai), \quad (6.23)$$

relies on error cancellation. By definition the exact  $\omega_S$  is nonnegative. In practice,  $\omega_S$  could be negative because approximations have been made. However the 2-electron integral terms are typically net positive, so they will at least partly cancel the negative orbital energy difference associated with the hole below the Fermi level. Explicit calculations are needed to see if this is actually the case.

Figure 6.13 shows that the TDPBE TDA  $S_0$  and  $S_1$  PESs calculated at the CASSCF geometries around the CASSCF CX. There is a much more marked resemblance between the TDPBE TDA and the CASSCF PESs than between the CIS and CASSCF PESs. In fact, the main difference between the TDPBE TDA approximate CX and the CASSCF CX is that the CASSCF double cone becomes a slightly interpenetrating double cone in the TDPBE TDA. Nevertheless the main conclusions of Levine, Ko, Quenneville, and Martínez [102] are verified. The CASSCF CX has become a TDPBE TDA seam encircling the CASSCF CX and the TDPBE TDA PESs vary too rapidly around this seam compared to the CASSCF PESs. From a dynamics point of view, the most serious problem with the TDPBE TDA approximate CX is that a typical trajectory crosses between  $S_0$  and  $S_1$  twice, with the net result that little surface hopping will occur. To counter this we deliberately decided to stay on  $S_0$  after SH and not allow re hopping back to  $S_1$ . While this neglect of surface recrossing may lead to shorter photodynamics, it is necessary to counter problems due to the approximate nature of the TDDFT CX and is not expected to have a large impact on the overall photochemical pathways that we seek to study.

## 6.6 Conclusion

Over the past decade, TDDFT has become a method of choice for studying molecular excited states. It is natural to expect that this success should be extended to the study of photochemical processes and that there will be obstacles encountered which must be surmounted. One barrier to applications of TDDFT in photochemistry has simply been a lack of technology to search excited state minimum energy pathways, to find funnels, to carry out photodynamics calculations of femtosecond spectra, and to simulate photochemical reactions. Technology of this sort is now coming on-line and, as it does,

it will permit us to troubleshoot TDDFT for applications to real photochemical reactions, thus giving a better idea of where conventional TDDFT provides an adequate description of photochemistry and where some of the problems mentioned in the introduction (artificially low ionization threshold, underestimated charge transfer excitations, lack of explicit two-electron excitations) may be critical and so must be corrected.

Very recently mixed TDDFT/classical trajectory photodynamics calculations have become possible [120–122]. This technology has been applied here to assess the usefulness of TDDFT for describing the photochemistry of oxirane. It was argued in Oxirane I that TDDFT/TDA calculations could indeed give a qualitatively correct description of oxirane photochemistry, but that dynamics calculations were needed in order to obtain full confirmation of this claim. We have done this and found that mixed TDPBE TDA/classical trajectory SH photodynamics calculations confirm the main experimental results available for the photochemical ring opening of oxirane. In addition we obtain state-specific information not easily available from experiment, such as that the  $^1(n, 3p_z)$  state is significantly more reactive than the  $^1(n, 3s)$  state, leading us to expect that vibronic coupling is likely to be much more important for the  $^1(n, 3p_z)$  state than for the  $^1(n, 3s)$  state.

Of course, some of what we found was already anticipated in earlier nondynamical studies. Indeed Bonačić-Koutecký and Michl give oxirane potential energy curves obtained with limited configuration interaction and a minimal basis set for a postulated CO ring-opening pathway (Ref. [1] p. 409) which are qualitatively similar to Fig. 6.9. However it should be emphasized that we had no need to postulate a pathway. Indeed the dynamics explores several pathways and gives us an idea of which are the most important. We see that we are not limited to following minimum energy pathways and that several surface hops may be needed before products are finally reached.

Once determined, we compared the performance of different functionals along the physically most important pathway. We found that the asymptotically-corrected TDLDA/SAOP and TDLDA/LB94 calculations give a more realistic vertical absorption spectrum. However this advantage diminishes along the  $^1(n, 3p_z)$  CO ring-opening pathway when the  $S_1$  state falls below  $-\epsilon_{\text{HOMO}}$ . It is then seen that the TDPBE potential energy curves are quite superior to those produced with the asymptotically-correct TDLDA/SAOP or TDLDA/LB94 approaches when compared to accurate QMC potential energy curves. Remarkably the TDPBE potential energy curves also appear to be superior to TDPBE0 potential energy

curves below  $-\epsilon_{\text{HOMO}}$ . This leads us to describe our TDPBE/TDA calculations as semi-quantitative.

We then went on to explore the timely question of how conical intersections are treated in TDDFT. Since TDDFT is a formally exact theory we should be able to obtain conical intersections had we the exact exchange-correlation functional. In practice, the use of approximate functionals leads to additional complications. Some of these complications are due to the presence of nearly degenerate HOMO and LUMO energies in the vicinity of conical intersection, leading to spin instabilities associated with holes below the Fermi level. These are handled, following the recommendation of Oxirane I, through the use of the Tamm-Dancoff approximation. The resultant TDDFT TDA calculations appear to be able to give an approximate description of the CASSCF conical intersection found in this system, the main difference being that the two cones interpenetrate slightly rather than touching as they should.

This “small” error could potentially translate into a large error in surface hopping dynamics, because it increases the probability of recrossings from  $S_1$  to  $S_0$  and back to  $S_1$ . We have chosen to deal with this by simply forbidding surface hopping from  $S_0$ . Such an approximation may lead to errors in rate constants but calculations using this approximation still provide useful information about likely reaction pathways.

As it stands, the success of the method for oxirane suggests that it could be used to study the photochemistry of similar systems. One example would be to add substituents which could stabilize the formation of carbonyl ylides since this is expected to favor CC ring-opening and (perhaps) lead to a Woodward-Hoffmann photomechanism (Appendix B of Oxirane I).

As it stands much of the interaction between the  $S_0$  and  $S_1$  surfaces at the conical intersection is happening at the orbital level. It would be interesting to introduce explicit configuration mixing between  $S_0$  and  $S_1$  in TDDFT in order to improve the TDDFT intersection topologies and  $(S_0, S_1)$  surface hopping rate calculations as well. The polarization propagator correction [101, 173, 174] and the spin-flip [175–178] approaches are promising routes in this direction.

## 6.7 Noncrossing Rule

Following Yarkony [179], we consider solving the problem

$$\mathbf{HC} = \mathbf{EC}, \quad (6.24)$$

where  $\mathbf{H}$  is a real matrix with spectral decomposition

$$H_{p,q}(\mathbf{R}) = \sum_r U_{p,r}(\mathbf{R}) E_r(\mathbf{R}) U_{r,q}^\dagger(\mathbf{R}), \quad (6.25)$$

where  $\mathbf{U}$  is a real orthogonal matrix. Here  $\mathbf{R}$  is the matrix of all nuclear degrees of freedom. At this point, Eq. (6.24) could be an eigenvalue problem for finding orbital energies, or it could be a configuration interaction (CI) problem for finding state energies. In the former case, we are studying orbital energy surfaces while, in the latter case, we are studying state energy surfaces.

The argument for a conical intersection (CX) is summarized here. The argument hinges on a calculation of the number of independent degrees of freedom in  $\mathbf{H}$  which is the number of independent degrees of freedom in  $\mathbf{U}$  plus the number of independent degrees of freedom in the set of  $E_r$ . Let  $N$  be the dimensionality of  $\mathbf{U}$ . Then  $\mathbf{U}$  has  $N \times N$  matrix elements. However

$$\mathbf{U}^\dagger \mathbf{U} = \mathbf{1} \quad (6.26)$$

means that there are  $N(N-1)/2$  orthogonality conditions to be satisfied on the columns of  $\mathbf{U}$  plus  $N$  normalization conditions. Thus  $\mathbf{U}$  really has

$$p_U(N) = N^2 - [N(N-1)/2 + N] = N(N-1)/2 \quad (6.27)$$

independent parameters.

Now suppose that one of the energy values is degenerate with value  $\tilde{E}$ . For generality let it be  $m$ -times degenerate. Without loss of generality we can reorder the energies so that

$$E_1 = E_2 = \dots = E_m = \tilde{E}. \quad (6.28)$$

Then we have the additional constraint that

$$\sum_{r=1,m} U_{p,r}(\mathbf{R}) E_r(\mathbf{R}) U_{r,q}^\dagger(\mathbf{R}) = \tilde{E} \delta_{p,q} \quad (6.29)$$

for  $p$  and  $q$  between 1 and  $m$ . That is,

$$\sum_{r=1,m} U_{p,r}(\mathbf{R})U_{r,q}^\dagger(\mathbf{R}) = \delta_{p,q} \quad (6.30)$$

which fixes

$$r_U(m) = m(m-1)/2 \quad (6.31)$$

parameters. At the same time, there are

$$d(N, m) = N - m + 1 \quad (6.32)$$

independent values of the  $E_r$  for  $r = 1, 2, \dots, m$ . This allows us to conclude that the final number of independent parameters in  $\mathbf{H}$  is

$$\begin{aligned} p_H(N, m) &= p_U(N) - p_U(m) + d(N, m) \\ &= N(N-1)/2 - m(m-1)/2 + N - m + 1. \end{aligned} \quad (6.33)$$

Finally we consider the case that two surfaces touch to make a CX. At the CX the number of free parameters is decreased from  $p_H(N, 1)$  (no degeneracy) to  $p_H(N, 2)$  (two surfaces touching). That is there is a reduction of

$$\Delta p_H = p_H(N, 1) - p_H(N, 2) = 2 \quad (6.34)$$

degrees of freedom (DOF). The conclusion is that 2 of the  $f$  internal DOF of a molecule must be fixed at a conical intersection. Hence that the conical intersection is of dimensionality  $f - 2$ . Actually, as emphasized in Ref. [179], it is not that the dimensionality of the conical intersection *must* be  $f - 2$  but that it *may* be  $f - 2$ . It could equally well be locally  $f - 1$ , even if this is improbable.

In the independent particle picture, there are no repulsions between electrons and the state Hamiltonian separates into the sum of orbital Hamiltonians. As is well-known, the state energies are just sums

of orbital energies and the energy difference between the ground and first excited states is just,

$$E_X - E_G = \epsilon_L - \epsilon_H, \quad (6.35)$$

where  $\epsilon_L$  is the LUMO energy and  $\epsilon_H$  is the HOMO energy. In this case, there is a clear one-to-one correspondence between the orbital and state CXs.

In contrast, full CI is invariant to a unitary transformation of the underlying orbitals. So state energy CXs are independent of orbital CXs.

In truncated CI, orbital and state CXs will be different because of the presence of orbital repulsion terms. For example, the CIS singlet-singlet excitation energy in a 2-orbital model is,

$$E_X - E_G = \epsilon_L - \epsilon_H + 2(HL|f_H|LH) - (HH|f_H|LL). \quad (6.36)$$

Usually

$$2(HL|f_H|LH) - (HH|f_H|LL) \neq 0 \quad (6.37)$$

when

$$\epsilon_L - \epsilon_H = 0. \quad (6.38)$$

This means that it usually suffices to focus on the CI matrix when discussing CXs.

Let us examine how the DOF argument changes in the CIS case. (This is quite analogous to what happens in the TDDFT/TDA method when employing the TDDFT adiabatic approximation.) We consider the equation

$$\mathbf{A}\mathbf{c} = \omega\mathbf{c} \quad (6.39)$$

where

$$\mathbf{A} = \mathbf{H} - E_0\mathbf{1} \quad (6.40)$$

and

$$\omega = E - E_0 \quad (6.41)$$

is a vertical excitation energy (which depends upon  $\mathbf{R}$ ). (Alternatively  $E_0$  is the HF ground state energy and the singly excited states are decoupled from the ground state by Brillouin's theorem.) Let us repeat



the above argument.  $\mathbf{A}$  is the  $N \times N$  matrix. We have that

$$p_A(N) = N^2 - [N(N-1)/2 + N] = N(N-1)/2. \quad (6.42)$$

Similarly if the ground state is  $m$ -fold degenerate, then without loss of generality

$$\omega_1 = \omega_2 = \dots = \omega_{m-1} = 0. \quad (6.43)$$

Note that  $m$  is the same as before, but  $m$  degenerate states correspond to  $(m-1)$  null excitation energies.

Then

$$r_U = (m-1)(m-2)/2 \text{ for } m > 0 \quad (6.44)$$

[which is different from Eq. (6.31)] and

$$r_U = 0 \text{ for } m = 0. \quad (6.45)$$

Also

$$d = N - (m-1) = N - m + 1 \quad (6.46)$$

[same as Eq. 6.32]. Calculating

$$\Delta p_A = p_A(N, 1) - p_A(N, 2) = -1 + 2 = 1. \quad (6.47)$$

Thus the ‘‘CIS noncrossing rule’’ is that the intersection with the ground state is of dimensionality  $f - 1$ .

Intersections between other states are of dimensionality  $f - 2$ .

## 6.8 Supplementary Material

Table 6.3 gives DMC energies calculated at the trajectory geometries given in Table 6.4.

We like to acknowledge useful discussions with Prof. Todd Martınez, Prof. Melvyn Levy, Prof. Massimo Olivucci, Dr. Felipe Cordova, and M. Mathieu Maurin. CF acknowledges the support by the *Stichting Nationale Computerfaciliteiten* (NCF-NWO) for the use of the SARA supercomputer facilities.

Table 6.3: Diffusion Monte Carlo energies.

Time Step	DMC Energy (a.u.)		
	$S_0$	$S_1$	$S_2$
1	-29.76593 (0.00059)	-29.48839 (0.00056)	-29.48847 (0.00057)
11	-29.76599 (0.00061)	-29.49390 (0.00056)	-29.49372 (0.00056)
21	-29.76023 (0.00059)	-29.50356 (0.00057)	-29.49707 (0.00057)
31	-29.74554 (0.00057)	-29.51447 (0.00060)	-29.49012 (0.00055)
41	-29.72426 (0.00062)	-29.53004 (0.00059)	-29.47881 (0.00056)
51	-29.69927 (0.00058)	-29.55456 (0.00056)	-29.49184 (0.00056)
61	-29.67125 (0.00059)	-29.57476 (0.00058)	-29.51883 (0.00055)
71	-29.64413 (0.00058)	-29.59381 (0.00058)	-29.53351 (0.00054)
81	-29.62603 (0.00061)	-29.60140 (0.00057)	-29.53029 (0.00063)
91	-29.61644 (0.00060)	-29.60962 (0.00057)	-29.52493 (0.00061)
101	-29.61977 (0.00058)	-29.61636 (0.00058)	-29.51733 (0.00061)
111	-29.63379 (0.00059)	-29.63012 (0.00063)	-29.52561 (0.00062)

Dr. Latévi Max Lawson Daku is thanked for supplying us with equilibrium geometry HOMO energies calculated with ADF and the LB94 and SAOP model exchange-correlation potentials.

Table 6.4: Diffusion Monte Carlo Geometries (Å)

Atom	$x$	$y$	$z$	$x$	$y$	$z$
	Time Step 1			Time Step 11		
C	5.716001	4.697350	4.740253	5.708642	4.696365	4.707034
C	4.268542	4.861866	4.685193	4.268986	4.866002	4.689871
O	5.059958	5.579439	5.659261	5.068887	5.581291	5.675816
H	6.394873	5.254909	4.017759	6.320931	5.248272	4.026430
H	3.570817	4.074812	5.061361	3.596577	4.054059	5.108103
H	6.124220	3.800314	5.142590	6.113518	3.774548	5.164374
H	3.899536	5.530933	3.922691	3.894545	5.561504	3.968278
	Time Step 21			Time Step 31		
C	5.700583	4.685666	4.670625	5.690324	4.662562	4.633233
C	4.266822	4.860386	4.690563	4.265988	4.853880	4.684585
O	5.078555	5.590114	5.701835	5.087869	5.605949	5.737091
H	6.273994	5.268379	4.025658	6.286331	5.335100	3.983653
H	3.658380	4.097412	5.141776	3.695577	4.140119	5.193340
H	6.105241	3.785173	5.189659	6.097250	3.839300	5.202626
H	3.856671	5.619638	4.010125	3.805925	5.669373	4.071584
	Time Step 41			Time Step 51		
C	5.682108	4.634714	4.584719	5.679835	4.602380	4.516071
C	4.269528	4.853639	4.673970	4.276690	4.856568	4.670861
O	5.094616	5.629287	5.781131	5.095162	5.660574	5.834160
H	6.299899	5.383928	3.965025	6.281852	5.380354	3.998633
H	3.673699	4.140254	5.277198	3.645922	4.152668	5.338324
H	6.111188	3.885028	5.220410	6.150170	3.904335	5.250797
H	3.760295	5.681397	4.155538	3.714459	5.669340	4.230430
	Time Step 61			Time Step 71		
C	5.683447	4.559336	4.432946	5.687818	4.498389	4.338152
C	4.287814	4.861139	4.685588	4.307673	4.874285	4.721692
O	5.087170	5.697589	5.893759	5.068676	5.741067	5.960793
H	6.259261	5.354725	4.044249	6.279360	5.369187	4.046432
H	3.654298	4.205548	5.336103	3.683374	4.256475	5.299296
H	6.182328	3.934450	5.247271	6.188564	3.982099	5.170132
H	3.661860	5.656398	4.268716	3.624044	5.636436	4.269583
	Time Step 81			Time Step 91		
C	5.688775	4.448742	4.261492	5.685935	4.406500	4.179016
C	4.333290	4.897132	4.760726	4.370446	4.931787	4.812912
O	5.046809	5.775195	6.012390	5.016058	5.808376	6.062579
H	6.305775	5.382080	4.007553	6.303708	5.335130	3.927621
H	3.679632	4.233752	5.300341	3.671551	4.169233	5.324153
H	6.191412	3.989886	5.081320	6.223290	3.924308	4.998596
H	3.634741	5.606361	4.252052	3.689336	5.569068	4.226539
	Time Step 101			Time Step 111		
C	5.679266	4.378646	4.107975	5.668014	4.357301	4.058374
C	4.413671	4.967544	4.875595	4.462932	5.000061	4.944148
O	4.979064	5.834592	6.102529	4.937273	5.852877	6.131409
H	6.275147	5.229236	3.799600	6.261575	5.125170	3.598018
H	3.716003	4.143069	5.330510	3.815039	4.179305	5.319001
H	6.268247	3.797387	4.898832	6.286471	3.657429	4.730906
H	3.763102	5.549321	4.204402	3.840754	5.560831	4.202227



## Chapter 7

# CC2 and TDDFT Studies of a Fluorescent Donor-Bridge-Acceptor Molecule

### Abstract

The photophysical properties of a donor-bridge-acceptor molecule (N-phenylpiperindone-malondinitrile) are investigated by second-order approximate coupled cluster (CC2) and time-dependent density functional theory (TDDFT). We report vertical excitation and fluorescence energies, calculated by taking energies from ground and excited state optimized geometries. CC2 is able to reproduce accurately the experimental results for both vertical excitations (within 0.3 eV) and fluorescence (within 0.1-0.6 eV). On the other hand, charge transfer (CT) excitations and fluorescence energies are strongly underestimated by TDDFT using the pure PBE functional but improved agreement is found for the hybrid functional PBE0. CC2 and DFT both predict accurate ground state geometries. Equilibrium geometries for the fluorescent state are qualitatively different between CC2 and TDDFT. CC2 predicts a bent exciplex geometry while TDDFT predicts a linear one. CC2 locates a minimum of the locally excited intradonor state. TDDFT fails to predict the equilibrium geometry of the intradonor state because of mixing between this state and an artificially low-lying CT state. This is an alarming example where the well documented CT failure of TDDFT affects properties of other localized states.

## 7.1 Introduction

The study of donor-bridge-acceptor (DBA) systems has a long history of serving as model systems in order to gain basic understanding of the elementary processes of photoinduced electron transfer (ET) in photosynthesis [180]. Nowadays, these types of systems are becoming attractive as possible building blocks for nano-optical devices in molecular electronics [181].

Covalently linked rod-shaped DBA systems [180] have been studied experimentally within the context of through-bond interactions [182, 183] (TBI). TBI refers to the interaction of electron donor and acceptor orbitals through mutual mixing with saturated  $\sigma$ -bonds that separate the two functional groups. It has been hypothesized and shown experimentally that TBI leads to structural distortions of DBA molecules compared to the molecular structures of the single donor, acceptor and bridge units [184]. In addition TBI leads to strong charge transfer (CT) absorption bands and excited states with large dipole moments [185].

In the present study we investigate, using different *first principle* methodologies, the geometric and optical properties of ground and excited states of a simple DBA molecule (DA1), as shown in Fig. 7.1. An N-phenyl unit serves as the electron donor and is separated from the dicyanoethylene electron accepting moiety by three saturated  $\sigma$ -bonds of the central piperidine unit. DBA molecules containing piperidine as a central unit were first synthesized and studied experimentally by Verhoeven and co-workers [184–189]. ET in DBA chromophores can proceed by two phenomenological different pathways, namely optical ET and photoinduced ET. In optical ET the transfer of an electron proceeds directly by excitation while in photoinduced ET an excitation occurs firstly into a locally excited state that then couples via molecular rearrangements to the CT state. DA1 is characterized by a strong CT absorption and a high fluorescence quantum yield. It has been found that excitation at different wavelengths all lead to a single fluorescence band, belonging to the lowest CT state [185]. This indicates that both pathways, optical and photoinduced ET might be important in the photophysics of this system. To investigate the importance of the different decay pathways, and to explain the strong fluorescence, we characterize the lowest excited states and their equilibrium geometries. Furthermore, we try to gain information about the geometric changes associated with interconversion from locally excited states into the fluorescence CT state.

Recently *first principles* excited-state electronic-structure methods have been used to complement

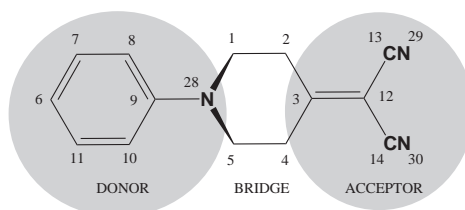


Figure 7.1: N-Phenylpiperidone-malondinitrile, which serves as the DBA model in the present study. The definition of donor (D), bridge (B) and acceptor (A) used in the analysis as well as the atomic numbering are indicated.

experimental studies of donor-acceptor systems. In particular theory has assisted in the rational design of molecules to gain desired properties [190–198]. Within this context, our aim is not only to investigate the photophysics of this particular system but also to probe the quality of the different excited-state methodologies for the description of this class of systems.

Coupled cluster (CC) methods [33] provide size-extensive descriptions of excited-state properties of molecular systems at a lower cost than CI methods. Among CC methods, second-order approximate CC singles-and-doubles [34] (CC2) offers a good compromise between accuracy and computational efficiency. CC2 is an approximation to coupled cluster singles and doubles (CCSD) but exhibits an  $N^5$  scaling with the number of orbitals rather than the  $N^6$  scaling of CCSD. In addition, excitation energies can be obtained by a linear response treatment of the CC2 reference state. Excitation energies using CC2 have been shown to be within 0.3 eV from experimental measurements [199, 200]. CC2 has been recently applied to study photophysical processes in a range of different systems [201, 202].

Further reduction of computational cost can be obtained by using time-dependent density functional theory (TDDFT) [19, 20, 39]. This method has been successfully applied to study photochemistry and photophysics in different systems [21, 43, 49, 203–205]. Unfortunately TDDFT has some severe drawbacks related to the approximate nature of the exchange-correlation (xc) kernel, which still restricts its general usage for a large variety of systems [206]. One of the major problems of TDDFT for describing extended systems is related to the well known underestimation of long-range CT excitations [83]. However, in some cases sufficient overlap between donor and acceptor orbitals can lead to a reasonable description of CT states [207–210], especially when hybrid functionals are used. In light of this, we explore the quality of TDDFT for the CT states occurring in our particular system, in addition we probe to what extent the CT failure affects the description of locally excited states.

## 7.2 Computational Details

All calculations presented here were carried out with the TURBOMOLE [78] program package. Geometry optimizations in the ground state were carried out using CC2 and DFT. The excited state geometries were obtained using linear response CC2 and linear response TDDFT. All geometry optimizations employ the TZVP [79] basis set and we use the default convergence criteria for Cartesian gradients ( $10^{-3}$  a.u.) and total energies ( $10^{-6}$  a.u.). Improved excitation energies and excited state properties were obtained by single point calculations using the augmented aug-cc-pVDZ [211] basis set for both, CC2 and TDDFT. Excitation energies were computed at linear response CC2 [34] level and by linear response TDDFT [20], using the the Tamm-Dancoff (TDA) [48] approximation. In the notation used in the following we do not make the distinction between CC2 and linear response CC2. Furthermore, the abbreviation TDDFT stands for linear response TDDFT using the TDA.

The CC2 module of TURBOMOLE [199, 200, 212, 213] makes use of the frozen core approximation. In our calculations the 17 lowest molecular orbitals were kept frozen. In addition the Coulomb repulsion is approximated by the resolution of identity (RI) method, was originally implemented for MP2 [214]. Therefore optimized auxiliary basis sets for SVP, TZVP [79] and aug-cc-pVDZ [215] basis sets were used.

DFT and TDDFT implementations of TURBOMOLE are described elsewhere [86, 216, 217]. Calculations employ the PBE [66] xc-functional and its hybrid version PBE0, in which 25% of PBE exchange is replaced by exact (Hartree-Fock) exchange. Corresponding TDDFT calculations are denoted by TDPBE and TDPBE0 in the following.

## 7.3 Results

### 7.3.1 Ground State Geometries

Selected bond distances, bond angles and dihedral angles of the ground state equilibrium structure of DA1 optimized with CC2, DFT/PBE, and DFT/PBE0 are reported in Tables 7.1 and 7.2. The full Cartesian coordinates can be found in Table 7.11 of the appendix. Fig. 7.2 shows the computed structures together with the experimentally derived crystal structure (X-ray), all aligned to the donor moiety plus the C5 atom of the bridge unit (D+C5). From this alignment it can be seen that all methods agree well in



the local description of the donor, bridge and acceptor units. This is evident by the low root mean square deviation (RMSD) ( $< 0.07 \text{ \AA}$ ) from the crystal structure (Table 7.3). In contrast the relative orientation between the single units exhibit larger deviations as evidenced by the somewhat larger overall RMSD.

The most significant deviation between the crystal structure and the theoretically computed structures concerns the description of the N28-C9 twist angle, defining the orientation of the phenyl ring to the piperidine moiety (C8-C9-N28-C1 and C10-C9-N28-C5 in Table 7.2). From the comparison of the Newman projections along the N28-C9 bond (Fig. 7.3), it can be seen, that all theoretical methods predict a rather asymmetric conformation, in contrast to the crystal structure that nearly conserves a symmetry plane perpendicular to the plane of the phenyl ring. This is also reflected by a larger RMSDs ( $\approx 0.2 \text{ \AA}$ ) for the donor moiety plus atoms C1 and C5 (D+C5+C1 in Table 7.3) compared to the RMSDs of the single units D, B, A. It is possible that the inaccurate description of dispersion interactions in the DFT methods leads to a stronger twist, caused by repulsion between hydrogens of the donor and the bridge (hydrogen atoms connected to C8, C10, C1, and C5). However, the fact that all theoretical gas-phase structures predict this asymmetric conformation suggests that the more symmetric conformation of the crystal structure arises from packing effects. It may be suspected that crystal packing would affect more the relative orientation of the units, than the internal geometries of the units.

Regarding the pyramidalization angle at N28 (Table 7.4), it can be seen that DFT structures and the crystal structure exhibit a flatter conformation than the CC2 structure.

The same trend is found for the acceptor, where CC2 again predicts a slightly stronger pyramidalization of the C3 center (Table 7.6) than DFT and the experiment.

For the piperidine unit, the RMSD of about  $0.04 \text{ \AA}$  from the X-ray structure is equally good for all theoretical methods, and small deviations in the dihedral angles related to the chair conformation (Table 7.5) have negligible effects on the positions of the nuclei.

In summary, theoretical structures agree within  $0.18 \text{ \AA}$  with one another but they differ by about  $0.24\text{-}0.29 \text{ \AA}$  from the the crystal structure (Table 7.3). In contrast, if we consider the donor, bridge, and acceptor units on their own then an agreement of  $< 0.07 \text{ \AA}$  with the experiment is found.

Some geometric parameters have been found to be sensitive for TBI in DA1 [184]. To probe the influence of TBI on the geometry of the  $\sigma$ -relay of the bridge unit the geometry of N-phenylpiperidine (NPP) was optimized. NPP may be considered as a DA1 molecule but lacking the acceptor moiety,

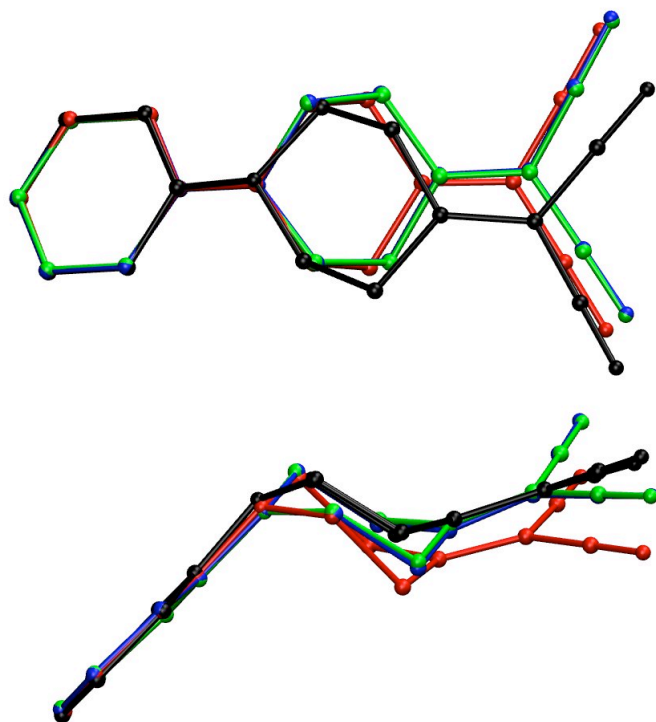


Figure 7.2: Superposition of the ground-state geometries, optimized by different methods and the crystal structure. All structures were aligned on the donor moiety plus C5. Red: CC2, blue: PBE, green: PBE0, and black: crystal structure.

so that distortions due to TBI should be absent. According to Ref. [184] the "central" C-C bonds of the bridge unit (C1-C2, C4-C5) are expected to be elongated if an interaction between the donor and acceptor is present. All theoretical methods used here predict longer "central" C-C bonds compared to the corresponding bonds in NPP (Table 7.1) and seem confirm the presence of TBI. With respect to the lengths of remaining C-C and C-N bonds of the  $\sigma$ -relay, CC2 and DFT both agree in the trend from NPP to DA1.

### 7.3.2 Vertical Absorption Energies

Using CC2, TDPBE and TDPBE0, we computed the lowest vertical singlet excitation energy from optimized ground state geometries. Results, employing the TZVP and aug-cc-pVDZ basis sets are summarized in Table 7.7.

The electronic transitions are interpreted in terms of single-particle transitions between the frontier orbitals of the given reference state. In the case of DFT these are the Kohn-Sham (KS) orbitals and for

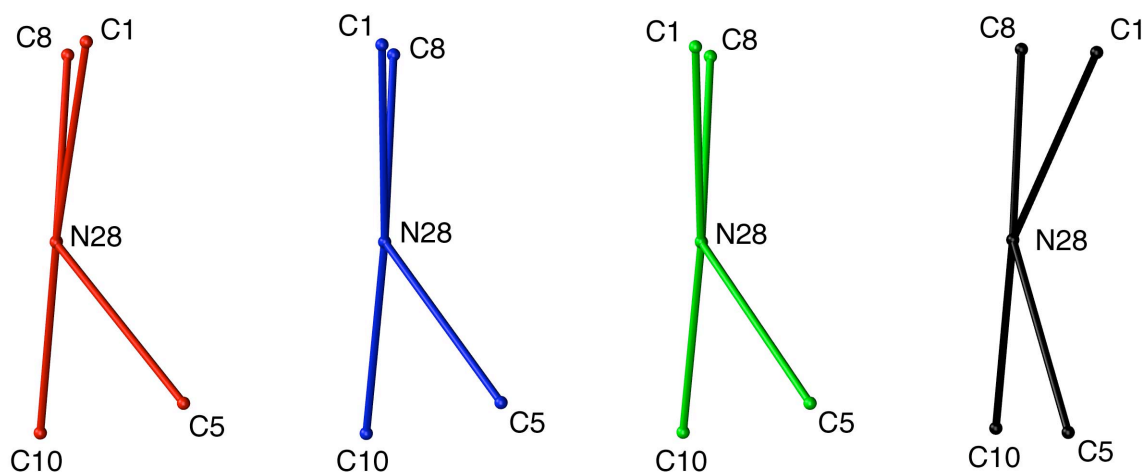


Figure 7.3: Newman projection along the N28-C9 bond. Red: CC2, blue: PBE, green: PBE0, and black: crystal structure.

	NPP			DA1							
	$S_0$			$S_0$				$S_1$			$S_2$
	PBE	PBE0	CC2	PBE	PBE0	CC2	X-ray	PBE	PBE0	CC2	CC2
C9-N28	1.398	1.391	1.406	1.410	1.400	1.414	1.412	1.346	1.337	1.379	1.391
N28-C1	1.459	1.449	1.463	1.450	1.441	1.453	1.461	1.494	1.474	1.475	1.455
N28-C5	1.463	1.453	1.467	1.455	1.444	1.459	1.495	1.495	1.474	1.475	1.458
C5-C4	1.539	1.528	1.528	1.565	1.547	1.550	1.546	1.521	1.516	1.539	1.546
C2-C1	1.536	1.526	1.530	1.564	1.546	1.552	1.542	1.520	1.515	1.534	1.544
C4-C3	1.534	1.525	1.530	1.492	1.487	1.491	1.494	1.513	1.494	1.497	1.495
C3-C2	1.535	1.525	1.530	1.493	1.488	1.491	1.495	1.513	1.495	1.497	1.495
C3-C12	-	-	-	1.374	1.357	1.365	1.347	1.438	1.423	1.446	1.362
C12-C14	-	-	-	1.429	1.428	1.430	1.438	1.410	1.405	1.406	1.431
C12-C13	-	-	-	1.430	1.427	1.430	1.436	1.410	1.405	1.406	1.431
C14-N30	-	-	-	1.168	1.153	1.182	1.141	1.176	1.162	1.194	1.182
C13-N30	-	-	-	1.167	1.153	1.182	1.139	1.176	1.162	1.194	1.182
C9-C10	1.417	1.406	1.411	1.412	1.404	1.409	1.395	1.442	1.432	1.415	1.432
C9-C8	1.415	1.403	1.411	1.411	1.401	1.408	1.399	1.442	1.433	1.416	1.418
C10-C11	1.393	1.383	1.392	1.392	1.383	1.391	1.387	1.378	1.369	1.386	1.435
C11-C6	1.399	1.389	1.396	1.398	1.389	1.396	1.373	1.407	1.397	1.399	1.405
C6-C7	1.396	1.386	1.393	1.396	1.385	1.392	1.372	1.407	1.397	1.400	1.415
C7-C8	1.396	1.387	1.395	1.397	1.388	1.396	1.386	1.378	1.369	1.386	1.436

Table 7.1: Selected bond lengths ( $\text{\AA}$ ) of the ground and excited state equilibrium geometries of DA1 and NPP, calculated by CC2 and DFT, and obtained from X-ray diffraction [184]. The numbering of the atoms refers to Fig. 7.2.

	NPP			DA1								
	$S_0$			$S_0$				$S_1$				$S_2$
	PBE	PBE0	CC2	PBE	PBE0	CC2	X-ray	PBE	PBE0	CC2	CC2	
C9-N28-C5	121.51	120.74	117.41	120.34	120.93	117.22	118.9	124.24	123.98	122.53	121.91	
C8-C9-N28	120.75	120.67	120.55	120.10	120.22	119.74	121.1	121.55	121.57	119.92	117.81	
C10-C9-N28	122.18	122.21	122.40	122.26	122.27	122.61	121.8	121.46	121.52	120.32	119.48	
C9-N28-C1	121.47	120.79	117.09	119.64	120.41	116.37	118.1	124.31	124.08	122.28	120.56	
C9-N28-C5	121.51	120.74	117.41	120.34	120.93	117.22	118.9	124.24	123.98	122.53	121.91	
N28-C1-C2	111.60	111.71	111.33	111.53	111.86	111.34	110.9	112.56	111.94	106.24	107.70	
N28-C5-C4	112.74	112.76	112.23	112.47	112.76	112.40	111.2	113.06	112.57	108.54	109.29	
C1-C2-C3	111.16	110.93	110.01	109.22	109.76	107.72	108.8	112.17	111.83	110.44	109.02	
C5-C4-C3	109.73	109.70	109.73	108.19	108.82	107.55	109.2	111.15	110.98	109.41	108.71	
C2-C3-C12	-	-	-	122.63	122.70	122.57	122.8	116.60	118.58	117.21	122.49	
C4-C3-C12	-	-	-	122.47	122.75	122.52	123.0	116.83	118.80	117.18	121.99	
C12-C14-N30	-	-	-	179.48	179.17	178.61	179.6	176.99	177.56	174.92	178.75	
C12-C13-N29	-	-	-	179.55	179.29	178.92	179.4	176.92	177.42	175.05	179.07	
C3-C12-C14	-	-	-	121.63	121.79	121.33	122.2	121.00	121.19	119.63	121.41	
C3-C12-C13	-	-	-	121.76	121.86	121.56	122.6	121.02	121.15	119.90	121.69	
C4-C3-C2	110.99	110.87	110.76	114.46	114.40	114.36	114.0	109.38	111.87	113.36	115.29	
C8-C9-N28-C1	36.82	39.11	37.24	41.35	39.74	43.53	23	-0.51	3.25	35.78	31.42	
C10-C9-N28-C5	7.12	4.59	-11.51	3.55	4.11	-5.38	22	14.44	12.03	12.74	6.83	
C2-C3-C12-C13	-	-	-	3.38	2.41	5.38	4	-24.56	-20.41	-23.35	3.87	
C4-C3-C12-C14	-	-	-	-3.85	-2.07	-4.33	4	25.15	20.96	22.95	-2.64	
C1-C2-C3-C4	-52.60	-52.74	-53.38	-53.56	-51.87	-55.74	53	-54.97	-52.78	-55.50	-53.34	
C5-C4-C3-C2	52.46	52.50	52.48	53.34	51.61	54.62	52	55.13	52.69	53.54	51.76	

Table 7.2: Selected bond angles and dihedral angles ( $^\circ$ ) of the ground and excited state equilibrium geometries of DA1 and NPP, calculated by CC2 and DFT, and obtained from X-ray diffraction [184]. The numbering of the atoms refers to Fig. 7.2.

	DA1	C9+N28+B+A	D	D+C1+C5	piperidine	A	A+C2+C4
CC2	0.293	0.159	0.038	0.178	0.041	0.068	0.094
PBE	0.251	0.124	0.035	0.195	0.038	0.056	0.082
PBE0	0.241	0.109	0.043	0.193	0.038	0.064	0.092

Table 7.3: RMSD ( $\text{\AA}$ ) of the heavy atoms between the DA1 crystal structure [184] and the ground state geometries optimized by different methods. The donor (D), bridge (B), and acceptor (A) moieties and the numbering of the atoms are defined in Fig. 7.2.

	DA1				NPP		
	PBE	PBE0	CC2	X-ray	PBE	PBE0	CC2
$S_0$	19.25	17.83	26.38	21.62	14.74	17.25	26.02
$S_1$	-7.70	-4.84	10.21	-	-	-	-
$S_2$	-	-	15.04	-	-	-	-

Table 7.4: N-pyramidalization angles ( $^\circ$ ) of ground ( $S_0$ ) and the first two excited state ( $S_1$ ,  $S_2$ ) geometries calculated by CC2 and DFT, and obtained from X-ray diffraction [184]. The average of the dihedrals C1-C5-C9-N28, C5-C9-C1-N28, and C9-C1-C5-N28 define the N-pyramidalization angle. Atoms numbers are defined in Fig. 7.2.

		DA1				NPP		
		PBE	PBE0	CC2	X-ray	PBE	PBE0	CC2
$S_0$	$\alpha$	52.20	51.94	53.83	51.85	51.40	51.75	54.42
	$\beta$	49.59	47.88	51.54	46.44	48.08	48.22	48.69
$S_1$	$\alpha$	48.11	49.26	58.78	-	-	-	-
	$\beta$	49.62	47.82	49.97	-	-	-	-
$S_2$	$\alpha$	-	-	58.76	-	-	-	-
	$\beta$	-	-	48.74	-	-	-	-

Table 7.5: Dihedral angles related to the chair conformation of the piperidine spacer for ground and excited state geometries of DA1 and NPP, calculated data and experimental values.  $\alpha$  is defined as the average of the dihedrals N28-C1-C5-C4 and N28-C5-C1-C2, and  $\beta$  as the average of dihedrals C3-C4-C3-C1 and C3-C2-C4-C5. Atoms numbers are defined in Fig. 7.2.

	PBE	PBE0	CC2	X-ray <sup>a</sup>
$S_0$	4.30	2.49	4.87	2.66
$S_1$	-26.68	-21.34	-22.70	-
$S_2$	-	-	3.14	-

Table 7.6: Calculated and experimental [184] values of the C3-pyramidalization angle ( $^\circ$ ) of ground ( $S_0$ ) and first two excited state ( $S_1$ ,  $S_2$ ) geometries of DA1. The C3-pyramidalization angle is defined as the average of the dihedrals C2-C12-C4-C3, C12-C4-C2-C3, and C4-C2-C12-C3.

CC2 these are the HF orbitals. In the case of PBE and PBE0, the usage of different basis sets does not affect the qualitative appearance (nodal structure, spatial extent) of the relevant orbitals. This is in stark contrast to HF, where the shape of the virtual orbitals changes when the basis set is augmented with diffuse functions. This leads to different sets of HF orbitals when TZVP and aug-cc-pVDZ are used (Fig. 7.4). PBE0, PBE and HF/TZVP orbitals agree qualitatively well, although their relative energetic ordering is slightly different. Therefore assignments calculated by TDPBE, TDPBE0, and CC2/TZVP are based on the same set of reference orbitals, as shown on the left of Fig. 7.4, while CC2/aug-cc-pVDZ assignments refer to the orbitals on the right of Fig. 7.4.

The CC2/aug-cc-pVDZ vertical absorption energies agree within 0.3 eV with the maxima of the experimental bands. We assign the first experimental band at 3.63 eV to the lowest charge transfer excitation ( $H \rightarrow L+6$ ) calculated at 3.685 eV, an assignment that is also supported by the fluorescence experiments of Hermant *et al.* [185]. The next band at 4.25 eV is assigned to an intradonor (ID)  $\pi-\pi^*$  ( $H \rightarrow L+14$ ) transition at 4.553 eV, typical for aniline derivatives [218]. According to CC2, the band at 4.99 eV can be caused either by another CT excitation ( $H \rightarrow L$ ) and/or by a Rydberg like transition

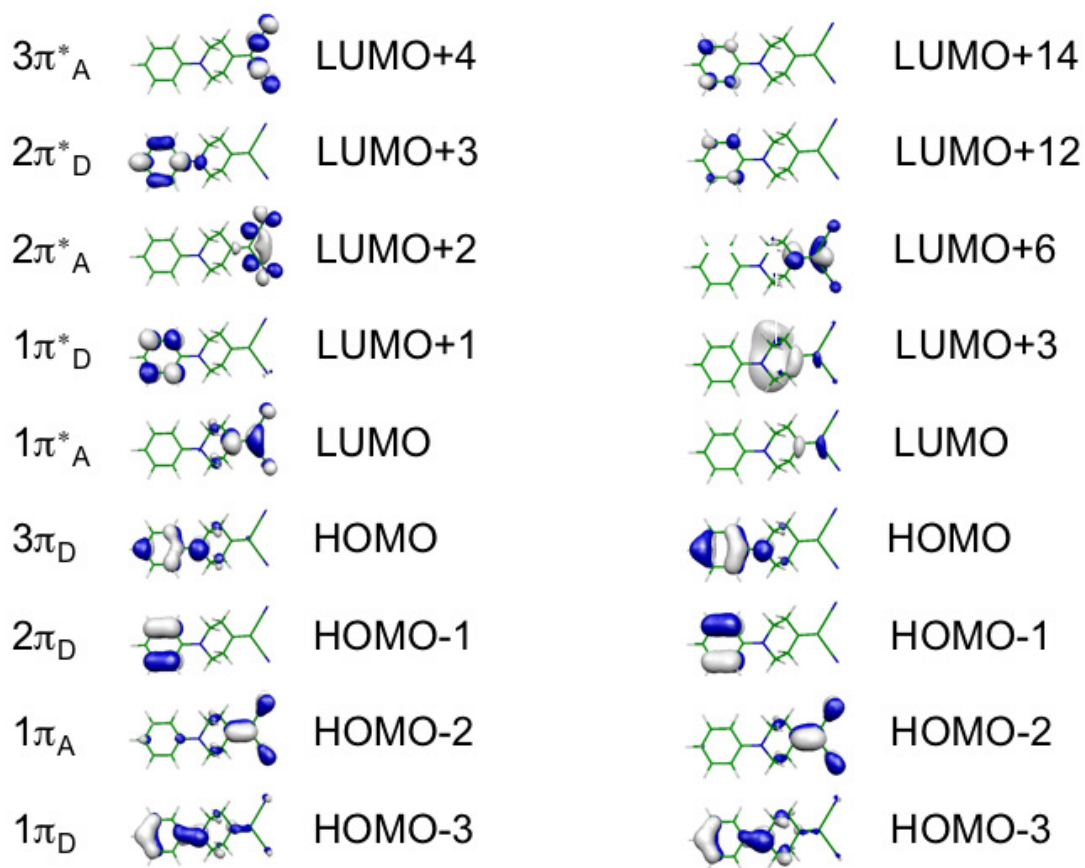


Figure 7.4: Left: PBE Kohn-Sham molecular orbitals obtained using the TZVP basis set. Right: Hartree-Fock molecular orbitals obtained using the aug-cc-pVDZ basis set. Assignments of TDDFT and CC2/TZVP transitions are qualitatively given on the basis of the KS orbitals on the left. CC2/aug-cc-pVDZ transitions are given on the basis of the HF/aug-cc-pVDZ orbitals on the right.

(H→L+3/L+2).

Comparing the excitation energies of the two CC2 calculations which differ only in the basis set used, it can be seen that  $S_1$  and  $S_2$  are predicted within 0.2 eV from the experimental value. However, the inclusion of diffuse basis functions shifts the energies of the next two higher states (4.857 and 5.026 eV in Table 7.7) down close to the experimental band at 4.99 eV. Therefore, the inclusion of diffuse basis functions is important for a balanced description of all excitation energies compared to the experiment. From a practical point of view, this fact complicates the description of the interconversion from  $S_2$  and  $S_3$  into the fluorescent  $S_1$  state, because CC2 geometry optimizations or molecular dynamics are computationally very demanding when augmented basis sets are used.

Turning to the TDDFT excitation energies, we see that TDPBE drastically underestimates the lowest CT excitation by more than 1.6 eV. In addition, there exists between  $S_1$  and the ID excitation at 4.1 eV two additional CT states that are absent in the CC2 description. Usage of the hybrid xc-functional PBE0 leads to a blueshift of all excitation energies. The blueshift is certainly larger for CT excitations, resulting in a smaller error for the first excitation energy compared to TDPBE. However, using TDPBE0/TZVP one finds an artificially low-lying CT state between  $S_1$  and the ID state. With TDPBE0/aug-cc-pVDZ this artificial CT state is shifted 0.1 eV above the ID state and mixes considerably with the ID state at 4.6 eV. This mixing also seems to affect excited state properties, for instance the excited state dipole moment of  $S_2$  predicted by TDPBE0 (11.683 Debye) is considerably larger than predicted by CC2 (2.283 Debye). As we will see later, the mixing between ID and CT states affects the nuclear forces and makes it impossible to obtain structural information of the ID state using TDPBE and TDPBE0.

In summary, it is CC2/aug-cc-pVDZ that reproduces best the experimental excitation energies. Both TDDFT approximations underestimate CT excitations. Considering the excitation energies, PBE0 differs on average by about 0.5 eV from the experiment. However, PBE0 predicts a strong mixing between the CT and ID states, in contrast such a mixing is not present in CC2. The influence of the basis set on the excitation energies appears to be stronger for CC2 than for TDDFT.

### 7.3.3 Geometries of the Excited Charge Transfer State and Fluorescence

In order to investigate structural rearrangements related to the electron transfer from donor to acceptor and to predict the fluorescence spectra, we optimize the geometry of DA1 in the lowest CT state. Ac-

$\omega$	assignment	$\mu$	$\omega$	assignment	$\mu$	$\omega$	assignment	$\mu$	$\omega$	Expt. <sup>b</sup>
2.206 (0.152)	$3\pi_D-1\pi_A^*$ CT	16.617	3.208 (0.168)	$3\pi_D-1\pi_A^*$ CT	19.170	3.780 (0.242)	$3\pi_D-1\pi_A^*$ CT	19.378	3.63 (0.118)	18.8
3.329 (0.001)	$2\pi_D-1\pi_A^*$ CT	24.058	4.646 (0.008)	$2\pi_D-1\pi_A^*$ CT	15.931	4.632 (0.020)	$3\pi_D-1\pi_D^*$ ID	2.476	4.25 (0.079)	
3.749 (0.012)	$3\pi_D-2\pi_A^*$ CT	23.162	4.805 (0.026)	$3\pi_D-1\pi_D^*$ ID	11.417	5.391 (0.333)	$3\pi_D-2\pi_D^*$ ID	2.605	4.99 (1.000)	
4.129 (0.022)	$3\pi_D-1\pi_D^*$ ID	0.778	5.298 (0.155)	$3\pi_D-2\pi_D^*$ ID	18.868	5.985 (0.008)	$2\pi_D-1\pi_A^*$ CT	25.505		
4.264 (0.121)	$1\pi_D-1\pi_A^*$ CT	19.199	5.365 (0.392)	$1\pi_A-1\pi_A^*$ IA	13.328	6.011 (0.391)	$1\pi_D-1\pi_A^*$ ID	9.333		
PBE/aug-cc-pVDZ			PBE0/aug-cc-pVDZ			CC2/aug-cc-pVDZ				
2.199 (0.150)	$3\pi_D-1\pi_A^*$ CT	16.604	3.196 (0.046)	$3\pi_D-1\pi_A^*$ CT	19.022	3.685 (0.236)	55% HL+6 8% H-3L+6 8% HL CT	19.070		
3.336 (0.009)	$2\pi_D-1\pi_A^*$ CT	23.947	4.614 (0.008)	51% $3\pi_D-1\pi_D^*$ 43% $2\pi_D-1\pi_A^*$ ID/CT	11.683	4.553 (0.022)	46% HL+14 9% HL+12 7% HL+13 ID	2.283		
3.749 (0.012)	$3\pi_D-2\pi_A^*$ CT	23.211	4.764 (0.010)	56% $2\pi_D-1\pi_A^*$ 37% $3\pi_D-1\pi_D^*$ CT/ID	15.317	4.857 (0.051)	64% HL 5% H-3L+6 5% HL+6 CT	5.588		
4.071 (0.022)	$3\pi_D-1\pi_D^*$ ID	0.8250	4.980 (0.081)	$3\pi_D-2\pi_D^*$ ID	7.258	5.026 (0.072)	20% LL+3 15% HL+2 11% HL+12 Rydberg	5.656		
4.249 (0.012)	56% $1\pi_D-1\pi_A^*$ 33% $2\pi_D-1\pi_A^*$ ID/CT	9.669	5.224 (0.133)	55% $3\pi_D-2\pi_A^*$ 9% $3\pi_D-2\pi_D^*$ CT/ID	6.633					

Table 7.7: Lowest lying singlet excitation energies  $\omega$  (eV) of DA1 and excited state dipole moments  $\mu$  (Debye). Oscillator strengths (length representation) and normalized extinction coefficients for the experiment are given in parenthesis. For all methods, except CC2/aug-cc-pVDZ, the main orbital contribution is qualitatively given by means of molecular orbitals obtained by PBE/TZVP (Fig. 7.4). Assignments of the CC2/aug-cc-pVDZ transitions are given on the basis of HF/aug-cc-pVDZ molecular orbitals. For transitions whose main contribution is below 65% also the second (and third) contributions are given. According to the location of the orbitals the excitations were labeled as charge transfer (CT), intradonor (ID) or intra acceptor (IA) excitations.<sup>b</sup> The experimental value measured in n-hexane is taken from Ref. [185].



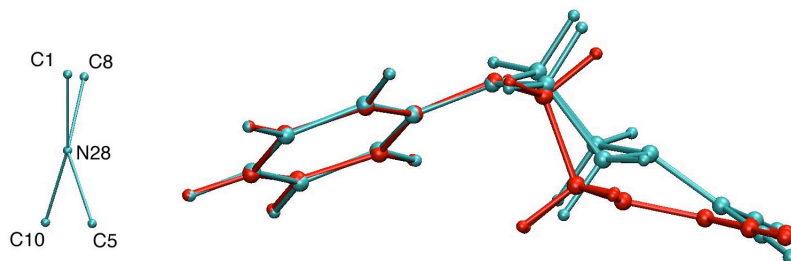


Figure 7.5: Comparison of the  $S_0$  and  $S_1$  geometries. Left: Newman projection along the N28-C9 bond of the CC2 structure optimized in  $S_1$ . Right: CC2 optimized geometries of  $S_0$  (red) and of  $S_1$  (cyan), aligned on the donor.

According to Hermant *et al.* [185] it is this state from which the experimentally measured fluorescence is emitted. Cartesian coordinates of the  $S_1$  optimized structures computed by CC2, TDPBE, and TDBPE0 are summarized in Table 7.5 in the appendix.

Comparing the CC2 ground state geometry with that of  $S_1$  (Fig. 7.5), we recognize that the major rearrangements result from a strong pyramidalization of the C3 atom of the acceptor moiety (Table 7.6). Simultaneously we observe a flattening of the pyramidalization of the donor nitrogen (Table 7.4), while the piperidine spacer changes very little (Table 7.5). These structural changes lead to a bending of the entire molecule. This geometric rearrangement resembles Coulombic-induced folding ("harpooning"), which has been observed in DBA systems possessing more flexible bridging units [219]. In addition, we observe a change of the sign N28-C9 twist angle (Fig. 7.5) compared to the ground state geometry (Fig. 7.3).

The optimized structures of the lowest CT state computed by TDDFT are qualitatively different from the corresponding CC2 structure (Fig. 7.6) as they do not exhibit the same bending of the molecule at N28. TDDFT assumes structures that are even more linear, due to a flat and only slightly inverted conformation of the N28 pyramidalization (Table 7.4). Similar to CC2 we also observe an increase of the N28-C9 twist angle and a similar C3-pyramidalization of the ethylene moiety.

With respect to the N28-C9 twist angle and the C3-pyramidalization TDPBE, TDPBE0 and CC2 are qualitatively similar, but the global structure of the molecule appears to be very different because of the different description of the pyramidalization at N28.

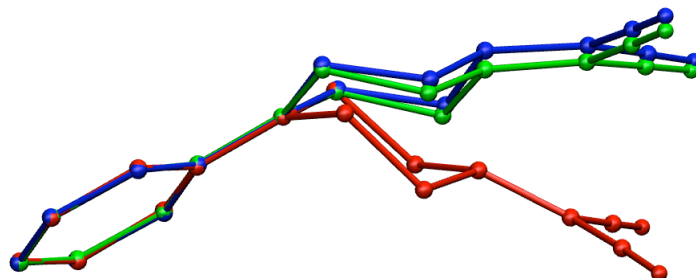


Figure 7.6: Geometries optimized in the  $S_1$  CT state. Red: CC2, blue: PBE, and green: PBE0. The structures were aligned at the donor moiety.

CC2/aug-cc-pVDZ				Experimental	
$\omega$	Stokes' shift		$\mu$		Stokes' shift
2.123 (0.0384)	1.562	CT	20.2865	2.727 (n-hexane <sup>c</sup> )	0.903
				2.293 (diethyl ether <sup>d</sup> )	1.311
4.154 (0.0296)		ID	3.0562	-	
4.272 (0.0237)		CT	3.8097	-	
4.562 (0.0168)		Rydberg	6.8941	-	

Table 7.8: CC2/aug-cc-pVDZ electronic excitation energies  $\omega$  (eV) and dipole moments  $\mu$  (Debye) of the  $S_1$  geometry optimized at the CC2/TZVP level. According to the location of the orbitals the excitations were labeled as charge transfer (CT), intra donor (ID) or Rydberg excitations. <sup>c</sup> Experimental fluorescence energy is taken from Ref. [185]. <sup>d</sup> Experimental fluorescence energy is taken from Ref. [188].

To gain insight into the nature of DBA fluorescence, we computed the excitation energies using aug-cc-pVDZ basis set (Table 7.8) for the geometries relaxed in the CT state. CC2 predicts a gas phase fluorescence energy of about 2.1 eV, very similar to the experimental value of 2.2 eV in polar solvent. Interestingly the CC2 gas phase value is considerably lower than the experimental value measured in apolar solvent (2.7 eV). This could indicate a kind of self stabilization of the bent zwitterionic geometry, which is decreased by the screening of the charges due to an apolar solvent. The solvent might also play a role in the interconversion from the ID state to the CT state by changing the energy gap between the two states.

Similar to the case of the vertical excitation spectra, TDPBE and TDPBE0 drastically underestimate the  $S_1$ - $S_0$  gap, predicting fluorescence energies of 0.341 and 1.628 eV, respectively.

	DA1	D+C1+C5	piperidine	A+C2+C4
PBE	0.527	0.178	0.059	0.053
PBE0	0.495	0.164	0.044	0.053

Table 7.9: RMSD (Å) between DFT structures and the CC2 structure optimized in the lowest CT state, for different fragments of DA1.

### 7.3.4 Geometries of the Excited Intradonor State

Hermant and coworkers [185] found that irrespective of the excitation wavelength a fluorescence typical for the CT state is always observed, leading to the conclusion that the locally excited states might interact with the CT states. To gain information about the interconversion process, we optimized the geometry of DA1 in the  $\pi_D-\pi_D^*$  ID state using the CC2/TZVP method. The corresponding optimization using TDDFT is not possible because the ID state mixes with one of the artificially low-lying CT states ( $2\pi_D-\pi_A^*$ ) and transforms adiabatically into the CT state. The mixing of the adiabatic states is caused by degenerate Kohn-Sham states. In the case of TDPBE0, LUMO+2 and LUMO+1 (Fig. 7.4) cross during the optimization and the initial character of the adiabatic state (H→HOMO+1) changes into a CT state when LUMO+1 adopts the character of the  $2\pi_A^*$  orbital. For this reason no local minimum for the ID state can be located using either TDPBE or TDPBE0, showing that the presence of artificially low-lying CT states in TDDFT affect properties of non-CT states. Therefore we report only the result of the CC2 optimization (Fig. 7.7, Cartesian coordinates in Table 7.5 of the appendix).

Structural changes in the ID state are much smaller than in the CT state. Consequently, the only significant change observed is the inversion of the sign of the N28-C9 twist angle similar to the  $S_1$  geometry. Twisting along the N-C bond in the locally excited state is typical for dialkylanilino derivatives [210]. In dimethylaniline compounds, twisting proceeds until an orthogonal conformation between the phenyl ring and the plane formed by the methyl groups and the nitrogen atom is reached. However, in the case of DA1, the twist angle does not exceed  $90^\circ$ , which most likely occurs because of steric hindrance due to the piperidine moiety.

Regarding the CC2/aug-cc-pVDZ excitation energies at the ID minimum energy structure (Table 7.10), we observe a decrease of the gap between  $S_1$  and  $S_2$  during the optimization from initially about 0.9 to 0.55 eV. We conclude that although the gap between the CT state and the ID state decreases, there is still thermal activation needed to decrease the gap to and allow interconversion from the ID to the

CC2/aug-cc-pVDZ		$\mu$
3.276 (0.180)	CT	19.709
3.827 (0.035)	ID	1.854
4.469 (0.058)	CT	5.430
4.678 (0.033)	Rydberg	6.517
4.848 (0.060)		4.084

Table 7.10: CC2/aug-cc-pVDZ excitation energies of the  $S_2$  geometry optimized on CC2/TZVP level (eV).

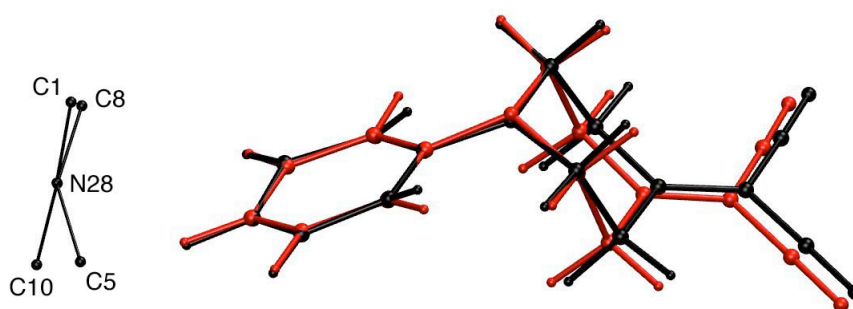


Figure 7.7: Left: Newman projection along the N28-C9 bond of the CC2 structure optimized in  $S_2$ . Right: CC2 geometries optimized in  $S_0$  (red) and optimized in  $S_1$  (black), aligned on the donor unit.

fluorescent CT state. The main difference between the  $S_1$  and  $S_2$  structures is that the C3 center is rather flat for the  $S_2$  structure but strongly pyramidal in  $S_1$ . Therefore we suspect the C3-pyramidalization to be an important reaction coordinate that could lead to a decrease of the gap between ID and CT states and may help to mediate a non-adiabatic transition.

## 7.4 Conclusions

Ground state geometries are well described by CC2 and the DFT methods we tested. A slightly better RMSD is found for DFT, especially using the PBE0 functional where a very good agreement with the crystal structure is found when the N-C twist angle of the donor is excluded (RMSD = 0.109 Å). However, all theoretical methods predict a twisted conformation of the phenyl substituent of the donor with respect to the central piperidine spacer, whereas the X-ray structure exhibits an almost symmetric conformation. Because of the fact that both, DFT and CC2 methods tend to be in a more asymmetric

conformation, we suspect that crystal packing effects are likely to be responsible for the more symmetric conformation of the phenyl substituent. A better answer to this question could be obtained by theoretical geometry optimization of the crystal, which is beyond the scope of the present work.

The experimental vertical absorption energies are very well reproduced by CC2, enabling a full assignment of the experimental bands. According to what was found experimentally, the lowest excited singlet state is due to a fluorescent CT state. We assign the next higher absorption band at 4.25 eV to a  $\pi$ - $\pi^*$  ID excitation. According to CC2, the experimentally observed band at 4.9 eV is accounted for by two separate states, one a CT state and the other one a Rydberg state. We find that the description of the latter two states is very sensitive to the inclusion of diffuse basis functions.

In contrast, TDDFT underestimates the  $S_1$  CT excitation by 1.4 eV using PBE and by 0.5 eV using PBE0. In addition, artificially low-lying CT states, which are not present in the CC2 spectra, are located between  $S_1$  and the ID state. Although, both TDDFT methods are able to reproduce the ID excitation energy to within 0.4 eV, mixing of the artificial CT states with the locally excited ID state perturbs the potential energy surface of the ID state in such a way that neither geometry optimizations nor molecular dynamics calculations can be carried out in a pure ID state. This finding rules out the use of TDDFT to gain structural and dynamical information about the ID state. The common practice of using TDDFT to describe only the locally excited states by ignoring the presence of artificially too low lying CT states [122] cannot be applied for the present system. In addition, excited state dipole moments are affected by the partial CT character.

For the  $S_1$  optimized geometry, the major characteristic of the CC2 structure is a bent conformation, that could be caused by the attraction of the negatively charged C3 center and the positively charged donor unit. In contrast, the linear geometries predicted by TDDFT are caused by a too strong flattening of the N28 center when compared with CC2. A delocalisation of the charges in the zwitterionic geometry could be responsible for the bending of the molecule not occurring.

Regarding fluorescence, CC2 is able to predict the emission energy within 0.1 eV compared to the value measured in diethyl ether, whereas a larger deviation of about 0.6 eV is found compared to the experimental value, measured in n-hexane. It is indicated that the solvent destabilizes the zwitterionic state. However, to obtain more information about the effect of the solvent on the excitation energies a more sophisticated model [220] would be required.

For the ID state we find a minimum energy structure indicating that the postulated interconversion from the ID state to the  $S_1$  CT state requires activation by thermal energy. However, although we find a decrease of the  $S_2$ - $S_1$  energy gap for the ID geometry from 0.9 eV at  $S_0$  equilibrium structure to 0.55 eV, the mechanism of the interconversion cannot be described on the basis of the present results based on single geometries. Finite temperature excited state molecular dynamics calculations, at the CC2 level, could provide information about the interconversion mechanism.

In summary, this study shows that CC2 using a large basis set is able to describe accurately the electronic absorption and fluorescence energies of a DBA molecule for both local and CT states. TDDFT in contrast fails to describe absorption and emission energies of the CT states, where a partial improvement is obtained by using a hybrid functional. Locally excited states are described at more reasonable excitation energies. However, it is shown that locally excited states are affected by the TDDFT failure for CT states. This holds for both, the purely local PBE functional as well as for the hybrid functional PBE0.

Furthermore, equilibrium geometries for ground and the first two low lying excited states were determined. For the zwitterionic structure large differences are found between the CC2 and the DFT structures.

## 7.5 Appendix

Table 7.11: Ground State Equilibrium Geometries (Å)

Atom	CC2/TZVP			PBE/TZVP			PBE0/TZVP		
	<i>x</i>	<i>y</i>	<i>z</i>	<i>x</i>	<i>y</i>	<i>z</i>	<i>x</i>	<i>y</i>	<i>z</i>
C	8.5883961	4.0839319	5.3730607	8.6183527	4.0609037	5.1218392	8.6079487	4.0676267	5.1355389
C	9.1905532	4.4299289	3.9870611	9.3707219	4.4558169	3.8070828	9.4055230	4.4460453	3.8647127
C	9.8969682	5.7366182	4.1126268	10.0926668	5.7434015	4.0220930	10.1212922	5.7314164	4.0841114
C	9.0468721	6.8483489	4.6259484	9.2360494	6.8550702	4.5305609	9.2588754	6.8389154	4.5779955
C	8.4299076	6.3827698	5.9712943	8.4971057	6.3541432	5.8142618	8.4739005	6.3461143	5.8150054
C	3.8304602	5.2569161	4.0795422	3.6882164	5.2557967	4.3412225	3.6930114	5.2394000	4.3426661
C	4.4095538	4.0478661	4.4692437	4.3146635	4.0430636	4.6440842	4.3250527	4.0366781	4.6304508
C	5.6956833	4.0125978	4.9987443	5.6488398	4.0057455	5.0403904	5.6526096	4.0044920	5.0178728
C	6.4207040	5.1990053	5.2261457	6.4135240	5.1891435	5.1369210	6.4063702	5.1841170	5.1187946
C	5.8180305	6.4145670	4.8506496	5.7725880	6.4079734	4.8280901	5.7595280	6.3906878	4.8226745
C	4.5213242	6.4386432	4.3329706	4.4297274	6.4338483	4.4432373	4.4231151	6.4117116	4.4491483
C	11.2450279	5.8625074	3.9416616	11.4578754	5.8548797	3.9121828	11.4636492	5.8582102	3.9321994
C	12.0519161	4.7608001	3.5181231	12.2730665	4.7513544	3.5126738	12.2792768	4.7693867	3.4992292
C	11.9094602	7.1093547	4.1622367	12.1364161	7.0790005	4.2045478	12.1376687	7.0878570	4.1977793
H	9.3961900	3.9804936	6.1033270	9.3604182	3.8340916	5.9033955	9.3114460	3.8407749	5.9437275
H	8.0699192	3.1302119	5.3169046	8.0418654	3.1492110	4.9382284	8.0428864	3.1606466	4.9372800
H	8.3600864	4.5220159	3.2782344	8.6083561	4.5850220	3.0196174	8.6884474	4.5772408	3.0458003
H	9.8551545	3.6324223	3.6486836	10.0485880	3.6467214	3.5012427	10.0889637	3.6405132	3.5916946
H	8.2384889	7.0375914	3.9128684	8.4746151	7.1096744	3.7750335	8.5427983	7.1015373	3.7907601
H	9.6150576	7.7702109	4.7668641	9.8192109	7.7596378	4.7530635	9.8398063	7.7310459	4.8194757
H	7.7876454	7.1559613	6.3920666	7.8363861	7.1371284	6.2039214	7.8098521	7.1286935	6.1772306
H	9.2401079	6.2086356	6.6855308	9.2523768	6.1537267	6.5910271	9.1892184	6.1418813	6.6192169
H	2.8282823	5.2816096	3.6707644	2.6410300	5.2823203	4.0384162	2.6514951	5.2603098	4.0466435
H	3.8786163	3.1150281	4.3183519	3.7526799	3.1087091	4.5912112	3.7732654	3.1045238	4.5714634
H	6.0965420	3.0613318	5.3241229	6.0876855	3.0472064	5.3174194	6.0959600	3.0524789	5.2814326
H	6.3170459	7.3591890	5.0175853	6.3160647	7.3519493	4.8770899	6.2925528	7.3316742	4.8731985
H	4.0853920	7.3929270	4.0602155	3.9645850	7.3940590	4.2112060	3.9548123	7.3655957	4.2298093
N	7.6929757	5.1368843	5.8410149	7.7504361	5.1332287	5.5829410	7.7342068	5.1363505	5.5602707
N	12.7024513	3.8359989	3.1723001	12.9352725	3.8442608	3.1923586	12.9287591	3.8810815	3.1553377
N	12.4351535	8.1504663	4.3569345	12.6823982	8.0814679	4.4494753	12.6708854	8.0847069	4.4240977

Table 7.12:  $S_1$  Equilibrium Geometries (Å)

Atom	CC2/TZVP			TDPBE/TZVP			TDPBE0/TZVP		
	<i>x</i>	<i>y</i>	<i>z</i>	<i>x</i>	<i>y</i>	<i>z</i>	<i>x</i>	<i>y</i>	<i>z</i>
C	8.6046410	3.9711330	5.4255140	8.5381533	4.1108472	4.9160707	8.5443160	4.1080735	4.9281079
C	9.5282361	4.3919798	4.2692857	9.7676955	4.4815944	4.1017700	9.7158878	4.4853350	4.0431312
C	10.1903747	5.6982942	4.5779301	10.4578087	5.7161274	4.6392780	10.3856155	5.7365522	4.5110121
C	9.2213718	6.7943856	4.8974054	9.4631206	6.8533944	4.7177607	9.4128544	6.8588434	4.6808079
C	8.2812841	6.3331628	6.0190672	8.2462127	6.4619107	5.5399900	8.2523745	6.4423385	5.5605532
C	3.7525757	4.9319701	4.0950141	3.4038349	4.7886546	4.8100719	3.4594708	4.8027303	4.7558348
C	4.3822858	3.7536924	4.5096097	4.2467695	3.6702485	4.6731802	4.2913377	3.6856221	4.6464090
C	5.6639091	3.7968113	5.0364651	5.6167931	3.8053407	4.7265551	5.6516601	3.8097689	4.7350753
C	6.3641958	5.0253236	5.0810696	6.2255253	5.0940222	4.9437129	6.2611380	5.0869066	4.9572130
C	5.7159524	6.2153778	4.6710141	5.3385347	6.2255299	5.0605828	5.3840919	6.2161029	5.0512409
C	4.4446525	6.1484928	4.1240126	3.9714957	6.0620954	4.9984439	4.0271032	6.0632180	4.9545535
C	11.3531765	6.0519422	3.7940598	11.7512835	6.0217676	4.0898666	11.6934131	6.0291625	4.0315441
C	12.1071720	5.0456469	3.1653868	12.5571299	5.0128374	3.5231094	12.5157676	5.0207916	3.5014763
C	11.7987741	7.3850786	3.7739949	12.2678352	7.3327792	4.1342443	12.2310500	7.3232804	4.1281763
H	9.1740351	3.8811360	6.3518272	8.8352934	3.8958895	5.9592551	8.9016118	3.8893008	5.9412369
H	8.0676410	3.0520242	5.2044151	8.0462151	3.2304420	4.4979736	8.0405136	3.2312440	4.5383427
H	8.9054890	4.4222264	3.3529097	9.4795700	4.6252000	3.0350346	9.3613955	4.5781319	2.9982516
H	10.2605787	3.5914337	4.1318384	10.4235163	3.5985298	4.1183833	10.3996621	3.6328827	4.0502020
H	8.5997571	7.0892656	4.0290206	9.1450777	7.1785857	3.7003977	9.0237095	7.2176788	3.7084587
H	9.7339053	7.6967185	5.2431028	9.8901295	7.7450238	5.1995701	9.8751106	7.7267075	5.1569569
H	7.5022753	7.0479228	6.2792487	7.5298522	7.2808823	5.6352376	7.5294506	7.2408269	5.6841773
H	8.8702967	6.0888570	6.9058329	8.5768088	6.1716787	6.5553646	8.6326480	6.1749270	6.5541552
H	2.7502843	4.8928238	3.6864262	2.3214785	4.6708245	4.7561811	2.3852352	4.6926318	4.6782312
H	3.8433917	2.8147450	4.4940313	3.8144450	2.6809103	4.5202642	3.8592061	2.7045847	4.4922771
H	6.1269747	2.8873216	5.3937293	6.2345063	2.9190554	4.6228815	6.2565139	2.9210128	4.6602960
H	6.2536244	7.1533096	4.6684143	5.7427934	7.2270511	5.1672200	5.7848274	7.2096172	5.1675458
H	3.9668080	7.0555953	3.7757813	3.3256611	6.9368584	5.0806825	3.3901911	6.9365648	5.0208241
N	7.6393804	5.0717033	5.6041608	7.5617061	5.2371931	5.0257682	7.5863866	5.2189460	5.0771959
N	12.6678427	4.1278863	2.6475847	13.1833580	4.1299893	3.0635140	13.1579887	4.1522825	3.0732247
N	12.0836008	8.5440437	3.7979910	12.6489341	8.4430163	4.2036510	12.6345202	8.4079809	4.2312033



Table 7.13:  $S_2$  Equilibrium Geometry ( $\text{\AA}$ )

CC2/TZVP			
Atom	$x$	$y$	$z$
C	8.5825075	4.1038785	5.3076390
C	9.2899380	4.4734697	3.9838296
C	10.0063322	5.7721241	4.1660530
C	9.1635054	6.8978181	4.6730594
C	8.4351002	6.4313526	5.9524420
C	3.7867333	5.2385148	4.1837925
C	4.3951462	4.0083914	4.4848469
C	5.7211217	3.9742811	5.0331655
C	6.3843407	5.2309954	5.2145374
C	5.7748408	6.4703334	4.8946011
C	4.3992187	6.4778372	4.4819967
C	11.3530514	5.8916044	3.9990519
C	12.1564736	4.7943039	3.5553062
C	12.0280535	7.1287142	4.2453065
H	9.3144716	3.9699738	6.1083870
H	8.0005463	3.1969231	5.1685549
H	8.5080080	4.5756464	3.2230801
H	9.9653553	3.6680494	3.6885643
H	8.4010971	7.1439499	3.9258525
H	9.7541272	7.7916314	4.8840791
H	7.7492736	7.1874979	6.3283273
H	9.1662457	6.2007470	6.7324970
H	2.7804659	5.2361082	3.7767506
H	3.8650505	3.0824451	4.2983221
H	6.0568534	3.1034137	5.5874869
H	6.3532332	7.3846471	4.8459858
H	3.9241900	7.4085943	4.2013448
N	7.7010787	5.2087916	5.6647650
N	12.8084388	3.8772478	3.1932309
N	12.5620174	8.1610329	4.4608570



## Chapter 8

# Conclusions and Outlook

In this thesis, a non-adiabatic AIMD scheme has been developed and implemented, and then applied to the study of decay processes, such as fragmentation, isomerization, and de-excitation, which occur upon photoexcitation of different organic molecules. The method is based on the Fewest-Switches Trajectory SH method and uses TDDFT as underlying electronic structure method.

Furthermore, the accuracy of approximations within TDDFT is assessed by comparison with the results of wavefunction-based excited-state methods. This investigation focuses on the evaluation of the performance of a number of different issues that are particularly important for the modeling of photoprocesses. These aspects include a) the accuracy of non-adiabatic coupling vectors, b) the description of conical intersections, and c) the description of locally excited states in the presence of CT states.

The newly developed non-adiabatic AIMD scheme (TDDFT-SH) is tested by studying the photodynamical processes of two small well-studied organic molecules, oxirane and protonated formalimine. For protonated formalimine, a good agreement with results of simulations based on CASSCF is found. The TDDFT-SH method and the CASSCF-SH method agree in the predicted reaction mechanism as well as with respect to the predicted excited state lifetimes. In the case of oxirane, the TDDFT-SH results are consistent with experimental data and furthermore provides a detailed mechanistic description that is difficult to obtain by experiments.

These examples show that the developed method constitutes a tool for the description of photodynamical processes of molecular systems that can reach accuracy similar to wavefunction-based methods but has the advantage of being easier to use and computationally more efficient.

However, it is also shown that TDDFT bears some limitations which arise from both, the approximate nature of the ground state xc-functional and the adiabatic approximation made in the TDDFT kernel. For some of these deficiencies, remedies are already available [145, 174, 221]. For instance, the underestimation of excitation energies due to the incorrect asymptotic behavior of the xc-potential can be overcome by the use of asymptotically corrected or hybrid functionals, as we have seen in the case of oxirane.

It is not yet clear how strongly the shortcomings in the description of the coupling between  $S_1$  and  $S_0$  and the  $S_1$ - $S_0$  intersections affect molecular dynamics simulations. Further comparisons of the TDDFT-SH method to other methods are necessary to fully establish to which extent the inaccuracies of the  $S_1$ - $S_0$  intersections can be corrected by an adapted surface hopping algorithm such as the one proposed in this work.

For the non-adiabatic coupling vectors evaluated at ground state equilibrium geometries, TDDFT provides a qualitative description similar to multiconfigurational CASSCF. However, the TDDFT-SH simulations show that in regions close to the  $S_1$ - $S_0$  intersection the coupling appears to be orders of magnitude smaller than the one close to intersections between excited states. With respect to the fact that  $S_1$  and  $S_0$  “do not see each other” in this region, TDDFT-TDA behaves similar to CIS. On the other hand, TDDFT-TDA seems to be able to account for the mixing between ground and excited states as shown by the shape of the intersection that appears to be approximately conical and resembles the CASSCF intersection on a larger scale. Not much is known about the effect the approximation in the xc-kernel regarding these problems. To some extent it seems that the LR-TDDFT method incorporates a certain degree of correlation, which in post Hartree-Fock methods would be included by double excitations, although linear response TDDFT is formulated in terms of singly excited determinants. This could account for the global similarity to the multiconfigurational description of the conical intersection.

We have shown that the problem of describing the energy of long-range CT excitations is severe, since it changes qualitatively the order of the adiabatic states and furthermore it affects the description of other excited states that do not have a CT character. This can cause problems if one considers simulations of larger systems in complex environments like liquids, where a large number of possible CT states could influence the dynamics. A few corrections to the CT failure in TDDFT have already been proposed [83, 103, 222], future validation studies will help to understand if these corrections are able to tackle this

problem.

The CC2 method on the other hand, has been shown to provide a highly accurate description of both, CT and non-CT states. An unbiased description of all types of states is an important requirement for the dynamical description of photoprocesses. Although for small molecules, AIMD simulations based on CC2 are already possible, more extensive applications of the method are still limited due to the fast growing computational expense that arises when the system size is increased. This is especially acute when high quality basis sets with diffuse functions are used, which is often necessary for a proper description of excited states.

It remains the hope that improvements in the development of xc-functionals and kernels become available for a more accurate modeling of dynamical processes. This requires that nuclear gradients from the improved xc-functionals can be obtained. However, improvements should not substantially increase the computational cost. The TDDFT-SH method is independent of the approximation used for the xc-functional and can directly profit from any improvement of the xc-functionals that leads to more accurate TDDFT potential energy surfaces.



# Bibliography

- [1] J. Michl and V. Bonačič-Koutecký, editors. *Electronic Aspects of Organic Photochemistry*. John Wiley and Sons, Inc., New York, 1990.
- [2] J. N. Turro. *Modern Molecular Photochemistry*. University Science Books, 1991.
- [3] E. Rabinowitch. *Discuss. Faraday. Soc.*, 27:161, 1959.
- [4] K.H. Kraemer. *Proc. Natl. Acad. Sci. U. S. A.*, 94:11, 1997.
- [5] R.P. Sinha and D.P. Hader. *Photochem. Photobiol. Sci.*, 1:225, 2002.
- [6] C.E. Crespo-Hernandez, B. Cohen, and B. Kohler. *Nature*, 436:1141, 2005.
- [7] V. Vaida and J. D. Simon. *Science*, 268:1443, 1995.
- [8] N. Koumura, R. W. J. Zijlstra, R. A. van Delden, N. Harada, and B.L. Feringa. *Nature*, 401:152, 1999.
- [9] B.L. Feringa. *Accounts Chem. Res.*, 34:504, 2001.
- [10] A. Toniolo, B. G. Levine, A.L. Thompson, J. Quenneville, M. Ben-Nun, J.M. Owens, S. Olsen, L. Manohar, and T.J. Martinez. *Mol. Supram. Photochem.*, 13:167, 2005.
- [11] W. Domcke, D. R. Yarkony, and H. Köppel, editors. *Conical Intersections: Electronic Structure, Dynamics & Spectroscopy*, volume 15 of *Advanced Series in Physical Chemistry*. 2004.
- [12] D. Marx and J. Hutter. *Modern Methods and Algorithms of Quantum Chemistry*, volume 1 of *NIC Series*, page 301. Forschungszentrum Jülich, 2000.
- [13] R. Car and M. Parrinello. *Phys. Rev. Lett.*, 55:2471, 1985.

- [14] H. Lischka, R. Shepard, R. M. Pitzer, I. Shavitt, M. Dallos, T. Muller, P. G. Szalay, M. Seth, G. S. Kedziora, S. Yabushita, and Z. Y. Zhang. *Phys. Chem. Chem. Phys.*, 3:664, 2001.
- [15] T. Ziegler, A. Rauk, and E. J. Baerends. *Theor. Chim. Acta*, 43:261, 1977.
- [16] C. Daul. *Int. J. Quantum Chem.*, 52:867, 1994.
- [17] I. Frank, J. Hutter, D. Marx, and M. Parrinello. *J. Chem. Phys.*, 108:4060–4069, 1998.
- [18] N. L. Doltsinis and D. Marx. *Phys. Rev. Lett.*, 88:166402, 2002.
- [19] E. Runge and E. K. U. Gross. *Phys. Rev. Lett.*, 52:997, 1984.
- [20] M. E. Casida. In D. P. Chong, editor, *Recent Advances in Density Functional Methods*, page 155. Singapore, World Scientific, 1995.
- [21] E. Tapavicza, I. Tavernelli, and U. Röthlisberger. *Phys. Rev. Lett.*, 98:023001, 2007.
- [22] M. Born and J. R. Oppenheimer. *Ann. Physik*, 84:457, 1927.
- [23] M. Born and K. Huang. *Dynamical Theory of Crystal Lattices*. Oxford University Press, 1954.
- [24] L. S. Cederbaum. In W. Domcke, D. R. Yarkony, and H. Köppel, editors, *Conical Intersections: Electronic Structure, Dynamics & Spectroscopy*, volume 15 of *Advanced Series in Physical Chemistry*, chapter 1, page 3. World Scientific, Singapore, 2004.
- [25] V. May and O. Kühn. *Charge and Energy Transfer Dynamics in Molecular Systems*. Wiley-VCH, Weinheim, 2005.
- [26] G. A. Worth and L. S. Cederbaum. *Annu. Rev. Phys. Chem.*, 55:127, 2004.
- [27] K. Drukker. *J. Comput. Phys.*, 153:225, 1999.
- [28] N. Doltsinis and D. Marx. *J. Theor. Comput. Chem.*, 1:319, 2002.
- [29] G. Stock and M. Thoss. In W. Domcke, D. R. Yarkony, and H. Köppel, editors, *Conical Intersections: Electronic Structure, Dynamics & Spectroscopy*, volume 15 of *Advanced Series in Physical Chemistry*, chapter 15, page 619. World Scientific, Singapore, 2004.



- [30] J. C. Tully. *J. Chem. Phys.*, 93:1061, 1990.
- [31] A. Szabo and N.S. Ostlund. *Modern Quantum Chemistry: Introduction to Advanced Electronic Structure Theory*. Dover Publications, Inc., Mineola, New York, 1996.
- [32] T. Helgaker, P. Jørgensen, and J. Olsen, editors. *Molecular Electronic-Structure Theory*. John Wiley and Sons, Inc., The Atrium, Southern Gate, Chichester, West Sussex PO19 8SQ, England, 2000.
- [33] O. Christiansen. *Theor. Chem. Acc.*, 116:106, 2006.
- [34] O. Christiansen, H. Koch, and P. Jørgensen. *Chem. Phys. Lett.*, 243:409, 1995.
- [35] R. G. Parr and W. Yang. *Density Functional Theory of Atoms and Molecules*. Oxford University Press, 1989.
- [36] R. M. Dreizler and E. K. U. Gross. *Density Functional Theory*. Springer, Berlin, 1990.
- [37] W. Koch and M. C. Holthausen. *A Chemists Guide to Density Functional Theory*. Wiley-VCH, 1999.
- [38] F. Nogueira, A. Castro, and M. A. L. Marques, editors. *A Primer in Density Functional Theory*, volume 620 of *Lect. Notes. Phys.* 2003.
- [39] M. A. L. Marques and E. K. U. Gross. In F. Nogueira, A. Castro, and M. A. L. Marques, editors, *A Primer in Density Functional Theory*, volume 620 of *Lect. Notes. Phys.*, chapter 4, page 144. Springer, Berlin, 2003.
- [40] M. A. L. Marques and E. K. U. Gross. *Annu. Rev. Phys. Chem.*, 55:427, 2004.
- [41] M. A. L. Marques, C.A. Ullrich, F. Nogueira, A. Rubio, K. Burke, and E. K. U. Gross, editors. *Lecture Notes of Physics*. Springer, Berlin, 2006.
- [42] A. Dreuw and M. Head-Gordon. *Chem. Rev.*, 105:4009, 2005.
- [43] A. Dreuw. *ChemPhysChem*, 7:2259, 2006.
- [44] P. Hohenberg and W. Kohn. *Phys. Rev.*, 136:B864, 1964.

- [45] W. Kohn and L. J. Sham. *Phys. Rev.*, 140:A1133, 1965.
- [46] R. van Leeuwen. *Phys. Rev. Lett.*, 80:1280, 1998.
- [47] R. van Leeuwen. *Int. J. Mod. Phys. B*, 15:1969, 2001.
- [48] S. Hirata and M. Head-Gordon. *Chem. Phys. Lett.*, 314:291, 1999.
- [49] F. Cordova, L. Jourbert Doriol, A. Ipatov, M. E. Casida, C. Filippi, and A. Vela. *J. Chem. Phys.*, 127:164111, 2007.
- [50] C. F. Craig, W. R. Duncan, and O. V. Prezhdo. *Phys. Rev. Lett.*, 95:163001, 2005.
- [51] E. K. U. Gross and W. Kohn. *Phys. Rev. Lett.*, 55:2850, 1985.
- [52] J. Hutter. *J. Chem. Phys.*, 118:3928–3934, 2003.
- [53] F. Furche and R. Ahlrichs. *J. Chem. Phys.*, 117:7433, 2002.
- [54] N. L. Doltsinis and D. S. Kosov. *J. Chem. Phys.*, 122:166402, 2005.
- [55] T. Kreibich and E. K. U. Gross. *Phys. Rev. Lett.*, 86:2984, 2001.
- [56] J. C. Tully. In D. L. Thompson, editor, *Modern Methods for Multidimensional Dynamics Computations in Chemistry*. Singapore, World Scientific, 1998.
- [57] M.D. Hack and D.G. Truhlar. *J. Phys. Chem. A*, 104:7917, 2000.
- [58] S. R. Billeter and A. Curioni. *J. Chem. Phys.*, 122:034105, 2005.
- [59] R. Baer. *Chem. Phys. Lett.*, 364:75, 2002.
- [60] S. Baroni, P. Giannozzi, and A. Testa. *Phys. Rev. Lett.*, 58:1861, 1987.
- [61] S. Hammes-Schiffer and J. C. Tully. *J. Chem. Phys.*, 101:4657, 1994.
- [62] *CPMD, Version 3.10.0*. Copyright IBM Corp 1990-2006, Copyright MPI für Festkörperforschung Stuttgart, 1997-2001. <http://www.cpmc.org>.
- [63] F. Gai, K.C. Hasson, J.C. McDonald, and P.A. Anfinrud. *Science*, 279:1886, 1998.

- [64] V. V. Bonačić-Koutecký, K. Schoffel, and J. Michl. *Theor. Chim. Acta*, 72:459, 1987.
- [65] M. Barbatti, A.J.A. Aquino, and H. Lischka. *Mol. Phys.*, 104:1053, 2006.
- [66] J.P. Perdew, K. Burke, and M. Ernzerhof. *Phys. Rev. Lett.*, 77:3865, 1996.
- [67] N. Troullier and J.L. Martins. *Phys. Rev. B*, 43:1993, 1991.
- [68] M. J. Frisch, G. W. Trucks, H. B. Schlegel, G. E. Scuseria, M. A. Robb, J. R. Cheeseman, J. A. Montgomery, Jr., T. Vreven, K. N. Kudin, J. C. Burant, J. M. Millam, S. S. Iyengar, J. Tomasi, V. Barone, B. Mennucci, M. Cossi, G. Scalmani, N. Rega, G. A. Petersson, H. Nakatsuji, M. Hada, M. Ehara, K. Toyota, R. Fukuda, J. Hasegawa, M. Ishida, T. Nakajima, Y. Honda, O. Kitao, H. Nakai, M. Klene, X. Li, J. E. Knox, H. P. Hratchian, J. B. Cross, C. Adamo, J. Jaramillo, R. Gomperts, R. E. Stratmann, O. Yazyev, A. J. Austin, R. Cammi, C. Pomelli, J. W. Ochterski, P. Y. Ayala, K. Morokuma, G. A. Voth, P. Salvador, J. J. Dannenberg, V. G. Zakrzewski, S. Dapprich, A. D. Daniels, M. C. Strain, O. Farkas, D. K. Malick, A. D. Rabuck, K. Raghavachari, J. B. Foresman, J. V. Ortiz, Q. Cui, A. G. Baboul, S. Clifford, J. Cioslowski, B. B. Stefanov, G. Liu, A. Liashenko, P. Piskorz, I. Komaromi, R. L. Martin, D. J. Fox, T. Keith, M. A. Al-Laham, C. Y. Peng, A. Nanayakkara, M. Challacombe, P. M. W. Gill, B. Johnson, W. Chen, M. W. Wong, C. Gonzalez, , and J. A. Pople. *Gaussian 03, Revision B.05*. Gaussian, Inc., Pittsburgh PA, 2003.
- [69] K.F. Donchi, B.A. Rumpf, G.D. Willett, J.R. Christie, and P.J. Derrick. *J. Am. Chem. Soc.*, 110:347, 1988.
- [70] F. Bernardi, M. Olivucci, and M. A. Robb. *Chem. Soc. Rev.*, 25:321, 1996.
- [71] J. F. Janak. *Phys. Rev. B*, 18:7165, 1978.
- [72] J. C. Slater. volume 4 of *The Self-Consistent Field for Molecules and Solids*. McGraw-Hill, New York, 1974.
- [73] S. R. Billeter and D. Egli. *J. Chem. Phys.*, 125:224103, 2006.
- [74] V. Chernyak and S. Mukamel. *J. Chem. Phys.*, 112:3572, 2000.
- [75] C.P. Hu, H. Hirai, and O. Sugino. *J. Chem. Phys.*, 127:064103, 2007.

- [76] H.-J. Werner, P. J. Knowles, R. Lindh, F. R. Manby, and M. Schütz. Molpro, version 5 a package of ab initio programs.
- [77] L. Bernasconi, M. Sprik, and J. Hutter. *J. Chem. Phys.*, 119:12417, 2003.
- [78] R. Ahlrichs, M. Bär, M. Häser, H. Horn, and C. Kölmel. *Chem. Phys. Lett.*, 162:165, 1989.
- [79] F. Weigend, M. Häser, H. Patzelt, and R. Ahlrichs. *Chem. Phys. Lett.*, 294:143, 1998.
- [80] R. Ditchfield, W. J. Hehre, and J. A. Pople. *J. Chem. Phys.*, 54:724, 1971.
- [81] T. Clark, J. Chandrasekhar, G. W. Spitznagel, and P. V. Schleyer. *J. Comput. Chem.*, 4:294, 1983.
- [82] V. Engel, V. Staemmler, R. L. Vanderwal, F. F. Crim, R. J. Sension, B. Hudson, P. Andresen, S. Hennig, K. Weide, and R. Schinke. *J. Phys. Chem.*, 96:3201, 1992.
- [83] A. Dreuw, J. Weisman, and M. Head-Gordon. *J. Chem. Phys.*, 119:2943, 2003.
- [84] J. Lorentzon, M. P. Fülscher, and B. O. Roos. *J. Am. Chem. Soc.*, 117:9265, 1995.
- [85] C. Jamorski, M. E. Casida, and D. R. Salahub. *J. Chem. Phys.*, 104:5134, 1996.
- [86] R. Bauernschmitt and R. Ahlrichs. *Chem. Phys. Lett.*, 256:454, 1996.
- [87] M. Chachisville and A.H. Zewail. *J. Phys. Chem. A*, 103:7408, 1999.
- [88] J. Danielsson, J. Ulicny, and A. Laaksonen. *J. Am. Chem. Soc.*, 123:9817, 2001.
- [89] E. W.-G. Diau, C. Kötting, and A.H. Zewail. *ChemPhysChem*, 2:273, 2001.
- [90] E. W.-G. Diau, C. Kötting, and A.H. Zewail. *ChemPhysChem*, 2:294, 2001.
- [91] E. W.-G. Diau, C. Kötting, T.I. Sølling, and A.H. Zewail. *ChemPhysChem*, 3:57, 2002.
- [92] T.I. Sølling, E. W.-G. Diau, C. Kötting, S. De Feyter, and A.H. Zewail. *ChemPhysChem*, 3:79, 2002.
- [93] G. Orlova, J.D. Goddard, and L.Y. Brovko. *J. Am. Chem. Soc.*, 125:6962, 2002.
- [94] E.W.G. Diau and A.H. Zewail. *ChemPhysChem*, 4:445, 2003.

- [95] J. Llano, J. Raber, and L.A. Eriksson. *J. Photochem. and Photobiol. A-Chem.*, 154:235, 2003.
- [96] D. Rappoport and F. Furche. *J. Am. Chem. Soc.*, 126:1277, 2004.
- [97] J. Černý, V. Špirko, M. Mons, P. Hobza, and D. Nachtigallová. *Phys. Chem. Chem. Phys.*, 8:3059, 2006.
- [98] K.Q.K. Musa and L.A. Eriksson. *J. Phys. Chem. B*, 111:13345, 2007.
- [99] M.E. Casida. In M.R. Hoffmann and K.G. Dyall, editors, *Accurate Description of Low-Lying Molecular States and Potential Energy Surfaces*, ACS Symposium Series 828. ACS Press, Washington, D.C., 2002.
- [100] M. E. Casida, C. Jamorski, K. C. Casida, and D. R. Salahub. *J. Chem. Phys.*, 108:4439, 1998.
- [101] M.E. Casida. *J. Chem. Phys.*, 122:054111, 2005.
- [102] B.G. Levine, C. Ko, J. Quenneville, and T.J. Martinez. *Mol. Phys.*, 104:1039, 2006.
- [103] M. E. Casida, F. Gutierrez, J. Guan, F.-X. Gadea, D. Salahub, and J.-P. Daudey. *J. Chem. Phys.*, 113:7062, 2000.
- [104] M. Bargheer, A. Cohen, R.B. Gerber, M. Guhr, M.V. Korolkov, J. Manz, M.Y. Niv, M. Schröder, and N. Schwentner. *J. Phys. Chem. A*, 111:9573, 2007.
- [105] G. Granucci and M. Persico. *Theor. Chem. Acc.*, 117:1131, 2007.
- [106] P.R.L. Markwick and N.L. Doltsinis. *J. Chem. Phys.*, 126:175102, 2007.
- [107] G. Zechmann, M. Barbatti, H. Lischka, J. Pittner, and V. Bonačič-Koutecký. *Chem. Phys. Lett.*, 418:377, 2006.
- [108] H. Langer, N.L. Doltsinis, and D. Marx. *ChemPhysChem*, 6:1734, 2005.
- [109] Z.W. Qu, H. Zhu, S.Y. Grebenshchikov, and R. Schinke. *J. Chem. Phys.*, 122:191102, 2005.
- [110] M. Barbatti, M. Ruckebauer, and H. Lischka. *J. Chem. Phys.*, 122:174307, 2005.
- [111] M. Barbatti, G. Granucci, M. Persico, and H. Lischka. *Chem. Phys. Lett.*, 401:276, 2005.

- [112] N. Winter and I. Benjamin. *J. Chem. Phys.*, 121:2253, 2004.
- [113] C. Ciminelli, G. Granucci, and M. Persico. *Chem.-Eur. J.*, 10:2327–2341, 2004.
- [114] P. Cattaneo and N. Persico. *J. Am. Chem. Soc.*, 123:7638, 2001.
- [115] C. Collaveri, G. Granucci, M. Persico, and A. Toniolo. *J. Chem. Phys.*, 115:1251, 2001.
- [116] C. Van Caillie and R.D. Amos. *Chem. Phys. Lett.*, 308:249, 1999.
- [117] C. Van Caillie and R.D. Amos. *Chem. Phys. Lett.*, 317:159, 2000.
- [118] D. Rappoport and F. Furche. *J. Chem. Phys.*, 122:064105, 2005.
- [119] G. Scalmani, M.J. Frisch, B. Mennucci, J. Tomasi, R. Cammi, and V. Barone. *J. Chem. Phys.*, 124:094107, 2006.
- [120] I. Tavernelli, U. F. Rohrig, and U. Röthlisberger. *Mol. Phys.*, 103:963, 2005.
- [121] M.E. Moret, E. Tapavicza, L. Guidoni, U.F. Rohrig, M. Sulpizi, I. Tavernelli, and U. Rothlisberger. *Chimia*, 59:493, 2005.
- [122] S. R. Mercier, O. V. Boyarkin, A. Kamariotis, M. Guglielmi, I. Tavernelli, M. Cascella, U. Rothlisberger, and T. R. Rizzo. *J. Am. Chem. Soc.*, 128:16938, 2006.
- [123] E. Gomer and Jr. W. A. Noyes. *J. Am. Chem. Soc.*, 72:101, 1950.
- [124] W.M.C. Foulkes, L. Mitas, R.J. Needs, and G. Rajagopal. *Rev. Mod. Phys.*, 73:33, 2001.
- [125] F. Schautz and C. Filippi. *J. Chem. Phys.*, 120:10931, 2004.
- [126] F. Schautz, F. Buda, and C. Filippi. *J. Chem. Phys.*, 121:5836, 2004.
- [127] L. D. Landau. *Phys. Z. Sowjetunion*, 2:46, 1932.
- [128] C. Zener. *Proc. R. Soc. London, Ser. A*, 137:696, 1932.
- [129] E. C. G. Stueckelberg. *Helv. Phys. Acta*, 5:369, 1932.
- [130] C. Wittig. *J. Phys. Chem. B*, 109:8428, 2005.

- [131] G. A. Jones, B. K. Carpenter, and M. N. Paddon-Row. *J. Am. Chem. Soc.*, 120:5499, 1990.
- [132] M. Kawasaki, T. Ibuki, M. Iwasaki, and Y. Takezaki. *J. Chem. Phys.*, 59:2076, 1973.
- [133] K. Kasha. *Discuss. Faraday Soc.*, 9:14, 1950.
- [134] B. Bigot, A. Sevin, and A. Devaquet. *J. Am. Chem. Soc.*, 101:1095, 1979.
- [135] A. Joshi, X.Q. You, T.A. Barckholtz, and H. Wang. *J. Phys. Chem. A*, 109:8016, 2005.
- [136] X. Yang, S. Maeda, and K. Ohno. *J. Phys. Chem. A*, 111:5099, 2007.
- [137] B.C. Shepler, B.J. Braams, and J.M. Bowman. *J. Phys. Chem. A*, 111:8282, 2007.
- [138] B. C. Roquitte. *J. Phys. Chem.*, 70:2699, 1981.
- [139] C. Wesdemiotis, B. Leyh, A. Fura, and F.W. McLafferty. *J. Am. Chem. Soc.*, 112:8655, 1990.
- [140] A. Sandoski and J.J. BelBruno. *J. Phys. Org. Chem.*, 12:681, 1999.
- [141] C.J. Umrigar and C. Filippi. a qmc program package.
- [142] andM.Dolg M.Burkatzki, C.Filippi. *J. Chem. Phys.*, 126:234105, 2007.
- [143] S.H. Vosko, L. Wilk, and M. Nusair. *Can. J. Phys.*, 58:1200, 1980.
- [144] R. Vanleeuwen and E.J. Baerends. *Phys. Rev. A*, 49:2421, 1994.
- [145] P.R.T. Schipper, O.V. Gritsenko, S.J.A. van Gisbergen, and E.J. Baerends. *J. Chem. Phys.*, 112:1344, 2000.
- [146] T. H. Jr. Dunning. *J. Chem. Phys.*, 90:1007, 1989.
- [147] R. A. Kendall, T. H. Jr. Dunning, and R. J. Harrison. *J. Chem. Phys.*, 96:6796, 1992.
- [148] C. Adamo and V. Barone. *J. Chem. Phys.*, 110:6158, 1999.
- [149] T. K. Liu and A. B. F. Duncan. *J. Chem. Phys.*, 17:241, 1949.
- [150] A. Lowrey III and K. Watanabe. *J. Chem. Phys.*, 28:208, 1958.
- [151] G. Fleming, M. M. Anderson, A. J. Harrison, and L. W. Pickett. *J. Chem. Phys.*, 30:351, 1960.

- [152] E.J. Heller. Time-dependent approach to semiclassical dynamics. *J. Chem. Phys.*, 62:1544–1555, 1975.
- [153] E.V. Doktorov, I.A. Malkin, and V.I. Manko. *J. Mol. Spectrosc.*, 56:1–20, 1975.
- [154] L.S. Cederbaum and W. Domcke. *J. Chem. Phys.*, 64:603–611, 1976.
- [155] W. von Niessen, L.S. Cederbaum, and W.P. Kraemer. *Theor. Chem. Acc.*, 44:85, 1977.
- [156] M.L. Lawson Daku. personal communication.
- [157] A. Migani and M. Olivucci. In W. Domcke, D. R. Yarkony, and H. Köppel, editors, *Conical Intersections: Electronic Structure, Dynamics & Spectroscopy*, volume 15 of *Advanced Series in Physical Chemistry*, chapter 6, pages 271–320. 2004.
- [158] D.M. Leitner, J. Quenneville, B. Levine, T.J. Martínez, and P.G. Wolynes. *J. Phys. Chem.*, 107:10706, 2003.
- [159] B. Levine and T.J. Martínez. In G.A. Worth and S.C. Althorpe, editors, *Quantum Dynamics and Conical Intersections*. CCP6, Daresbury, 2004.
- [160] A. Toniolo, B. Levine, A. Thompson, J. Quenneville, M. Ben-Nun, J. Owens, S. Olsen, J. Manohar, and T.J. Martínez. In A. Kutateladze, editor, *Computational Methods in Organic Photochemistry*, page 167. Marcel-Dekker, New York, 2005.
- [161] S. Olsen, A. Toniolo, C. Ko, L. Manohar, and K. Lamothe. In M. Olivucci, editor, *Computational Photochemistry*, page 225. Elsevier, Amsterdam, 2005.
- [162] A. D. McLean and G. S. Chandler. *J. Chem. Phys.*, 72:5639, 1980.
- [163] R. Krishnan, J. S. Binkley, R. Seeger, and J. A. Pople. *J. Chem. Phys.*, 72:650, 1980.
- [164] G. Herzberg and J. Shoosmith. *Can. J. Phys.*, 34:523, 1956.
- [165] G. Herzberg. *Proc. R. Soc. London, Ser. A*, 262:291, 1961.
- [166] M.B. Smith and J. March. page 276. Wiley Interscience Ed.: Toronto, Canada, 2007.
- [167] M. Levy. *Phys. Rev. A*, 26:1200, 1982.



- [168] M. Levy and J.P. Perdew. In R.M. Dreizler and J. da Providencia, editors, *Density Functional Methods in Physics*, page 11. Plenum, 1985.
- [169] P.W. Ayers and W. Yang. *J. Chem. Phys.*, 124:224108, 2006.
- [170] R.C. Morrison. *J. Chem. Phys.*, 117:10506, 2002.
- [171] N.T. Maitra. *J. Chem. Phys.*, 122:234104, 2005.
- [172] N.T. Maitra and D.G. Tempel. *J. Chem. Phys.*, 125:184111, 2006.
- [173] R.J. Cave, F. Zhang, N.T. Maitra, and K. Burke. *Chem. Phys. Lett.*, 389:39, 2004.
- [174] N.T. Maitra, F. Zhang, F.J. Cave, and K. Burke. *J. Chem. Phys.*, 120:5932, 2004.
- [175] L.V. Slipchenko and A.I. Krylov. *J. Chem. Phys.*, 118:6874, 2003.
- [176] Y. Shao, M. Head-Gordon, and A.I. Krylov. *J. Chem. Phys.*, 118:4807, 2003.
- [177] F. Wang and T. Ziegler. *J. Chem. Phys.*, 121:12191, 2004.
- [178] F. Wang and T. Ziegler. *J. Chem. Phys.*, 122:074109, 2005.
- [179] D. R. Yarkony. 105:6277, 2001.
- [180] M. N. Paddon-Row. In V. Balzani, editor, *Electron Transfer in Chemistry, Vol 3*, page 179. Wiley-VCH, Weinheim, 2001.
- [181] M. C. Petty, M. R. Bryce, and Bloor. *An Introduction to Molecular Electronics*. Edward Arnold, London, 1995.
- [182] R. Hoffmann, A. Imamura, and W. J. Hehre. *J. Am. Chem. Soc.*, 90:1499, 1968.
- [183] R. Hoffmann. *Accounts Chem. Res.*, 4:1, 1971.
- [184] B. Krijnen, H. B. Beverloo, J. W. Verhoeven, C. A. Reiss, K. Goubitz, and D. Heijdenrijk. *J. Am. Chem. Soc.*, 111:4433, 1989.
- [185] R. M. Hermant, N. A. C. Bakker, T. Scherer, B. Krijnen, and J. W. Verhoeven. *J. Am. Chem. Soc.*, 112:1214, 1990.

- [186] P. Pasman, J.W. Verhoeven, and T.J. Deboer. *Tetrahedron Lett.*, page 207, 1977.
- [187] P. Pasman, F. Rob, and J.W. Verhoeven. *J. Am. Chem. Soc.*, 104:5127, 1982.
- [188] W. Schuddeboom, B. Krijnen, J. W. Verhoeven, E. G. J. Staring, G. L. J. A. Rikken, and H. Oevering. *Chem. Phys. Lett.*, 179:73, 1991.
- [189] F. Hoogesteger, C. A. van Walree, L. W. Jenneskens, M. R. Roest, J. W. Verhoeven, W. Schuddeboom, J. J. Piet, and J. M. Warman. *Chem. Eur. J.*, 6:2948, 2000.
- [190] C. Barolo, M.K. Nazeeruddin, S. Fantacci, D. Di Censo, P. Comte, P. Liska, G. Viscardi, P. Quagliotto, F. De Angelis, S. Ito, and M. Graetzel. *Inorg. Chem.*, 45:4642, 2006.
- [191] S. Ghosh, G.K. Chaitanya, K. Bhanuprakash, M.K. Nazeeruddin, M. Graetzel, and P.Y. Reddy. *Inorg. Chem.*, 45:7600, 2006.
- [192] M. Belletete, N. Blouin, P.L.T. Boudreault, M. Leclerc, and G. Durocher. *J. Phys. Chem. A*, 110:13696, 2006.
- [193] M. K. Nazeeruddin, T. Bessho, L. Cevey, S. Ito, C. Klein, F. De Angelis, S. Fantacci, P. Comte, P. Liska, H. Imai, and M. Graetzel. *J. Photochem. Photobiol. A-Chem.*, 185:331, 2007.
- [194] E. Mete, D. Uner, M. Cakmak, O. Gulseren, and S. Ellialtoglu. *J. Phys. Chem. C*, 111:7539, 2007.
- [195] F. De Angelis, S. Fantacci, and A. Sgamellotti. *Theor. Chem. Acc.*, 117:1093, 2007.
- [196] D. P. Hagberg, T. Marinado, K. M. Karlsson, K. Nonomura, P. Qin, G. Boschloo, T. Brinck, A. Hagfeldt, and L. Sun. *J. Org. Chem.*, 72:9550, 2007.
- [197] M. Belletete, P. La .T. Boudreault, M. Leclerc, and G. Durocher. *Theochem-J. Mol. Struct.*, 824:15, 2007.
- [198] M.S. Tsai, Y.C. Hsu, J.T. Lin, H.C. Chen, and C.P. Hsu. *J. Phys. Chem. C*, 111:18785, 2007.
- [199] A. Köhn and C. Hättig. *J. Chem. Phys.*, 119:5021, 2003.
- [200] C. Hättig. *J. Chem. Phys.*, 118:7751, 2003.

- [201] H. Fliegl, A. Köhn, C. Hättig, and R. Ahlrichs. *J. Am. Chem. Soc.*, 125:9821, 2003.
- [202] C. Hättig, A. Hellweg, and A. Köhn. *J. Am. Chem. Soc.*, 128:15672, 2006.
- [203] A.L. Sobolewski and W. Domcke. *Eur. Phys. J. D*, 20:369, 2002.
- [204] M. A. L. Marques, X. Lopez, D. Varsano, A. Castro, and A. Rubio. *Phys. Rev. Lett.*, 90:258101, 2003.
- [205] A. L. Sobolewski and W. Domcke. *J. Phys. Chem. A*, 108:10917, 2004.
- [206] N.T. Maitra and D.G. Tempel. *J. Chem. Phys.*, 125:184111, 2006.
- [207] A.B.J. Parusel, G. Köhler, and S. Grimme. *J. Phys. Chem. A*, 102:6297, 1998.
- [208] C. Jamorski, J.B. Foresman, C. Thilgen, and H.P. Lüthi. *J. Chem. Phys.*, 116:8761, 2002.
- [209] C. Jamorski Jödicke and H.P. Lüthi. *J. Am. Chem. Soc.*, 125:252, 2003.
- [210] D. Rappoport and F. Furche. *J. Am. Chem. Soc.*, 126:1277, 2004.
- [211] D. E. Woon and T. H. Dunning. *J. Chem. Phys.*, 98:1358, 1993.
- [212] C. Hättig and F. Weigend. *J. Chem. Phys.*, 113:5154, 2000.
- [213] C. Hättig and A. Köhn. *J. Chem. Phys.*, 117:6939, 2002.
- [214] F. Weigend and M. Häser. *Theor. Chem. Acc.*, 97:331, 1997.
- [215] F. Weigend, A. Köhn, and C. Hättig. *J. Chem. Phys.*, 116:3175, 2002.
- [216] M. Häser and R. Ahlrichs. *J. Comput. Chem.*, 10:104, 1989.
- [217] R. Bauernschmitt and R. Ahlrichs. *J. Chem. Phys.*, 104:9047, 1996.
- [218] V.V. Jarikov and D.C. Neckers. *J. Org. Chem.*, 66:659, 2001.
- [219] B. Wegewijs and J. W. Verhoeven. *Advan. Chem. Physics.*, 106:221, 1999.
- [220] V. N. Nemykin, Ra .G. Hadt, R. V. Belosludov, H. Mizuseki, and Y. Kawazoe. *J. Phys. Chem. A*, 111:12901, 2007.

[221] O. V. Gritsenko, P. R. T. Schipper, and Baerends E. J. *Chem. Phys. Lett.*, 302:199, 1999.

[222] O. Gritsenko and E.J. Baerends. *J. Chem. Phys.*, 121:655, 2004.

# Publications

## published

- M.-E. Moret, E. Tapavicza, L. Guidoni, U. F. Röhrig, M. Sulpizi, I. Tavernelli and U. Rothlisberger, Quantum mechanical/molecular mechanical (QM/MM) Car-Parrinello simulations in excited states, *Chimia*, 59(7-8), 493 (2005)
- E. Tapavicza, I. Tavernelli, U. Rothlisberger, Trajectory surface hopping within linear response time-dependent density functional theory, *Phys. Rev. Lett.* 98, 023001 (2007).
- E. Tapavicza, I-C. Lin, O. A. von Lilienfeld, I. Tavernelli, M. D. Coutinho-Neto, and U. Rothlisberger, Weakly Bonded Complexes of Aliphatic and Aromatic Carbon Compounds Described with Dispersion Corrected Density Functional Theory, *J. Chem. Theory Comput.*, 2007, 3 (5), 1673.

## submitted or in preparation

- E. Tapavicza, I Tavernelli, U. Rothlisberger, C. Filippi, M. E. Casida, Mixed Time-Dependent Density-Functional Theory/Classical Trajectory Surface Hopping Study of Oxirane Photochemistry, submitted to *J. Chem. Phys.*
- A. K. Renfrew, A. D. Phillips, E. Tapavicza, U. Rothlisberger, P. J. Dyson, Tuning the efficacy of Ruthenium(II)-arene (RAPTA) antitumour compounds with fluorinated arene ligands
- E. Tapavicza, I. Tavernelli, U. Rothlisberger, Calculation of Non-Adiabatic Coupling Vectors by TDDFT

- E. Tapavicza, I. Tavernelli, U. Rothlisberger, CC2 and TDDFT Studies of a Fluorescent Donor-Bridge-Acceptor Molecule

# Presentation and Posters

- Poster: Photoinduced intramolecular electron transfer using TDDFT at 'Time-Dependent Density Functional Theory - Prospects and Applications', Benasque, Center of Science September 2004
- Poster: Photoinduced intramolecular electron transfer using TDDFT at 'Fall Meeting Swiss Chemical society 2004', Zürich, October 2004
- Poster: Molecular dynamics with quantum transition using TDDFT at 'Density Functional Theory 2005', Geneva, September 2005
- Oral Presentation: Molecular dynamics with quantum transition using TDDFT at 'Fall Meeting Swiss Chemical society 2005', Lausanne, October 2005
- Oral Presentation: Molecular dynamics with quantum transition using TDDFT at 'Quantum simulation of solids and liquids', Lyon, November 2005
- Poster: Carbon complexes described by dispersion corrected density functional theory at 'CE-CAM - New developments for first principles molecular dynamics simulations in condensed matter and molecular physics', May 15-18, 2006
- Oral Presentation: Trajectory surface hopping within time-dependent density functional theory at 'Car-Parrinello dyna-mix and co.' Paris, April 19th 2006
- Poster: Trajectory surface hopping within time-dependent density functional theory at 'The 9th Sostrup Summer School. Quantum Chemistry and Molecular Properties', Denmark, June 25 - July 7, 2006.
- Poster: Trajectory surface hopping within time-dependent density functional theory at 'Research Day 2006 - Ecole Polytechnique Federale de Lausanne', Lausanne, November 16 2006

- Poster: TDDFT trajectory surface hopping study of decomposition of oxirane, 'Progress in ab initio modelling of biomolecules : towards computational spectroscopy', Rome, April 2007.
- Oral Presentation: Trajectory surface hopping within time-dependent DFT: theory and applications to photochemistry, Reunion du Laboratoire de Chimie Théorique, Université Joseph Fourier, April 20 2006.



# Acknowledgment

I am grateful to Ursula Röthlisberger giving me the confidence and accepting me to do my PhD studies at her group in Lausanne. With her experience she always supported me and gave me the possibility to follow up the things that seemed the most motivating and interesting to me. I also want to thank her for giving me so many possibilities to attend conferences and schools.

A special thanks goes to Ivano Tavernelli who introduced me to theory and practice, and during the whole PhD time he was always there to assist me in research and programming.

I really appreciated the fruitful collaboration with Mark E. Casida, and thank him for his endless enthusiasm for TDDFT, for helping me to understand things better, and finally for accepting to be examiner in my PhD exam.

For joining the jury of my thesis exam, I would like to thank Nikos Doltsinis, Jiří Vaníček, and Jean-Claude Bünzli.

I like to thank Claudia Filippi for the nice collaboration and the scientific and non-scientific discussions we had on different conferences. For scientific discussions and support with computer codes I acknowledge Salomon Billeter, Jürg Hutter, Tomasz A. Weselowski, Felipe Cordova and Carme Rovira. I also like to thank Carme and her group for the hospitality that I received in Barcelona. I also thank Paul Dyson and Anna Renfrew, for the interesting collaboration on Ruthenium anticancer compounds.

I thank our secretary Karin, in every situation she knew exactly how to handle bureaucratic affairs during my time in Switzerland.

I thank my friend Ari P. Seitsonen for his company and always being interested in my work, posing critical questions and proofreading my articles. He also tried to introduce me into Finnish opera.

The whole LCBC team is thanked for the good working atmosphere but also for the time we spend outside the lab. A special thanks goes to Geoff and Sam, the human spell checkers in the writing of this

thesis. Another special thanks goes to the administrators Christian and Linux Guruçao Matteo, without their support not much would have been possible. It was also Matteo who invented the saying 'See you Slater'. Thanks to Anatole for sharing his inspiring view of science but also for hanging out in Spain and at 'Tendance Catalogue' concerts. I thank Maria-Carola for her endurance in supporting me such a long time in the office. It was also pleasant to share the office with Mauricio, with whom I could always discuss about my work. Thanks to Mitch, my groovy flat mate, and to Pascal, Ute, Leonardo, Patrick, I-Chun, Marilisa, Fanny, Hakan, Djaffar, Julien, Roberto, Denis, Michele, Marialore, Samuele, Marc-Etienne, Pablo, Stefano, Topaz, Ruby.

Besides, I was very happy to meet people outside the lab like Tom, David R., Melanie, Benjamin, Isabelle, Fidi, Gustavo, Zach.

Thanks to my belayers Jan, Laurin, Pierre, Pascal, David H., Pirmin and the people from Charmey, my friends from Valais, not so much for belaying but more for the exciting and relaxing hours we spent rockclimbing and bouldering.

Thanks for the support from my old friends from Bayreuth Michi, Clemens, Georg, Anna, and from Munich: Bidji, Sandra, Paul, Cinq, Norbert, and Sven, my friend since kindergarden.

It was always refreshing to have visitors like Niki Wengi (¡Hueiong!) from Bariloche, Dieter, Ana, Layla, and meeting people like Ivana and Angie in India.

I thank my lovely aşkim Mine for always being there for me.

Finally, I would like to thank my whole family. Especially my parents, Heide and Marko, always caring about me and encouraging me to do the things I want. Thanks also to my brother Rafael, my sister Evelyn together with Alfredo, Rosa, Marina, Marylin, Peterle, and my grandparents, uncles, aunts and cousins.

# Curriculum Vitae

## Enrico Marko Tapavicza

Born 28<sup>th</sup> April 1976 in Karlsruhe, Germany

- **Secondary school** until 1995 Gymnasium Unterhaching, Germany
- **Basic studies** October 1997 - October 1999, Chemistry at Technical University Munich, Germany
- **Advanced studies** October 1999 - March 2003, Chemistry at University of Bayreuth, Germany
  - **Exchange semester** winter 2000/2001 exchange semester at University of Zaragoza, Spain
  - **Short term project** October - December 2001, with Prof. Dirk Schwarzer, Max Planck Institute for Biophysical Chemistry, Göttingen, Germany
  - **Diploma thesis** NMR Spectroscopy of Proteins, supervision: Prof. Paul Rösch, University of Bayreuth, Germany
- **Current Degree** March 2003, Diplom-Chemiker at University Bayreuth, Germany
- **PhD studies** since September 2003 under supervision of Prof. Ursula Röthlisberger at EPFL
- **Practical**
  - **Civil Service** September 1995-1996 at school for physically disabled children (Bayr. Landesschule für Körperbehinderte), Munich, Germany
  - **Working Student** summer 1999 in Analytical Chemistry at GSF-Research Center for Environmental Health, Neuherberg, Germany
  - **Teaching** at University of Bayreuth, Germany and EPFL